

DOT/FAA/TC-14/38

Federal Aviation Administration
William J. Hughes Technical Center
Aviation Research Division
Atlantic City International Airport
New Jersey 08405

Low Cost Accurate Angle of Attack System

September 2015

Final Report

This document is available to the U.S. public through the National Technical Information Services (NTIS), Springfield, Virginia 22161.

This document is also available from the Federal Aviation Administration William J. Hughes Technical Center at actlibrary.tc.faa.gov.



U.S. Department of Transportation
Federal Aviation Administration

NOTICE

This document is disseminated under the sponsorship of the U.S. Department of Transportation in the interest of information exchange. The U.S. Government assumes no liability for the contents or use thereof. The U.S. Government does not endorse products or manufacturers. Trade or manufacturers' names appear herein solely because they are considered essential to the objective of this report. The findings and conclusions in this report are those of the author(s) and do not necessarily represent the views of the funding agency. This document does not constitute FAA policy. Consult the FAA sponsoring organization listed on the Technical Documentation page as to its use.

This report is available at the Federal Aviation Administration William J. Hughes Technical Center's Full-Text Technical Reports page: actlibrary.tc.faa.gov in Adobe Acrobat portable document format (PDF).

Technical Report Documentation Page

1. Report No. DOT/FAA/TC-14/38	2. Government Accession No.	3. Recipient's Catalog No.	
4. Title and Subtitle LOW COST ACCURATE ANGLE OF ATTACK SYSTEM		5. Report Date September 2015	
		6. Performing Organization Code	
7. Author(s) David F. Rogers, Borja Martos, and Francisco Rodrigues	8. Performing Organization Report No.		
9. Performing Organization Name and Address Embry-Riddle Aeronautical University Eagle Flight Research Center / College of Engineering 1585 Aviation Parkway, Suite 606 Daytona Beach, FL 32114		10. Work Unit No. (TRAIS)	
		11. Contract or Grant No. 2014-G-013	
12. Sponsoring Agency Name and Address U.S. Department of Transportation Federal Aviation Administration Transport Airplane Directorate 1601 Lind Ave., SW Renton, WA 98057		13. Type of Report and Period Covered Final Report	
		14. Sponsoring Agency Code ANM-112	
15. Supplementary Notes			
16. Abstract A low cost (\$100 / Table A-1) differential pressure based Commercial Off The Shelf (COTS) angle of attack data acquisition system was designed, successfully reduced to practice, wind tunnel tested and flight tested. The accuracy of the differential pressure angle of attack system was determined to be $\frac{1}{4}$ to $\frac{1}{2}$ of a degree. The repeatability of the data from the COTS system was excellent. Using unnormalized differential pressure ($P_{fwd}-P_{45}$) does not provide adequate accuracy throughout the aircraft angle of attack range. This technique is dynamic pressure dependent. For a limited range of high angles of attack near stall a linear fit to the data provides adequate accuracy. However, accuracy at low angles of attack, such as required by cruise, is poor. Hence, systems similar to that tested, using a linear calibration are basically stall warning devices. A physics based determination of angle of attack was successful, provided that a reasonably accurate aircraft lift curve is determined. Calculation of the lift curve slope was within 0.01/degree of the value determined by flight test using and alpha/beta probe. A calibration curve based on the ratio of P_{fwd}/P_{45} was studied and determined to be linear throughout the aircraft angle of attack if the probe is located on the wing lower surface between an estimated 25% and 60% of the local wing chord.			
17. Key Words Angle of Attack, General Aviation, Sensors, Instrumentation		18. Distribution Statement This document is available to the U.S. public through the National Technical Information Service (NTIS), Springfield, Virginia 22161. This document is also available from the Federal Aviation Administration William J. Hughes Technical Center at actlibrary.tc.faa.gov .	
19. Security Classif. (of this report) Unclassified	20. Security Classif. (of this page) Unclassified	21. No. of Pages 103	22. Price

Low Cost Accurate Angle of Attack System

David F. Rogers, Phd, ATP

Rogers Aerospace Engineering & Consulting

Principal Investigator COTS Low Cost Accurate Angle of Attack System

www.nar-associates.com

Borja Martos, Phd, ATP, CFI-AMI

Eagle Flight Research Center

Embry-Riddle Aeronautical University

Principal Investigator Flight Testing FAA Grant 2014-G-013

Francisco Rodriguez

Rogers Aerospace Engineering & Consulting

Electronics Engineer

September 2015

ACKNOWLEDGEMENTS

Dave Rogers gratefully acknowledge the critical contributions of Francisco Rodrigues. As usual, you did both of us proud in your ability to convert concepts into electronic and computer code. After 40 years of association, I expected, and received, nothing less. Not bad for a couple of geriatric engineers.

Dave Rogers acknowledges the professional support of Borja Martos of Eagle Flight Research Center for the exceptional conduct of the flight test program. Borja is an outstanding flight test engineer. He is a superb pilot whose skills provide excellent data sets.

Dave Rogers would also like to acknowledge the support of Peter Osterc, Alfonso Noriega, and Yosvanny Alonso, students of the Eagle Flight Research Center, for their efforts as computer flight test engineers on the various test flights.

The willingness of Dave Sizoo of the FAA Small Airplane Directorate and Bob McQuire of the FAA William J. Hughes Technical Center for their flexibility in supporting the flight test program is gratefully acknowledged. It was a pleasure working with you.

TABLE OF CONTENTS

Executive Summary	1
1. Introduction	1
2. The Aircraft Fundamental Angle of Attack	1
2.1. Nondimensionalization	2
2.2. Relation Between Angle of Attack and Velocity	2
2.3. Fundamental Angle of Attack — $\alpha_{L/D_{max}}$	3
2.4. Power Required and Angle of Attack	4
2.5. Why Is Flying Angle of Attack Important?	5
3. Wind Tunnel Tests	5
3.1. The Calibration Effect	6
3.2. Calibration Techniques	7
3.3. Alternate Normalization Techniques	7
4. Design of the Data Acquisition System	8
4.1. Accuracy	8
4.2. Pressure Range	8
4.3. Reference Pressure	9
4.4. Pressure Sensors	9
4.5. Development System	10
4.6. Basic Design of the DFRDAS Data Acquisition System.	10
4.7. Software Description	11
4.8. Wind Tunnel Testing Of The DFRDAS Breadboard	12
4.9. Noload Altitude Test	12
5. Road Tests	12
6. Proof of Concept Flight Test	13
7. The Aircraft	13
8. The 21/22 January 2015 Flights	14
8.1. Physics Based Determination of Absolute Angle of Attack	14
8.2. The Results of the 21/22 January 2015 Flight Tests	15
9. Air Data Probe and Alpha/Beta Boom	16
10. The Results Of The 22 April 2015 Flight Test	17
10.1. Left Wing DFRDAS-1 Results	18
10.2. Right wing DFRDAS-2 Results	19
11. Stall Flight Tests	20
12. The Results Of The 26/27 May 2015 Flight Tests	20
12.1. Left Wing DFRDAS-1 Results	22
12.2. Right Wing DFRDAS-2 Results	23
12.3. Right Wing Flaps 40° Results	23
13. Aerodynamics Of Why A Linear Calibration Curve?	25
14. The Results Of The 18/19 August 2015 Flight Tests	26
14.1. Right Wing DFRDAS-2 Results	27
14.2. Stall Results	27

15. What Works And What Does Not Work	30
16. Conclusions	32
17. Suggested Future Work	33
18. References	33
Appendix A. Details for the Arduino Based COTS System	35
Appendix B. Mechanical Drawings, General Assembly, Ground and Flight Testing	47
Appendix C. Aerodynamics Of Why A Linear Calibration Works	71
Appendix D. The Effect Of The Average Of An Average	74
Appendix E. The Response of the DFRDAS To Various Stall Configurations	75
Appendix F. Hazards, Test Cards and Flight Log	83

LIST OF FIGURES

Figure	Page
1. Altitude effect on power required.	2
2. Nondimensional power required - multiple effects	2
3. Relationship between nondimensional velocity and nondimensional angle of attack.	3
4. Relationship between nondimensional power required and nondimensional angle of attack.	4
5. Probe mounted in the wind tunnel.	5
6. Probe pressure port locations.	5
7. $P_{fwd}-P_{45}$ as a function of angle of attack.	5
8. $P_{fwd}-P_{45}$ normalized with dynamic pressure.	5
9. Flight line and the effect of two-point and four-point linear calibration.	6
10. An alternate method of normalizing the pressure.	8
11. Angle of attack as a function of P_{fwd}/P_{45} .	8
12. MS4525 differential pressure sensor.	8
13. Bosch BMP085 altitude/pressure absolute pressure	9
14. Arduino UNO R3 development micro-controller system.	10
15. DFRDAS breadboard as used for wind tunnel verification tests.	11
16. Comparison of wind tunnel result for the breadboard data acquisition system and the results read from the inclined manometer.	11
17. Combined results for the 21 and 22 January 2015 flight tests.	15
18. Alpha/beta probe mounted on the aircraft.	15
19. Alpha/beta probe head.	16
20. Spanwise location of the right wing probe DFRDAS-2.	18
21. Alpha vs P_{fwd}/P_{45} results for the left wing DFRDAS-1 probe for the 22 April 2015 flight test.	18
22. Alpha vs P_{fwd}/P_{45} results for the right wing 23. P_{fwd}/P_{45} vs Alpha results for the right wing	19
24. Alpha vs P_{fwd}/P_{45} results for the right wing DFRDAS-2 for the 22 April 2015 flight test.	21
25. Lift coefficient vs angle of attack with respect to the fuselage reference line for two stall flight tests.	21
26. Absolute angle of attack vs time for Stall 1. P_{fwd}/P_{45} data is from DFRDAS-2. The absolute angle of attack is calculated using the calibration curve for the DFRDAS-2 shown in Figure 23.	22
27. Absolute angle of attack vs P_{fwd}/P_{45} for the DFRDAS-1 from the 26 May 2015 flight test. The probe is mounted approximately at the leading edge of the left wing of the aircraft.	22
28. Absolute angle of attack vs P_{fwd}/P_{45} for the DFRDAS-2 from the 26 May 2015 flight test. The probe is mounted at 38.9% of the local chord on the right wing of the aircraft.	24
29. Absolute angle of attack vs P_{fwd}/P_{45} for DFRDAS-2 for the 27 May 2015 flight test with flaps extended to 40°. The probe is mounted at 38.9% local chord on the right wing.	24
30. Two frame grabs showing the streamlines around an airfoil without flaps extended.	25
31. Sketch of the pressure distribution on the surface of a typical airfoil.	26
32. Frame grabs showing the streamlines around an airfoil with a flap extended.	26
33. Combined linear fit for absolute angle of attack vs P_{fwd}/P_{45} in the clean configuration with the right hand probe at 38.9% of local chord.	28
34. The DFRDAS-2 results for a standard FAA stall in the clean configuration with the probe at 38.9% of the local chord. The curve is based on a 3-point moving average of the raw data. The red dots represent individual smoothed data points.	28
35. DFRDAS-2 results for a standard FAA stall in the clean configuration with the probe at 38.9% of the local chord. The curve is based on a 3-point moving average of the raw data. The red dots represent individual smoothed data points.	29
36. DFRDAS-2 results for a standard FAA stall in the clean configuration in a right 20° bank with the probe at 38.9% of the local chord. The curve is based on a 3-point moving average of the raw data. The red dots represent individual smoothed data points.	29
37. DFRDAS-2 results for a standard FAA stall with zero bank and 40° flap extended with the probe at 38.9% of the local chord. The curve is based on a 3-point moving average of the raw data. The red dots	

represent individual smoother data points.	30
38. What works and what does not work: Angle of attack vs (a) P_{fwd}/P_{45} , (b) $(P_{fwd} - P_{45})/P_{45}$, (c) $(P_{fwd} - P_{45})/q$, (d) $\Delta(P_{fwd} - P_{45})$.	31
A-1. Block diagram for Arduino DFRDAS data acquisition system.	35
A-2. Block diagram for Arduino DFRDAS data acquisition system sketch (program).	37
B-1. Isometric view.	47
B-2. Side view.	47
B-3. Front view.	47
B-4. Top view.	48
B-5. Right wing tip with boom (side view).	48
B-6. Right wing tip (side view).	48
B-7. Right wing tip with boom (view looking forward).	48
B-8. Angle of attack data boom.	49
B-9. Data boom free body diagram.	49
B-10. Point loads magnitude and position.	50
B-11. Shear force diagram.	50
B-12. Bending moment diagram.	51
B-13. Predicted deflection.	51
B-14. Test setup with boom unloaded.	52
B-15. Test setup – boom loaded.	52
B-16. Rulers, clamps and inclinometer stations setup.	53
B-17. Clamps.	53
B-18. Weights with the correspondent clamp.	53
B-19. Boom – tip deflection.	54
B-20. Air data boom pneumatic and digital wiring.	56
B-21. Commanded altitude vs static pressure.	58
B-22. Values for the POH and ERAU DAS airspeeds in graphical format.	62
B-23. Static pressure position error (ΔPPC) vs indicated airspeed.	62
B-24. Velocity static pressure position error (ΔVPC) vs indicated airspeed.	63
B-25. Altitude static position error vs indicated airspeed.	63
B-26. $\Delta\alpha$ vs. time, α vs time, airspeed vs time, and altitude vs time for record 1.	65
B-27. $\Delta\alpha$ vs α_i for all legs.	65
B-28. α_{true} vs α_i for all legs.	66
B-29. Stall 1 lift coefficient vs angle of attack.	67
B-30. Stall 2 lift coefficient vs angle of attack.	67
B-31. Comparison between Stalls 1 and 2.	68
B-32. Calibrated airspeed during Stall 1	68
B-33. Calibrated airspeed during Stall 2.	69
B-34. Calibrated angle of attack during Stall 1.	69
B-35. Calibrated angle of attack during Stall 2.	70
C-1. Frame grabs showing the streamlines around an airfoil without flaps extended.	71
C-2. Sketch of the pressure distribution on the surface of a typical airfoil.	72
C-3. Frame grabs showing the streamlines around an airfoil with flaps extended.	73
D-1. Values for angle of attack and P_{fwd}/P_{45} from DFRDAS-2 for one leg of the 4-leg GPS data point for $V_{L/D_{max}}$ for the 26 May 2015 flight test.	74
E-1. FAA standard stall with Flaps 0° and Bank 0° DFRDAS-2 probe on the right wing at 38.9% of the local chord.	75
E-2. FAA standard stall with Flaps 0° and Bank 20° DFRDAS-2 probe on the right wing at 38.9% of the local chord.	76
E-3. FAA standard stall with Flaps 0° and Bank 30° DFRDAS-2 probe on the right wing at 38.9% of the local chord.	76
E-4. FAA accelerated stall with Flaps 0° and Bank 0° DFRDAS-2 probe on the right wing at 38.9% of the	

local chord.	77
E-5. FAA accelerated stall with Flaps 0° and Bank 0° DFRDAS-2 probe on the right wing at 38.9% of the local chord.	77
E-6. FAA accelerated stall with Flaps 21.5° and Bank 0° DFRDAS-2 probe on the right wing at 38.9% of the local chord.	78
E-7. FAA standard stall with Flaps 21.5° and Bank 20° DFRDAS-2 probe on the right wing at 38.9% of the local chord.	78
E-8. FAA standard stall with Flaps 21.5° and Bank 30° DFRDAS-2 probe on the right wing at 38.9% of the local chord.	79
E-9. FAA accelerated stall with Flaps 21.5° and Bank 0° DFRDAS-2 probe on the right wing at 38.9% of the local chord.	79
E-10. FAA standard stall with Flaps 30° and Bank 0° DFRDAS-2 probe on the right wing at 38.9% of the local chord.	80
E-11. FAA standard stall with Flaps 30° and Bank 20° DFRDAS-2 probe on the right wing at 38.9% of the local chord.	80
E-12. FAA standard stall with Flaps 30° and Bank 30° DFRDAS-2 probe on the right wing at 38.9% of the local chord.	81
E-13. FAA accelerated stall with Flaps 30° and Bank 0° DFRDAS-2 probe on the right wing at 38.9% of the local chord.	81
E-14. FAA standard stall with Flaps 30° and Bank 30° DFRDAS-2 probe on the right wing at 38.9% of the local chord. This is a four cycle limit cycle oscillation.	82
F-1. EFRC safety finding.	83
F-2. EFRC flight permit.	84
F-3. Test cards and safety considerations cover.	85
F-4. Airworthiness and safety process.	86

LIST OF TABLES

Table	Page
A-1. Parts List and Costs—DFRDAS Data Acquisition System.	36
B-1. Deflection and displacement.	54
B-2. Cessna 182Q instrumentation.	56
B-3. Commanded altitude vs. measured pressure.	57
B-4. Velocity corrections as listed in the pilot's operating handbook (POH).	61
B-5. Correction values determined during ADS calibration.	61
E-1. Stall Series.	75
F-1. Definitions of severity categories (Reference MILSTD-882D).	87
F-2. Mishap probability levels (Reference MILSTD-882D).	88
F-3. Comparative risk assessment matrix (Reference MILSTD-882C).	89
F-1. Flight log.	90

LIST OF ACRONYMS

CFR	Code of Federal Regulations
DFRDAS	David F. Rogers Data Acquisition System
ERAUDAS	Embry Riddle Aeronautical University Data Acquisition System
FAA	Federal Aviation Administration

EXECUTIVE SUMMARY

The rate of General Aviation accidents and fatalities is the highest of all aviation categories and has been nearly constant for the past decade. According to the NTSB, in 2010 GA accidents accounted for 96 percent of all aviation accidents, 97 percent of fatal aviation accidents, and 96 percent of all fatalities for U.S. civil aviation. However, GA accounted for 51 percent of the estimated total flight time of all U.S. civil aviation in 2010. The FAA identified the top three causes of fatal GA accidents to be: 1) loss of control in flight (LOC), 2) controlled flight into terrain (CFIT), and 3) system or component failure/power plant. Additionally, the general aviation joint steering committee (GAJSC) recently published its final report on loss of control, approach and landing. The GAJSC LOC working group recommended angle of attack systems as one of its top safety enhancements for general aviation aircraft. Current differential pressure angle of attack systems for light general aviation aircraft concentrate on slow flight / stall regime. Typically, outside of this flight regime, these angle of attack systems are inaccurate. Hence, they are unusable for critical flight regimes other than the stall region.

In this study, such systems were studied and it was found that using unnormalized differential pressure ($P_{fwd} - P_{45}$) does not provide adequate accuracy throughout the aircraft angle of attack range. Using unnormalized differential pressure ($P_{fwd}-P_{45}$) does not yield accurate angle of attack data throughout the aircraft normal operating envelope. The calibration curve is nonlinear. For a limited range of high angles of attack near stall a linear fit to the data near stall provides adequate accuracy. However, accuracy at low angles of attack, such as required by cruise, is poor. Hence, systems using unnormalized differential pressure, similar to that tested, which use a linear calibration are basically stall warning devices.

Four alternate techniques were flight tested using the two pressure ports, designated P_{fwd} and P_{45} on the probe used with the COTS angle of attack data acquisition system. The flight tested configurations were: the ratio of P_{fwd}/P_{45} , $(P_{fwd} - P_{45})/P_{45}$, which is just $((P_{fwd}/P_{45})-1)$, $(P_{fwd}-P_{45})/q$ and $(P_{fwd}-P_{45})$. Only the ratio of P_{fwd}/P_{45} provided an accurate angle of attack throughout the aircraft normal operating environment including into and recovery from the stall region. The calibration curve based on the ratio of P_{fwd}/P_{45} was studied and determined to be linear throughout the aircraft angle of attack provided that the probe is located on the wing lower surface between an estimated 25% and 60% of the local wing chord.

The resulting calibration curve was linear because of the smooth laminar flow on the lower wing surface including when the upper wing surface was partially or fully separated. Normalizing $(P_{fwd}-P_{45})/q$, i.e., normalizing differential pressure with dynamic pressure, also produced a linear calibration curve (italic) provided that the aircraft true freestream dynamic pressure was used. Similar results may be expected for other differential pressure systems.

A low cost (\$100 / Table A-1) differential pressure based Commercial Off The Shelf (COTS) angle of attack data acquisition system was designed, successfully reduced to practice, wind tunnel tested and flight tested. The accuracy of the COTS differential pressure angle of attack system was determined to be $\frac{1}{4}$ to $\frac{1}{2}$ of a degree. The repeatability of the data from the COTS system was excellent. Differential pressure angle of attack systems are dynamic pressure dependent. A physics based determination of angle of attack was successful, provided that a reasonably accurate aircraft lift curve is determined. Calculation of the lift curve slope was within 0.01/degree of the value determined by flight test using an alpha/beta probe.

1. INTRODUCTION

Accurate angle of attack information is important for safe and efficient operation throughout the aircraft flight envelope. Accurate knowledge of angle of attack in the low speed/high angle of attack regime is important to prevent the typical low altitude base to final stall/spin, approach and departure/go around accident. In most cases, such a stall or stall/spin is unrecoverable. Current differential pressure angle of attack systems for light general aviation aircraft concentrate on this flight regime. Typically, outside of this flight regime, these angle of attack systems are inaccurate. Hence, they are unusable for critical flight regimes other than the stall region.

At angles of attack between the angle of attack for minimum power required (maximum endurance) and stall, the aircraft is operating on the backside of the power required curve. In this regime, the effect of power application is reversed, i.e., the pilot must add power to fly slower. This is counter intuitive. Furthermore, in this flight regime the aircraft does not have speed stability. These characteristics frequently lead to inadvertent controlled flight into terrain. Providing accurate angle of attack information to the pilot that clearly depicts this flight regime is useful in preventing **departure from controlled flight**.

Lower than the angle of attack for minimum power required, the angle of attack for maximum lift to drag ratio corresponds to maximum range and maximum glide ratio for a piston engine propeller aircraft. This angle of attack does not change with density altitude, weight, load factor, etc. Hence, in a fuel critical situation and/or an engine failure situation it is critical that the pilot have accurate access to this angle of attack.

Finally, with today's fuel costs the Carson Cruise angle of attack, which represents the most efficient way to fly fast with the least increase in fuel consumption, is of significant interest.

2. THE AIRCRAFT FUNDAMENTAL ANGLE OF ATTACK*

Is there a fundamental angle of attack for an aircraft? Yes, there is. To understand this consider Figure 1. Figure 1 shows curves of the power required to maintain level flight versus true airspeed for various altitudes on a standard day. Clearly, the power required changes with altitude.

It is well known that, for a piston/propeller aircraft, a line drawn through the origin tangent to the power required curve yields the speed for maximum lift to drag ratio as illustrated by the dashed line in Figure 1. The speed for maximum lift to drag ratio is also the speed for maximum range as well as the speed for best glide. Notice that the single dashed line touches every single one of the power required curves for the various altitudes. One could say that the power required curve slides along the line for maximum lift to drag ratio with increasing altitude. Hence, the true airspeed increases with increasing altitude.

However, the angle between the line for maximum lift to drag ratio remains the same, i.e., there is only one dashed line for all altitudes. The angle between the dashed line and the abscissa (x-axis) is directly related to the absolute angle of attack for maximum lift to drag ratio. Thus, the angle of attack for maximum lift to drag ratio does not depend on density altitude.

*The following is based on a paper by David F. Rogers available at www.nar-associates.com/technical-flying.html
#Angle, Rogers, David F., "Fundamental Angle of Attack".

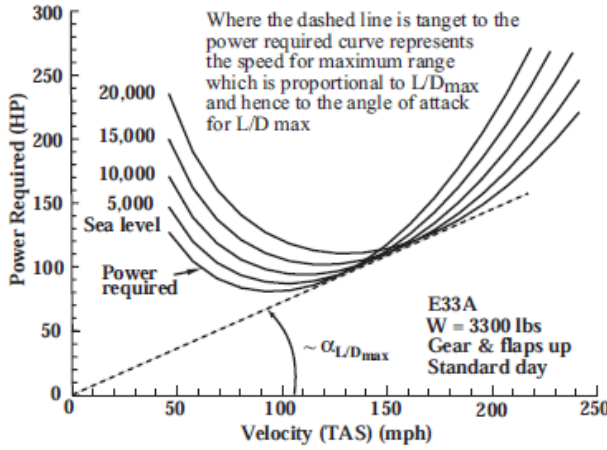


Figure 1. Altitude effect on power required.

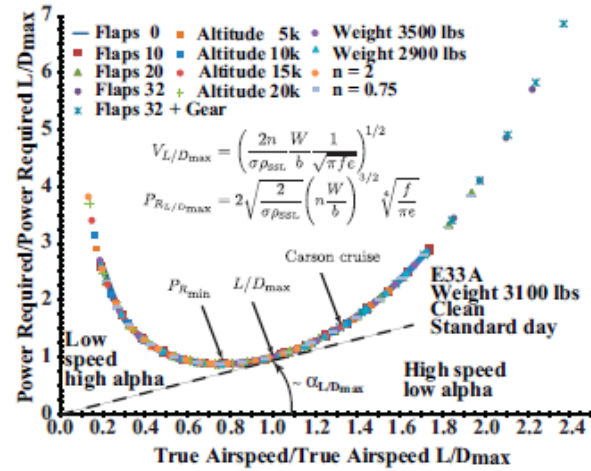


Figure 2. Nondimensional power required -multiple effects

2.1. NONDIMENSIONALIZATION

Figure 1 suggests nondimensionalizing the velocity with the velocity for maximum lift to drag ratio, $V_{L/D_{max}}$, and the power required with the power required for the maximum lift to drag ratio, $P_{R_{L/D_{max}}}$ (see [P&H49]).

The result is shown in Figure 2. Not only does nondimensionalization collapse the effect of density altitude, σ (sigma), on the power required but it also collapses the effects of weight, W , load factor, n , and aircraft configuration, i.e., e , the Oswald aircraft efficiency factor, and f , the aircraft equivalent parasite drag area, into a single curve. The formulas for the velocity and power required for maximum lift to drag ratio are given in the figure where b is the aircraft wing span. The results in Figure 2 allow determining the power required for any altitude, any weight, any load factor, and any configuration for any velocity.

2.2. RELATION BETWEEN ANGLE OF ATTACK AND VELOCITY

So far the discussion has been couched in terms of velocity. Let's now look at the absolute angle of attack. The absolute angle of attack varies inversely with the square of the velocity, i.e., from

$$C_L = a\alpha = \frac{2n}{\sigma \rho_{SSL}} \frac{W}{S} \frac{1}{V^2} \quad \text{we have} \quad \alpha = \frac{1}{a} \frac{2n}{\sigma \rho_{SSL}} \frac{W}{S} \frac{1}{V^2} \propto \frac{1}{(V^2)}$$

Where C_L is the lift coefficient, a is the linear lift curve slope, ρ_{SSL} is the density at sea level on a standard day, and S is the wing area.

Figure 3 illustrates the relationship between absolute angle of attack and velocity nondimensionalized with angle of attack and velocity for maximum lift to drag ratio, respectively. The result is a parabolic (second degree or quadratic) curve. Notice that the angle of attack decreases significantly with increasing velocity. Conversely, the angle of attack increases significantly with decreasing velocity. Again, the formulas for absolute angle of attack and power required for maximum lift to drag ratio are given in Figure 3. Notice that again the results for all the various configurations collapse into a single curve.

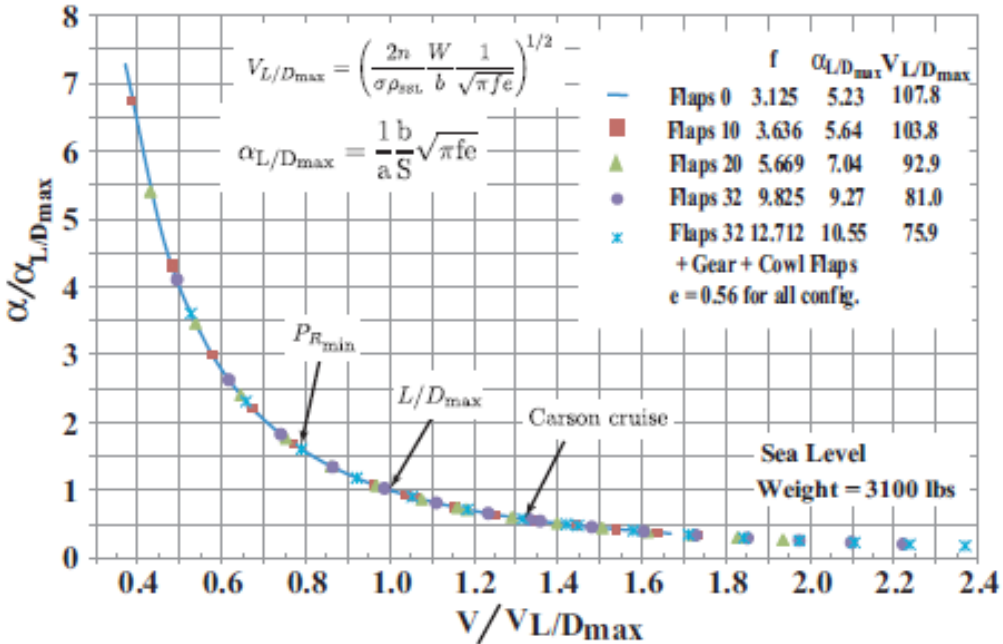


Figure 3. Relationship between nondimensional velocity and nondimensional angle of attack.

2.3. FUNDAMENTAL ANGLE OF ATTACK — $\alpha_{L/D\max}$

From the above, it is clear that the absolute angle of attack for maximum lift to drag ratio is a fundamental aircraft angle of attack. Examining the absolute angle of attack more closely, it is easy to show that it is independent of density altitude and aircraft weight. In fact, it depends only on aircraft design parameters, i.e., characteristics that are built into the aircraft. Specifically,

$$\alpha_{L/D\max} = \frac{1}{a} \frac{b}{S} \sqrt{\pi f e}$$

which does not depend on weight, W, load factor, n, or density altitude, σ . The absolute angle of attack for L/D_{\max} depends only on aircraft design parameters: lift curve slope, a, wing span, b, wing area, S, parasite drag, f, and the Oswald aircraft efficiency factor, e. Although the parasite drag, f, and the Oswald efficiency factor, e, can be changed in flight, e.g., by extending gear and/or flaps or opening cowl flaps, they are still aircraft design parameters.

In addition, there are two other angles of attack that are simple numerical multiples of the absolute angle of attack for maximum lift to drag ratio. They are the absolute angle of attack for minimum power required (maximum endurance) and the absolute angle of attack for Carson Cruise. Specifically, the corresponding angles of attack for $P_{R\min}$ and Carson Cruise are

$$\alpha_{P_{R\min}} = \sqrt{3} \alpha_{L/D\max} = 1.73 \alpha_{L/D\max} \quad \text{and} \quad \alpha_{CC} = \frac{1}{\sqrt{3}} \alpha_{L/D\max} = 0.58 \alpha_{L/D\max}$$

Hence, the absolute angle of attack for minimum power required is simply $1.73 \alpha_{L/D\max}$ and the absolute angle of attack for Carson Cruise is $0.58 \alpha_{L/D\max}$ as also shown in Figure 3. These angles of attack are also independent of density altitude, weight and load factor.

Recalling that the velocity for $V_{L/D\max}$ is

$$V_{L/D_{max}} = \left(\frac{2n}{\sigma \rho_{SSL}} \frac{W}{b} \frac{1}{\sqrt{\pi f e}} \right)^{1/2}$$

the velocities for $V_{P_{Rmin}}$ and V_{CC} are also multiples of the $V_{L/D_{max}}$. Specifically,

$$V_{P_{Rmin}} = \frac{1}{\sqrt{3}} V_{L/D_{max}} = 0.76 V_{L/D_{max}} \quad \text{and} \quad V_{CC} = \frac{1}{\sqrt{3}} V_{L/D_{max}} = 1.32 V_{L/D_{max}}$$

However, the velocity (TAS) for $V_{L/D_{max}}$ does depend on weight, density altitude and load factor, as shown by the equations above and in Figure 3. Hence, the velocity for minimum power required and Carson Cruise also depend on weight, density altitude and load factor.

2.4. POWER REQUIRED AND ANGLE OF ATTACK

Recalling the inverse square relationship between angle of attack and velocity allows recasting the nondimensional power required in terms of the angle of attack. However, it is convenient to recast it in terms of the nondimensional square root of the absolute angle of attack over the angle of attack, as shown in Figure 4. Here, we see that Figure 4 looks very similar to Figure 2. Specifically, the line through the origin tangent to the curve is again related to the absolute angle of attack for maximum lift to drag ratio. That is why it was recast in terms of the square root of the absolute angle of attack for maximum lift to drag ratio divided by the absolute angle of attack.

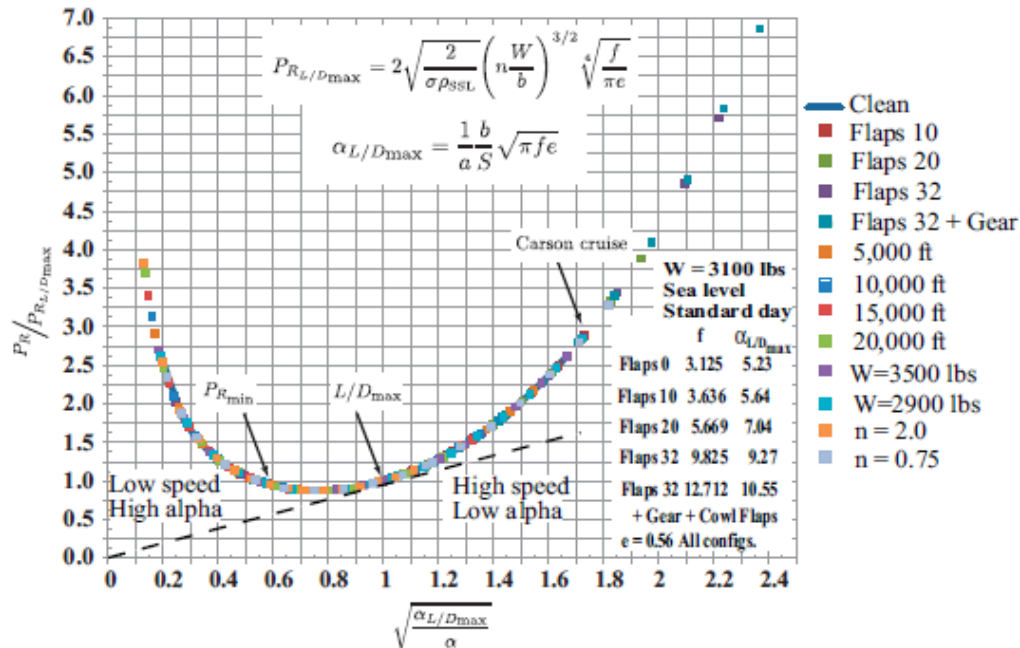


Figure 4. Relationship between nondimensional power required and nondimensional angle of attack.

2.5. WHY IS FLYING ANGLE OF ATTACK IMPORTANT?

Why is it important to understand that $V_{L/D_{max}}$ varies with weight but that $\alpha_{L/D_{max}}$ does not? To see this, look at the speed for L/D_{max} (best range speed) for a typical 3300 lb single engine retractable gear aircraft. With a single pilot and some equipment aboard, that aircraft might typically depart with full fuel at 2900 lbs. The pilot operating handbook gives the equivalent airspeed in knots (KEAS) at full gross weight as 105 KEAS. That aircraft might carry 74 gallons of useable fuel.

KEAS for $V_{L/D_{max}}$ decreases with decreasing weight as the square root of the weight ratio. For full fuel at 2900 lbs the equivalent airspeed for $V_{L/D_{max}}$ is approximately 98 KEAS. At half fuel it is approximately 95 KEAS, while with empty tanks it is approximately 90 KEAS. However, the angle of attack $\alpha_{L/D_{max}}$ remains constant. Flying angle of attack might make the mission possible whether it is to the mission destination or, in an emergency, a glide to an on airport landing rather than an off airport landing. Furthermore, no calculations are required. Simply fly the angle of attack. Similar arguments apply to Carson Cruise and minimum power required (see Figure 2).

3. WIND TUNNEL TESTS

Rogers [ROG13] conducted wind tunnel tests of a typical differential pressure angle of attack probe. The probe is shown mounted in the wind tunnel in Figure 5. Typically, in flight, the probe is mounted on the

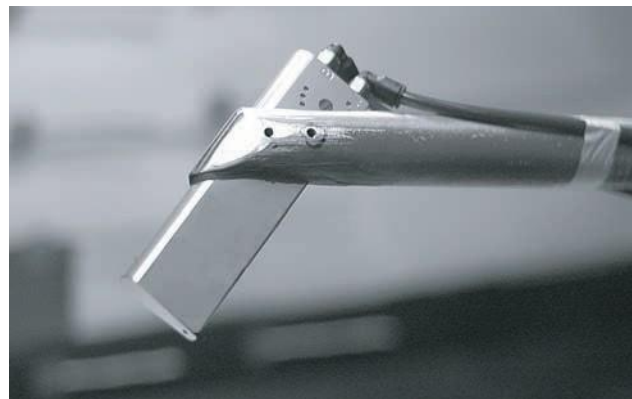


Figure 5. Probe mounted in the wind tunnel.



Figure 6. Probe pressure port locations.

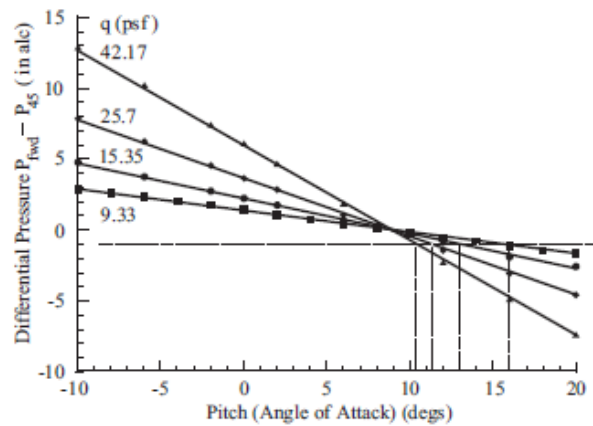


Figure 7. $P_{fwd} - P_{45}$ as a function of angle of attack.

©2015 David F. Rogers. All rights reserved.

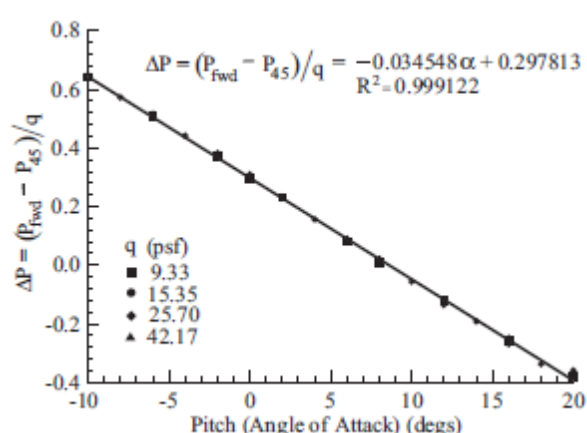


Figure 8. $P_{fwd} - P_{45}$ normalized with dynamic pressure.

bottom of the wing of a single engine aircraft or on the underside of the nose of a twin engine aircraft. The probe contains two pressure ports, each 0.1 in in diameter. One pressure port, called P_{fwd} in Figure 6, is nominally aligned with the airstream direction under the wing. In high speed cruise flight P_{fwd} nominally measures total pressure. The second pressure port, called P₄₅ in Figure 6, is located on the flat 45° surface.

The differential pressure P_{fwd}-P₄₅ is related to angle of attack. Conceptually, this is similar to the classical spherical or cylindrical based differential pressure angle of attack probe (see for example Gracey [GRA58] and Arend and Saunders [ARE09] and the references therein).

Tests were conducted for a range of angle of attack (pitch), yaw and roll for various dynamic pressures. The pressures at P_{fwd} and P₄₅ were directly measured using an inclined alcohol manometer. As expected, both pressures varied linearly with angle of attack. However, both P_{fwd} and P₄₅, as well as the differential pressure P_{fwd}-P₄₅, exhibited a dynamic pressure effect, as shown in Figure 7. Normalizing the differential pressure P_{fwd}-P₄₅ with the dynamic pressure collapsed the data to a single linear relationship, as shown in Figure 8. Hence, the effects of speed and density altitude are removed when deriving angle of attack from differential pressure.

3.1. THE CALIBRATION EFFECT

From the definition for the lift coefficient and the equation for the normalized differential pressure shown in Figure 8, along with appropriate aircraft parameters, the variation of differential pressure as a function of angle of attack can be obtained. Specifically from,

$$C_L = a\alpha = \frac{2W}{\rho_{SSL}(EAS)^2 S} \quad \text{we have} \quad \alpha = \frac{1}{a} \frac{2W}{\rho_{SSL}(EAS)^2 S}$$

where EAS is the equivalent airspeed and ρ_{SSL} is the density at sea level on a standard day. In terms of the equivalent airspeed the dynamic pressure is given by

$$q = 1/2 \rho_{SSL}(EAS)^2$$

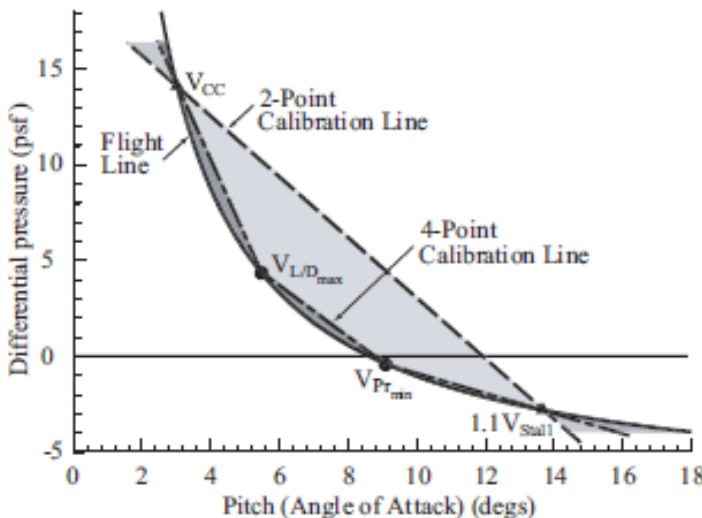


Figure 9. Flight line and the effect of two-point and four-point linear calibration.

Using the equation for the normalized differential pressure from Figure 8 the differential pressure as a function of angle of attack, called the Flight Line, is obtained as shown in Figure 9. As expected from the discussion above, the Flight Line is a parabolic function of the angle of attack.

3.2. CALIBRATION TECHNIQUES

Typically, simple differential pressure based angle of attack probes use a 2-point calibration with linear interpolation between the two calibration points. The dashed line in Figure 9 labelled 2-point calibration line shows the resulting calibration line when the Carson Cruise speed and a speed 10% above stall speed are used as the calibration points. The light gray shaded area illustrates the error in displayed angle of attack that results from this technique. The error can be significant.

Figure 9 suggests using a multiple point linear chordwise approximation to increase the accuracy of the calibration curve. The line labelled 4-point calibration line using the speed for Carson Cruise, the speed for maximum lift to drag ratio, the speed for minimum power required and a speed 10% above stall speed results. The dark gray shaded area indicates the considerably smaller error in displayed angle of attack resulting from this technique. However, neither of these linear chordwise calibration techniques accounts for the dynamic pressure effect.

3.3. ALTERNATE NORMALIZATION TECHNIQUES

The calibration techniques shown in Figure 9 do not account for the dynamic pressure effects shown in Figure 7. Because the FAA does not consider an angle of attack system on a general aviation aircraft that accesses the aircraft pitot-static system (see [SAD11]) a minor alteration, an alternate method of normalizing the differential pressure independent of the aircraft pitot-static system as suggested by Rogers [ROG13] is shown in Figure 10. Here, the pressure P_{fwd} is normalized using the pressure from the 45° surface, P_{45} . Figure 10 clearly shows that the results for all four dynamic pressures tested in the wind tunnel collapse into a single parabolic curve. Similar results, not shown, are obtained by normalizing the differential pressure $P_{fwd} - P_{45}$ by P_{45} . This technique of normalizing was used throughout the development of the digital data acquisition system (DFRDAS) for the flight test portion of this study. Figure 11 shows angle of attack as a function of P_{fwd}/P_{45} for the wind tunnel tests.

In a wind tunnel study, the independent variables are often pitch angle (angle of attack), yaw angle and roll angle along with dynamic pressure. In a wind tunnel, any pitch angle, yaw angle or roll angle can be obtained for any dynamic pressure within the capability of the tunnel. Hence, these variables are frequently used as the independent variable when presenting results. However, in steady flight, angle of attack, sideslip and roll are linked to dynamic pressure simply because angle of attack, and to a lesser extent sideslip and roll (bank angle), control speed. Consequently, as we shall see later, careful selection of the independent variable is key to obtaining appropriate results.

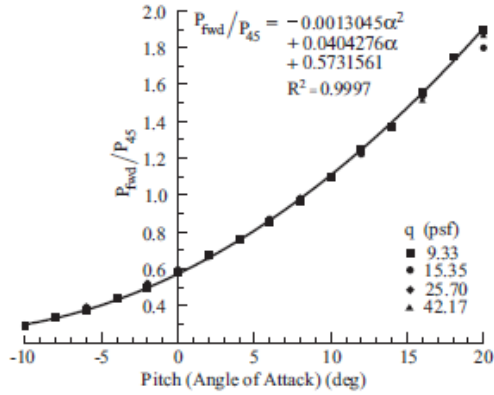


Figure 10. An alternate method of normalizing the pressure.

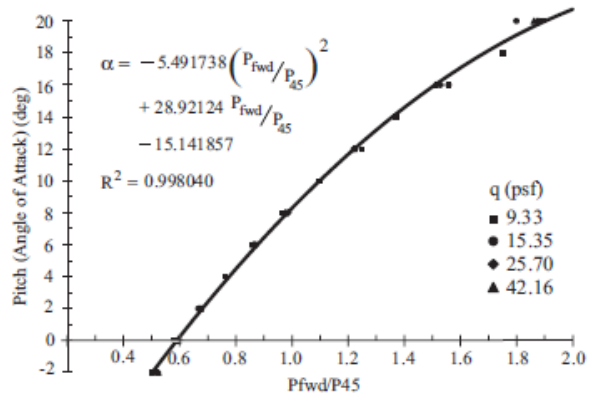


Figure 11. Angle of attack as a function of Pfwd/P45.

4. DESIGN OF THE DATA ACQUISITION SYSTEM

The fundamental considerations for the design of the data acquisition system were accuracy and low cost. These considerations, especially cost, dictated a COTS (Commercial Off The Shelf) approach in order to make the system available to the largest number of light general aviation aircraft owners.

4.1. ACCURACY

Accuracy is driven by the relatively small range of absolute angle of attack in which a typical light general aviation aircraft operates. Typically the absolute angle of attack range from cruise to stall is twenty to twenty-two degrees or less. Furthermore, the dividing lines between critical conditions are on the order of one to two degrees. For example: The difference between a stalled and unstalled wing is on the order of one degree. Similarly, to receive the benefits of Carson Cruise or to operate at L/D_{max} , the speed for best range, the angle of attack should be held within ± 1 degree, i.e., within a two degree band. These requirements dictate an accuracy of $\pm 1/4$ to $\pm 1/2$ degree.

4.2. PRESSURE RANGE

One way to establish the required pressure range is to recall that, on a standard day at sea level, the pressure exerted by a 20 inch column of water corresponds to a dynamic pressure resulting from a speed of 200 mph. A pressure of 20 inches of water equates to approximately 0.72 psi. The dynamic pressure corresponding to a speed of 200 knots equates to a pressure a bit under 1.0 psi (0.94 psi). Similarly, in the low speed range at and near stall, the dynamic pressure at 50 mph equates to approximately 1 1/4 inches of water or 0.045 psi. These are very small pressures. Furthermore, these small numbers have implications for the required accuracy of the pressure sensors.

Referring to the equation in Figure 8, one degree change in angle of attack (α) corresponds to approximately $\Delta P/q = 0.26$. From above, near stall, the dynamic pressure is approximately 0.045 psi. Hence, the differential pressure is approximately 0.012 psi. If the pressure sensor full scale is 1.0 psi and $\pm 1/4$ degree of angle attack is the required accuracy, then a full scale accuracy of 1/4 % is required.

4.3. REFERENCE PRESSURE

All pressure measurements are differential. A so called absolute pressure gauge is simply a differential pressure gauge with a built in reference pressure. An example is the Bourdon tube in an altimeter. The original wind tunnel tests used the local atmospheric pressure for the reference pressure. The question becomes: What to use as a reference pressure for the digital data acquisition system while in flight? This becomes particularly important considering the range of ‘local’ atmospheric pressure and temperature as the aircraft climbs and descends.

4.4. PRESSURE SENSORS

The Measurement Specialties MS4525DO differential pressure sensor was chosen because of commercial availability and low cost (\$21 / Table A-1). Specifically the MS4525DO-DS-5-A-I-001-D-P was used [MSa]. This unit, shown in Figure 12, is a small, ceramic based, PC board mounted low power pressure transducer with a 14 bit digital temperature compensated (11 bit) output. Full scale output is 1.0 psi with an accuracy of $\pm 1/4\%$ of full scale. The 1/8 inch barbed pressure ports mate securely with 3/32 ID tubing. The sensor is designed to operate at either 3.3 or 5.0 VDC. The sensor is compatible with either the I2C or SPI bus. Multiple I2C addresses are specified although only one I2C address was available for the sensors used for the data acquisition system.

Because of concerns with the reference pressure, an additional sensor was included in the data acquisition

System design. The Bosch BMP085 [BM085] was chosen, again, because of commercial availability and cost. The BMP085, shown in Figure 13, and its replacement the BMP180, are high-precision, ultra-low power barometric pressure sensors. Their accuracy is of the order of 2.5 hPa with low noise level down to 0.03 hPa, which is equivalent to an altitude change of approximately 8 inches. Conversion to local atmospheric pressure is straightforward. Digital temperature measurement is also available from the sensor. The BMP085 is about the size of a quarter. The BMP085, and BMP180, are also compatible with the I2C bus.

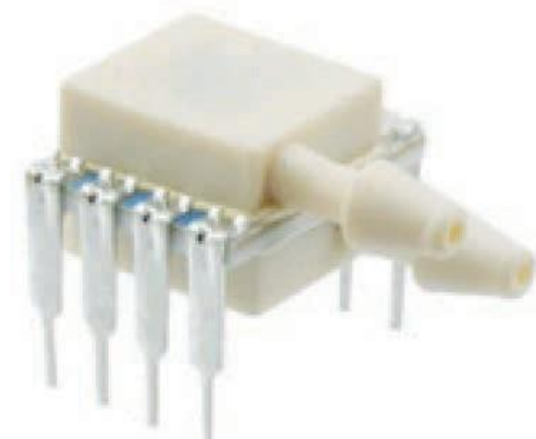


Figure 12. MS4525 differential pressure sensor.



Figure 13. Bosch BMP085 altitude/pressure absolute pressure sensor.



Figure 14. Arduino Uno R3 development micro-controller system.

4.5. DEVELOPMENT SYSTEM

The Arduino Uno was chosen as the microcontroller development system because of cost, simplicity and available hardware and software support systems.

The Arduino Uno, shown in Figure 14, is a microcontroller board based on the 16 bit ATmega328 16U2. The ATmega328 has 32 Kbytes of flash memory, of which 0.5 Kbytes is used by the boot loader, as well as 2 Kbytes of SRAM memory. The board has 14 digital input/output pins, six analog inputs, a USB connection, a power jack, an ICSP header, a reset button and a 16 MHz ceramic resonator. Bi-directional communication between the Uno and a standard personal computer is available via a USB cable. The Uno can be powered from the development computer via USB cable, with a separate AC-to-DC adapter, or by a separate battery. Operating voltage is 5 VDC.

Software support is available for Windows, MAC and Linux. The open-source Arduino Software Integrated Development Environment (IDE) allows writing code on the host computer and uploading the correctly compiled code to the board. The software environment is written in Java and other open-source software. A serial monitor is included in the Arduino software, which allows simple textual data to be sent to and from the Arduino board. When data is transmitted over the USB connection to the computer, RX (receive) and TX (transmit) LEDs on the board flash.

A SoftwareSerial library allows for serial communication on any of the Uno's digital pins. A Wire library is included in the software to simplify communication with the I2C bus. A specific library is available for SPI bus communication. The ATmega328 on the Arduino Uno comes pre-burned with a bootloader that allows uploading code without using a separate hardware programmer. The Uno PC Board is 2.7 inches long and 2.1 inches wide. The USB connector and power jack extend beyond the board edge. Four screw holes are provided for mounting the board.

4.6. BASIC DESIGN OF THE DFRDAS DATA ACQUISITION SYSTEM.

The COTS data acquisition system consists of the Arduino UNO, two Measurement Specialties MS4525 0–1 psi differential pressure sensors, a Bosch BMP085 altitude/pressure sensor and various resistors and capacitors, as detailed in the block diagram in Appendix A. The pressure

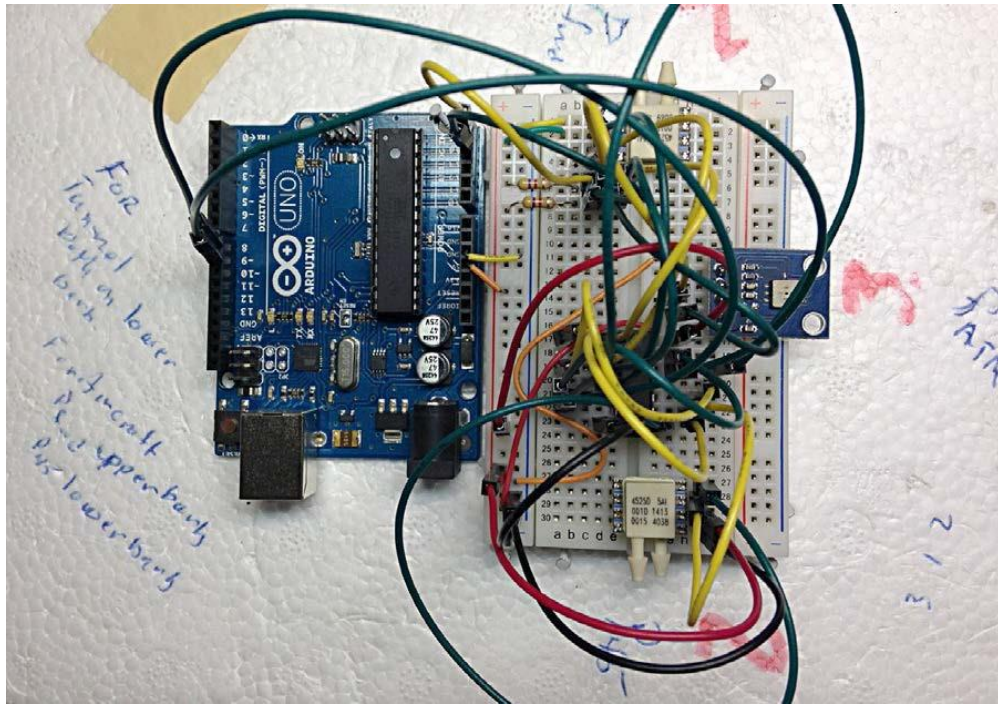


Figure 15. DFRDAS breadboard as used for wind tunnel verification tests.

sensors, Bosch BMP085 (or BMP180) and the small parts are mounted on a Proto shield which attaches to the UNO. The pinouts are also given in the block diagram in Appendix A.

4.7. SOFTWARE DESCRIPTION

A block diagram of the DFRDAS software along with a full listing of the software is given in Appendix A. The program begins with declaration of the global variables followed by setting up the pins allowing communication with the hardware. The main loop first gets the atmospheric pressure from the Bosch BMP085 or BMP180. Because only MS4525 sensors with a common I₂C address were available, it was necessary to multiplex

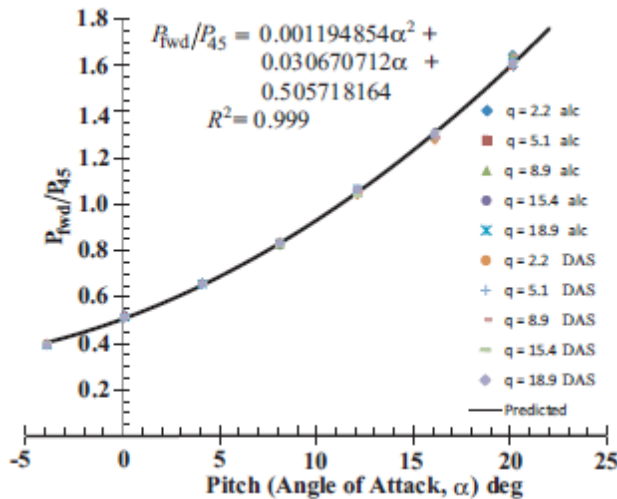


Figure 16. Comparison of wind tunnel result for the breadboard data acquisition system and the results read from the inclined manometer.

accessing the two MS4525 pressure sensors for P_{fwd} and P_{45} . The P_{fwd} and P_{45} pressure values are acquired as raw counts in the range of 0 to 16383. These values are corrected by subtracting the ‘noload’ values corresponding to zero differential pressure. The ratio P_{fwd}/P_{45} is then calculated using the ‘noload’ corrected P_{fwd} and P_{45} values. The angle of attack, α , is then determined from the calibration equation. Finally, the result is either printed or displayed as required.

4.8. WIND TUNNEL TESTING OF THE DFRDAS BREADBOARD

To insure that the breadboard data acquisition system, shown in Figure 15, worked correctly and provided appropriate accuracy, a wind tunnel test was conducted. The angle of attack probe was set up in the wind tunnel exactly as reported by Rogers [ROG13] with the exception that the P_{fwd} and P_{45} pressure lines were T’d to the breadboard data acquisition system. Fifty samples were simultaneously collected by the breadboard data acquisition system while the inclined alcohol manometer was manually read. The angle of attack probe was pitched from -6° to 18° in four degree increments for dynamic pressures of 2.2, 5.1, 8.9, 15.4 and 19.9 inches of alcohol. The samples acquired by the breadboard data acquisition system were corrected for the noload condition and then were averaged to yield P_{fwd}/P_{45} . The local barometric pressure was used as the reference pressure for both the inclined alcohol manometer and for the MS4525 pressure sensors in the breadboard data acquisition system. The results for both the alcohol and breadboard data acquisition system are shown in Figure 16. The accuracy of the pitch attitude of the wind tunnel balance is 0.1° . Clearly, the breadboard data acquisition system is of equal or better accuracy under the flow conditions present in the wind tunnel.

Furthermore, clearly in the static environment of the wind tunnel room, using the local room atmospheric pressure as the reference pressure for the data acquisition system was satisfactory. However, considering the large variation of atmospheric pressure with altitude, the question remained: Would using the local atmospheric pressure as the reference pressure work for the MS4525 sensors?

4.9. NOLOAD ALTITUDE TEST

The breadboard data acquisition system was tested for variation in the noload (bias) values at altitudes from near sea level (15 ft) to 6000 ft in 1000 ft increments. While in steady level flight, a sample of 500 noload values was taken for both the P_{fwd} and P_{45} sensors. The standard deviation for the 500 noload values was on the order of 10 counts out of 16383 possible counts. The maximum observed change in the noload value was 22 counts. For P_{fwd} the noload count decreased slightly with increasing altitude while for P_{45} the noload count increased slightly for increasing altitude. These changes are small and are attributed to individual sensor calibration by the manufacturer and possibly to temperatures changes with altitude. The maximum observed change represents approximately 0.1% of full scale for the sensor.

5. ROAD TESTS

The wind tunnel used for the angle of attack probe tests is a straight through design (Eiffel) tunnel which uses the surrounding room as the plenum; the test section is sealed. Hence, both the P_{fwd} and P_{45} pressures are below atmospheric pressure. Consequently, the lower (No. 1) barb on the MS4525 is used to measure pressure. The upper barb is left open to the local atmospheric pressure.

However, in flight, P_{fwd} , at typical flight attitudes, is nominally the total pressure, i.e., the dynamic pressure plus the static pressure. In flight, the static pressure is nominally the local atmospheric pressure. Thus, P_{fwd} is normally greater than the local atmospheric pressure, and hence positive, and the lower (No. 1) barb on the MS4525 is used to measure P_{fwd} and the upper (No. 2) barb is used for the reference pressure.

If the local atmospheric pressure is used as the reference pressure for P_{45} , the result is not as clear. If the pressure at P_{45} is less than the local atmospheric pressure, then, when corrected for the noload value, a negative value of P_{45} results. If that is the case, then solving the quadratic calibration equation given in Figure 16 is problematic, especially at the low dynamic pressures associated with speeds near stall.

Consequently, a rig was developed which, mounted on a truck, allowed testing the breadboard data acquisition system at low speeds. The rig consisted of a PVC pipe attached to a pair of roof racks on the truck cab. The pipe projected forward approximately over the truck hood. The probe was mounted to the forward end of the PVC pipe.

Road tests were conducted at 25 and 60 mph for all four possible barb connections. The results suggested that both P_{fwd} and P_{45} are positive for the anticipated probe pitch angles. Hence, both P_{fwd} and P_{45} pressure sensors were connected to the lower No. 1 position, as shown in the MS4525 data sheet [MS45] for the flight tests. In addition, the turbulence on the highway was clearly shown in the acquired data which suggested that the DFRDAS was both fast enough and sensitive enough.

6. PROOF OF CONCEPT FLIGHT TEST

An initial proof of concept flight test was conducted at Bay Bridge Airport (W29) on 21 & 22 January 2015. The purpose of the flight tests was to confirm that:

1. the DFRDAS mechanically and electrically worked in flight;
2. the DFRDAS had an adequate data acquisition sample rate in flight;
3. the local atmospheric pressure as the reference pressure when determining P_{fwd}/P_{45} correctly normalized the pressures;
4. the P_{fwd}/P_{45} curves for different altitudes collapsed into a single curve.

7. THE AIRCRAFT

The aircraft used was a Cessna 182Q. The aircraft was not equipped with an angle of attack/angle of sideslip (α/β) boom for these flights. A standard general aviation differential pressure angle of attack probe, as used in the wind tunnel tests, was mounted on the left wing in an inspection port centered approximately 13 in outboard of the wing strut attachment. The center of the probe inspection port was approximately four inches aft of the leading edge which placed P_{fwd} approximately at the leading edge.

Mounting the differential pressure angle of attack probe at the leading edge is outside of the manufacturer's recommendation. Mounted this far forward the probe is in the upwash field ahead of the wing. It may also be in the critical area where the surface pressure on the wing changes from positive to negative with respect to the local atmospheric pressure [GAR34] as the aircraft angle

of attack changes.

8. THE 21/22 JANUARY 2015 FLIGHTS

Two flights were conducted, one at 2000 ft pressure altitude and the second at 6000 ft pressure altitude, to confirm that the results were independent of altitude. A single DFRDAS (DFRDAS-1) data acquisition system, connected to the differential angle of attack probe mounted on the left wing, was used. The calibration curve from the wind tunnel test results shown in Figure 16 was coded into the DFRDAS-1 software. Raw counts from both MS4525 sensors and from the BMP85 sensor were recorded. Outside air temperature was manually recorded from the Aspen Avionics Evolution 1000.

The 4-leg GPS horseshoe heading technique [FOX95, LEW97, and ROG10] was used to acquire multiple data points for various indicated airspeeds. Indicated airspeed, altitude, manifold pressure and engine RPM were manually recorded and maintained constant for each of the legs of the 4-Leg GPS box pattern. Using the onboard fuel computer, fuel remaining was manually recorded for each leg of the 4-Leg GPS pattern.

True airspeed was determined from the GPS ground speed on four headings 90-degrees apart. Aircraft weight for each of the four GPS legs was determined by subtracting the fuel used from the initial aircraft weight.

The flight test points were chosen based on the best glide velocity from the pilot operating handbook [POH] at full gross weight, i.e., $V_{L/D_{max}} = 71$ kts ($\alpha_{L/D_{max}} \approx 12^\circ$). An additional test point was Carson Cruise, i.e., $V_{CC} = 1.32 V_{L/D_{max}} \approx 95$ kts ($\alpha_{CC} \approx 7^\circ$). Additional points fleshed out the data at intermediate, slower and faster speeds.

8.1. PHYSICS BASED DETERMINATION OF ABSOLUTE ANGLE OF ATTACK

From the basic definition of the lift coefficient we have

$$C_L = a\alpha = n \frac{W}{S} \frac{1}{(1/2\rho V^2)} = n \frac{W}{S} \frac{1}{q} \quad \text{which yields} \quad \alpha = 2 \frac{1}{a} \frac{n}{\rho} \frac{W}{S} \frac{1}{V^2} \propto \frac{1}{(V^2)}$$

where C_L is the lift coefficient, a is the lift curve slope, α is the absolute angle of attack, W is the weight of the aircraft, n is the load factor, ρ (rho) is the air density, V is the true airspeed (TAS) and S is the wing area. The Cessna 182Q wing area is $S = 174$ ft² with a span $b = 35$ ft 10 in, which yields an aspect ratio of AR= 7.38.

Here, $q = \frac{1}{2}\rho V^2$ is the dynamic pressure, i.e., the pressure resulting from the motion of the aircraft through the air. It is sometimes called ram (impact) pressure. Dynamic pressure is a force per unit area.

Noting that the true airspeed is known from the 4-leg GPS horseshoe heading calculations, then for any individual box pattern (TAS data point) flown at constant altitude, constant indicated airspeed, known weight and outside air temperature the absolute angle of attack can be determined provided the aircraft lift curve slope, a , is known.

The linear portion of the aircraft lift curve slope can be estimated from [P&H49 or And89]

$$a = \frac{a_0}{1 + \frac{a_0}{\pi AR}} = 0.081/\text{deg}$$

where a_0 is the lift curve slope of the wing airfoil section and AR is the wing aspect ratio, taper ratio and aspect ratio. The Cessna 182Q uses an NACA 2412 airfoil section, which has a sectional lift curve slope of 0.101/deg [ARR45] yields $a = 0.081/\text{deg}$ as indicated above. Aspect ratio and taper ratio reduce this value somewhat. Lifting surface theory for an aspect ratio, AR= 7.38, gives a value of 0.080/deg [WOO63 p. A65]. Hence, a lift curve slope $a = 0.080/\text{deg}$ is used for the linear portion of the CL vs α curve.

8.2. THE RESULTS OF THE 21/22 JANUARY 2015 FLIGHT TESTS

The results for the 21/22 January 2015 proof of concept flight tests are shown in Figure 17. Clearly, the results for both the 2000 ft and 6000 ft pressure altitude flight collapse into a single curve. Hence, the use of the local atmospheric pressure as the reference pressure is acceptable.

The curve in Figure 17 represents a second order polynomial (parabolic) fit to both the 2000 ft and 6000 ft flight test data. The angle of attack in Figure 17 is the physics based absolute angle of attack estimate discussed above. The equation in Figure 17 represents the calibration curve for this angle of attack probe location. The angle of attack represented by the calibration curve is within the required data acquisition system accuracy of $\pm 1/4^\circ$ to $\pm 1/2^\circ$.

The highest angle of attack shown in Figure 17 is significantly lower than the stall angle of attack. If the calibration curve is continued closer to the stall angle of attack, it begins to curve upward. This upward curvature can potentially result in difficulty in solving the parabolic calibration curve for absolute angle of attack given the measured P_{fwd}/P_{45} . The measured sample rate for the DFRDAS-1, written to the file on the laptop computer, was better than 17 samples/sec.

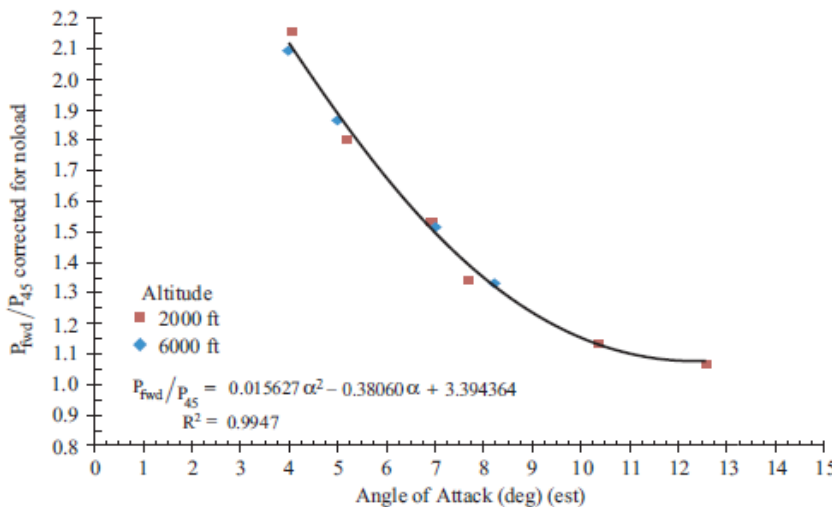


Figure 17. Combined results for the 21 and 22 January 2015 flight tests.



Figure 18. Alpha/beta probe mounted on the aircraft.

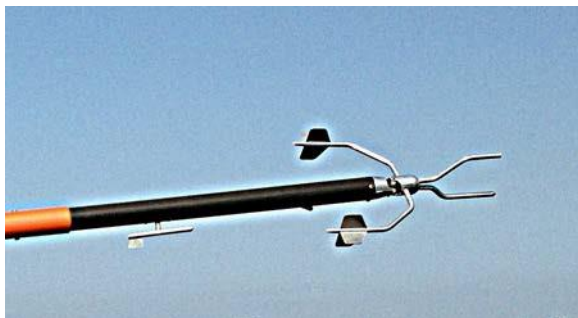


Figure 19. Alpha/beta probe head.

9. AIR DATA PROBE AND ALPHA/BETA BOOM

Subsequent to the 21/22 January 2015 flight test an air data probe was mounted on the aircraft. The air data probe consists of alpha and beta vanes and a swivel head pitot-static system. The probe extends approximately one mean aerodynamic chord length ($\approx 60 \frac{1}{2}$ inches) in front of the wing leading edge, as shown in Figures 18 and 19. Only the angle of attack and pitot-static system were used as a source for the current angle of attack study.

The air data probe was installed on the right wing tip. The probe supporting structure was integrated into the outboard rib. The supporting structure is constructed of 6061-T6 aluminum and carbon fiber. The probe was analyzed using loads in regulation 14 CFR 23.337 [CFR] for utility category (4.4G). An aerodynamic load at VD and 10 degrees angle of sideslip was superimposed and assumed as a worst case condition. Static and dynamic structural analyses were conducted. These analyses included hand calculations and finite element analysis (FEA) [FEAa] using two commercial software packages. An additional computation fluid dynamics (CFD) analysis [CFDa] was also conducted in support of the structural analysis. Selected results, as well as representative part and installation drawings, are included in Appendix B.

Ground structural testing represented the design 4.4G case. Point loads (weights) were used along the length of the probe to simulate the calculated shear and bending moment diagrams [BENa]. The FEA analysis predicted a maximum deflection of 0.219 in at the tip of the probe. During ground testing the maximum deflection was 0.288 in, which represents a 31.5% error in the calculations. Knock it off criteria for the test was set at 1 in deflection. As the boom was unloaded, the tip returned to its initial position. A post-test inspection included all brackets, fasteners and rivets on the probe, supporting structure, and the aircraft's right wing. There were no signs of cracks, fatigue or deformation in any of the inspected elements.

The aircraft data acquisition system collects data from the Inertial Measurement System (INS), Global Position System (GPS) unit, total and static digital pressure transducers, and Angle of Attack and Angle of Sideslip control position transducers. All sensor signals are interpreted by a National Instruments Compact RIO (Reconfigurable Input Output) communications module in real time at 50 Hertz. The Compact RIO simultaneously logs data in a raw format and outputs the data to the Flight Test Engineers (FTE) laptop. The laptop serves as master control module for the ERAUDAS system, as well as a data processing and logging device. The outside air temperature (OAT) and fuel quantities were manually entered on the FTE laptop throughout the flight. The laptop saves the processed data into a comma separated value file that is then reduced and

interpreted post-flight.

Ground calibrations for the total and static digital pressure transducers and angle of attack and angle of sideslip control position transducers were performed prior to first flight. All ground calibrations utilized the data acquisition system and were performed “end to end”. The angle of attack measured by the alpha/beta probe was calibrated with respect to the fuselage reference line. Details of the ground calibration setup and results are included in Appendix B.

Prior to first flight a safety review board was convened. Configuration control requests, hazard and risk assessments, and flight test cards were reviewed and approved. A safety finding and flight permit were issued. Post first flight a second safety review board was convened. The aircraft was cleared for research flights, an updated safety finding and a flight permit were issued. Details of the safety review board process are included in Appendix F.

Prior to all research data flights several in-flight calibrations were required for the air data probe. The probe pitot-static system was calibrated using a GPS 4-Leg maneuver. The probe angle of attack vane was calibrated using steady trim shots during the GPS 4-Leg maneuver. Details of in-flight calibrations, theory, practical considerations, and results are included in Appendix B.

10. THE RESULTS OF THE 22 APRIL 2015 FLIGHT TEST

A single test flight was conducted at Daytona Beach (KDAB) on 22 April 2015. Two separate DFRDAS systems were installed on the flight test aircraft. The left wing Alpha System probe location and orientation was not changed from the 21/22 January 2015 flight tests. The calibration curve from Figure 17 was implemented in the left wing data acquisition system (DFRDAS-1) software. Given P_{fwd}/P_{45} from the data acquisition system the quadratic equation in Figure 17 was solved for the angle of attack. Code was included in the DFRDAS-1 software to check for a negative radical.

Prior to the 22 April 2015 flight test a second DFRDAS (DFRDAS-2) was built and installed on the right wing of the flight test aircraft. The second DFRDAS hardware was identical to that of the first DFRDAS (DFRDAS-1). The center of the inspection port for the DFRDAS-2 was located at 38.9% of the local chord at the spanwise position shown in Figure 20. The basic software installed on the DFRDAS-2 was the same as previously installed on the DFRDAS-1 with the exception of the calibration curve. The wind tunnel calibration curve was implemented in the DFRDAS-2 software.

A seven point horseshoe heading level flight performance test was conducted at a pressure altitude of 6000 ft. Again, data points were taken at speeds corresponding the $V_{L/D\max}$, V_{CC} , $V_{PR\min}$ points and at maximum available power (117 KIAS).**

Two standard FAA idle power stalls (1 KIAS per second deceleration) were also conducted at an approximate weight of 2835 lbs. The indicated stall airspeed was 51/52 KIAS.

**The flight test aircraft is not equipped with wheel pants.



Figure 20. Spanwise location of the right wing probe DFRDAS-2.

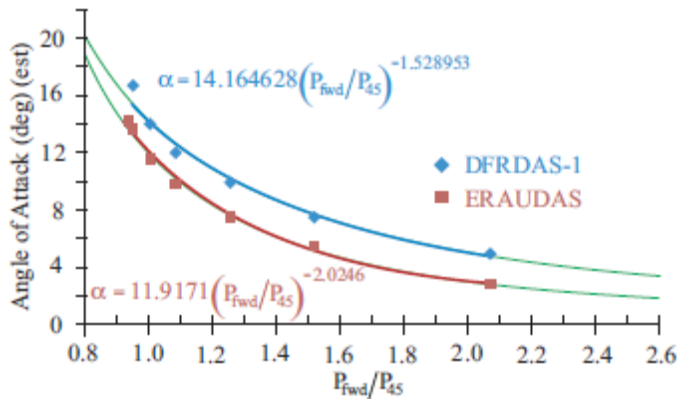


Figure 21. Alpha vs P_{fwd}/P_{45} results for the left wing DFRDAS-1 probe for the 22 April 2015 flight test.

10.1. LEFT WING DFRDAS-1 RESULTS

The calibration curve coded in the DFRDAS-1 failed to yield angle of attack values above approximately 12° because of a negative value in the square root radical. The negative square root can be eliminated by interchanging the dependent and independent variables (x and y axes) as shown in Figure 21. The results in Figure 21 are based on the horseshoe heading level flight performance test. P_{fwd}/P_{45} was calculated from the raw sensors counts corrected for noload (bias) offset using individual recorded values of P_{fwd} and P_{45} . The angle of attack was estimated using a lift curve slope of $0.08/\text{deg}$.

Here, neither a linear or second degree (parabolic) fit to the data was acceptable. A power law fit was acceptable, as is shown for both the DFRDAS-1 (blue line) and ERAUDAS (red line). The green lines represent extensions of the appropriate curve fits to both higher and lower angles of attack. The typical high speed cruise angle of attack for a retractable light general aviation aircraft is on the order of 2° . These power law fits provide adequate definition in this angle of attack range. Furthermore, the power law fits provide adequate definition in the critical angle of attack range near stall, e.g., $14\text{--}18^\circ$, as shown by the data in Figure 21. The DFRDAS-1 power law curve fit equation shown in Figure 21 is used in the next series of flight tests with the DFRDAS-1.

10.2. RIGHT WING DFRDAS-2 RESULTS

The results for the right wing DFRDAS-2 and the ERAUDAS for the horseshoe heading flight test are shown in Figs. 22 and 23. The angle of attack for the DFRDAS results was estimated using a lift curve slope of 0.080/deg. The angle of attack for the ERAUDAS results is based on the alpha/beta probe mounted on the right wing of the aircraft. The values of P_{fwd}/P_{45} are based on the individual values of P_{fwd} and P_{45} corrected for noload (sensor bias) from the DFRDAS-2 angle of attack data acquisition system. Figure 23 shows that the variation of angle of attack with P_{fwd}/P_{45} is linear.

The equation in Figure 23 was programmed into the DFRDAS-2 for use in later flight tests. The green lines in Figure 23 represent extensions of the linear fit equations also presented in Figure 23. The black triangle in Figure 23 represents the stall angle of attack determined from the alpha/beta probe mounted on the right wing and the ERAUDAS.

The wing tip alpha/beta boom is calibrated with respect to the fuselage longitudinal reference line (FRL), i.e., it is a ‘geometric’ angle of attack. The physics based angle of attack determined from the horseshoe heading tests is the absolute angle of attack of the aircraft. The constant term in the fit equations in Figure 23 suggests that the angle of zero lift with respect to the aircraft FRL is $\approx -2.4^\circ \pm 0.05^\circ$.

Figure 24 shows angle of attack plotted against the differential pressure $P_{fwd}-P_{45}$. This particular presentation is of interest because a number of differential pressure-based angle of attack systems correlate the differential pressure to angle of attack. Figure 24 clearly shows that the angle of attack varies parabolically with differential pressure. Presented as $P_{fwd}-P_{45}$ illustrates that in the stall region the correlation of angle of attack with $P_{fwd}-P_{45}$ is approximately linear. However, at angles of attack below the stall region Figure 24 clearly illustrates that the correlation is parabolic. Hence, at the lower angles of attack a linear correlation/calibration provides inadequate accuracy. Thus, differential angle of attack systems that use a linear correlation with $P_{fwd}-P_{45}$ are essentially only stall warning devices which are inadequate for other flight regimes.

It should be further noted that normalizing the differential pressure with P_{45} (not shown) eliminates the dependence on dynamic pressure and results in a linear variation.

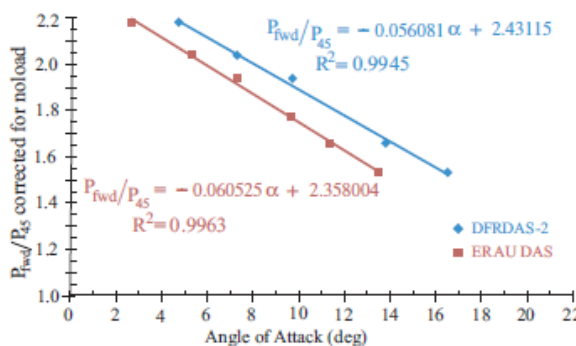


Figure 22. Alpha vs P_{fwd}/P_{45} results for the right wing DFRDAS-2 probe for the 22 April 2015 flight test.

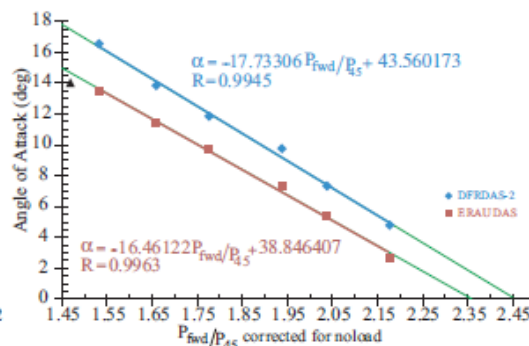


Figure 23. P_{fwd} / P_{45} vs Alpha results for the right wing DFRDAS-2 probe for the 22 April 2015 flight test.

11. STALL FLIGHT TESTS

Two stall flight tests in the clean configuration were conducted. The standard FAA deceleration of approximately one knot per second from approximately 90 KIAS was used. The stall warning horn activated at approximately 58 KIAS. Stall occurred at approximately 51 KIAS.

The results for both tests are shown as CL vs α curves in Figure 25. The angle of attack used in Figure 25 is from the alpha/beta probe mounted on the right wing tip referenced to the aircraft fuselage longitudinal reference line. The dashed black line intercepts the abscissa at approximately -1.75° to yield an estimate of the aircraft angle of zero lift with respect to the longitudinal reference line. The slopes recorded on Figure 25 indicate a lift curve slope of approximately $0.080/\text{deg}$, which confirms the value calculated above and used to estimate the physics-based absolute angle of attack.

Figure 26 shows data from Stall 1 acquired using the DFRDAS-2. The absolute angle of attack was determined using the calibration curve developed from the 4-leg GPS data shown in Figure 23. The P_{fwd}/P_{45} values calculated within the DFRDAS-2 during the stall flight test were used to calculate the absolute angle of attack also within the DFRDAS-1. Figure 26 centers the initial stall break at time zero, recovery was initiated at approximately three seconds and completed at approximately five second, i.e., a total of approximately five seconds from stall break to recovery completion. The maximum absolute angle of attack was approximately $19 \frac{1}{2}^\circ$ while the minimum angle of attack was approximately $6 \frac{1}{2}^\circ$. Figure 26 clearly indicates that the DFRDAS provides adequate angle of attack information during stall recovery.

12. THE RESULTS OF THE 26/27 MAY 2015 FLIGHT TESTS

Two flight tests were conducted at Stevensville, Maryland (W29) on 26 and 27 May 2015. Again, two separate DFRDAS systems were installed on the flight test aircraft. The left wing Alpha System probe location and orientation was not changed from either the January or April 2015 flight tests. The power law calibration curve (blue equation) from Figure 21 was implemented in the left wing data acquisition system (DFRDAS-1) software. Code was included in the DFRDAS-1 software to calculate the absolute angle of attack from the power law calibration equation in real time given P_{fwd}/P_{45} .

Again the DFRDAS-2 data acquisition system was used to acquire data from the differential pressure angle of attack probe mounted at 38.9% local chord on the right wing. The orientation of the right wing probe with respect to the wing lower surface was not change from the 22 April 2015 flight test. The software in the DFRDAS-2 used to determine P_{fwd}/P_{45} from the raw pressure sensor output was not changed.

The raw values of P_{fwd} and P_{45} were output to data files. These values were used to independently calculate the ratio P_{fwd}/P_{45} , and compare to those internally calculated within the DFRDAS.

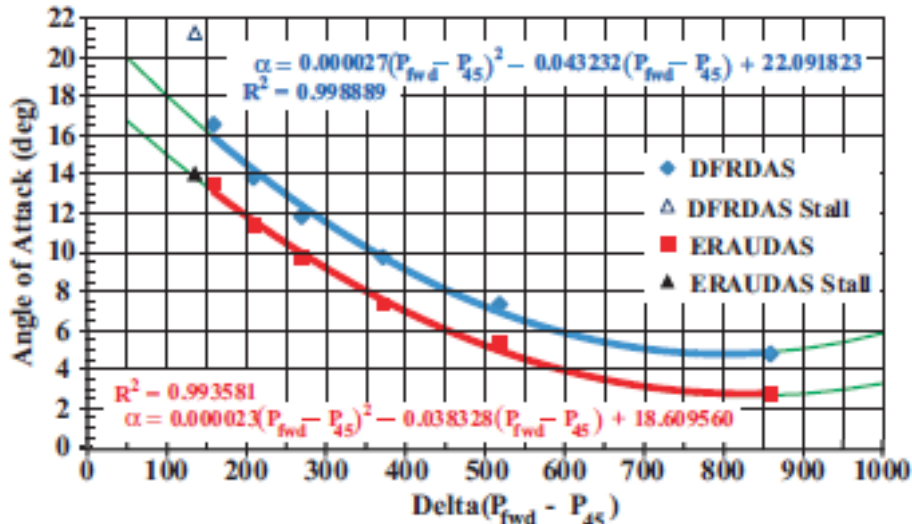


Figure 24. Alpha vs Pfwd- P45 results for the right wing DFRDAS-2 for the 22 April 2015 flight test.

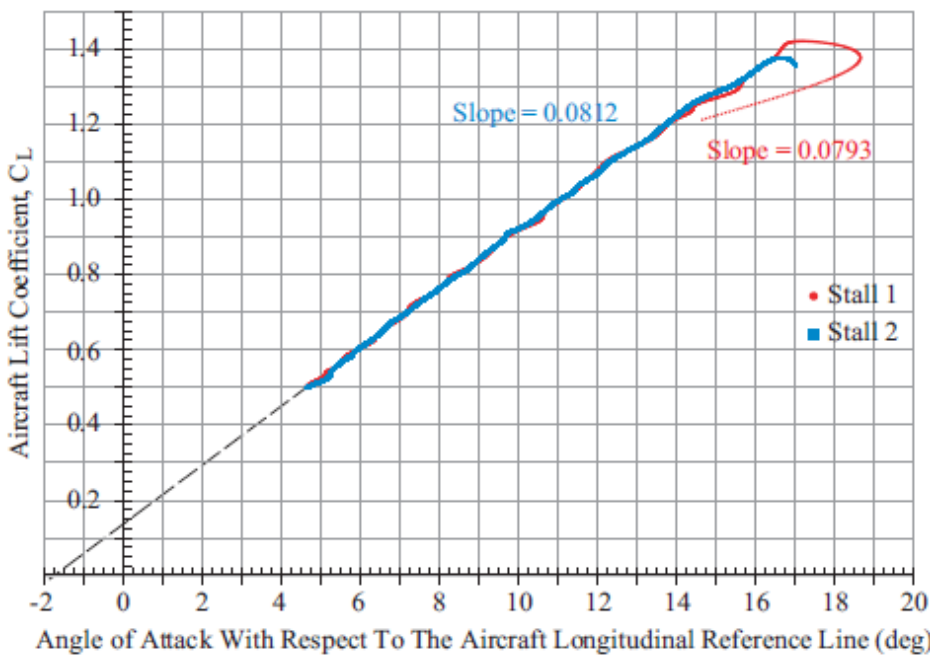


Figure 25. Lift coefficient vs angle of attack with respect to the fuselage reference line for two stall flight tests.

A seven point horseshoe heading level flight performance test was conducted at a pressure altitude of 6000 ft on 26 May 2015. Again, data points were taken at speeds corresponding to $V_{L/D\max}$, V_{cc} , V_{P_R} intermediate points and at maximum available power (117 KIAS).**

A single standard FAA idle power stall in the clean configuration was also conducted on 26 May 2015 at a nominal pressure altitude of 4500 ft

**The flight test aircraft is not equipped with wheel pants.

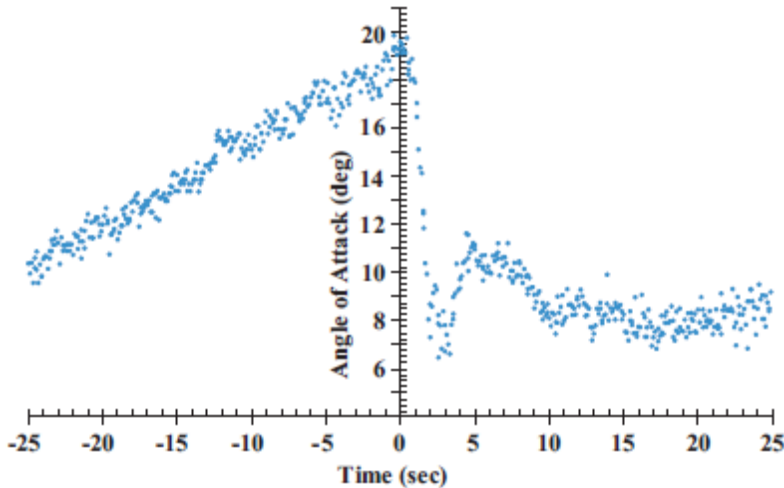


Figure 26. Absolute angle of attack vs time for Stall 1. Pfwd/P45 data is from DFRDAS-2. The absolute angle of attack is calculated using the calibration curve for the DFRDAS-2 shown in Figure 23.

The linear calibration curve from the 22 April 2015 flight test, represented by the blue equation in Figure 23, was programmed into the software for the DFRDAS-2 data acquisition system. Again, software within the DFRDAS-2 was used to determine the absolute angle of attack from P_{fwd}/P_{45} , calculated in real time by the software.

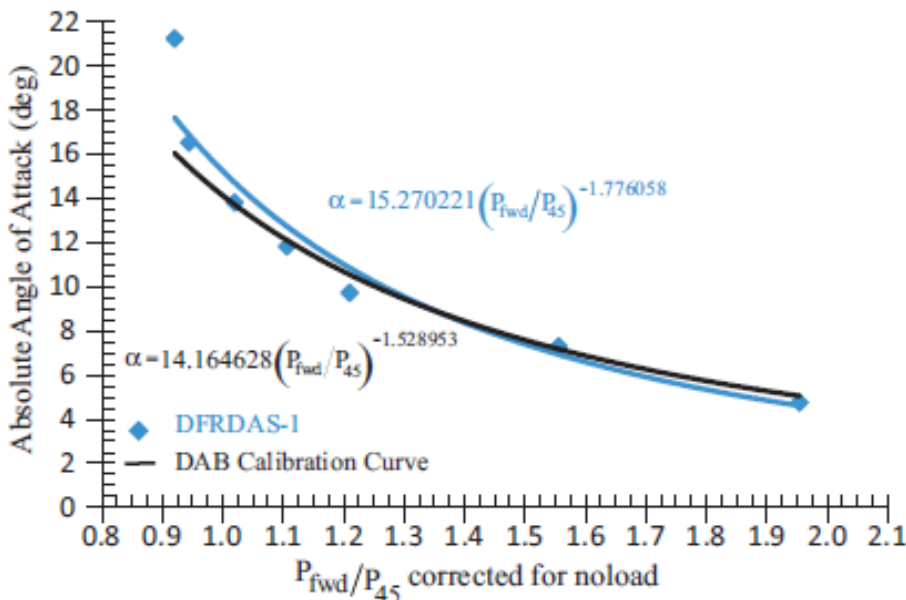


Figure 27. Absolute angle of attack vs Pfwd/P45 for the DFRDAS-1 from the 26 May 2015 flight test. The probe is mounted approximately at the leading edge of the left wing of the aircraft.

12.1. LEFT WING DFRDAS-1 RESULTS

The results for the left wing DFRDAS-1, based on the horseshoe heading level flight performance flight test, are shown in Figure 27. The blue curve and equation represents a power law fit to the data from the 26 May 2015 flight test. The black curve and equation represents the calibration curve from the 22 April 2015 flight test. Again, a lift curve slope of 0.08/deg was used to calculate the angle of attack.

The difference in angle of attack for a given value of P_{fwd}/P_{45} is likely a result of the method used to determine both the angle of attack and P_{fwd}/P_{45} . Specifically, the noload value was determined by averaging 100 data points and was not changed, nor should it have been, for the two flight tests. The 100 values for P_{fwd}/P_{45} for each leg of the 4-leg GPS horseshoe heading box pattern were averaged and then the four averaged values averaged again. The four true airspeeds determined from each of the triads of the 4-leg GPS horseshoe heading data were averaged to obtain the true airspeed for each data point. In short, the values represented by the data points are an average of an average. Finally, the calibration curve was determined by a ‘statistical’ fit to the averaged data.

The power law curves represent a reasonable approximation to the angle of attack for medium to low angles of attack, i.e., for typical cruise and approach conditions. However, notice that near stall both curves in Figure 27 become quite sensitive and tend to underestimate the angle of attack.

12.2. RIGHT WING DFRDAS-2 RESULTS

The results for the right wing DFRDAS-2 for the horseshoe heading flight test are shown in Figure 28. The angle of attack for the DFRDAS results was estimated using a lift curve slope of 0.080/deg. The values of P_{fwd}/P_{45} are based on the individual values of P_{fwd} and P_{45} corrected for noload (sensor bias) from the DFRDAS-2 angle of attack data acquisition system. Figure 28 shows the angle of attack, α , plotted against P_{fwd}/P_{45} . Again, as in the 22 April 2015 test, the variation is linear. The blue equation in Figure 25 was programmed into the DFRDAS-2 and is shown here as the black line and equation. The differences between the linear fits to the data represented by the blue and black lines is attributed to the effect of averaging the averages discussed in Appendix D.

Some of the ‘scatter’ in the data is a result of ‘ringing’ in the pressure sensors. However, a significant amount of the ‘scatter’ results from the continuous very small changes in angle of attack made by the pilot in order to maintain constant airspeed and altitude without changing power or trim during the data run.

12.3. RIGHT WING FLAPS 40° RESULTS

A four point 4-leg GPS horseshoe heading flight test was conducted at 6000 ft pressure altitude with full flaps (nominally 40°) extended. The results are shown in Figure 29. The flaps zero calibration curve from Figure 28 is shown for comparison. Figure 29 again shows a linear calibration curve with flaps extended. Figure 29 also shows that P_{fwd}/P_{45} , for a given angle of attack, is larger with flaps extended than without flaps extended. In addition, the slope of the calibration curve is approximately twice that with 40° flaps extended than without flaps extended. It is known from NACA airfoil data [ARR45] that flap extension beyond approximately 30° changes the lift curve slope. Additional flight tests at lower flap extensions may change the result seen with 40° flap extension.

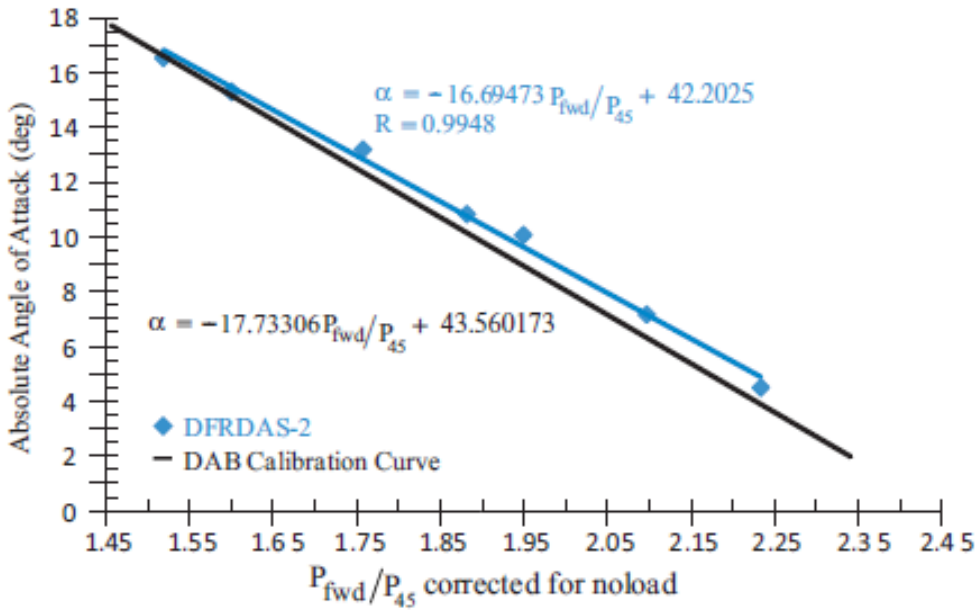


Figure 28. Absolute angle of attack vs P_{fwd}/P_{45} for the DFRDAS-2 from the 26 May 2015 flight test. The probe is mounted at 38.9% of the local chord on the right wing of the aircraft.

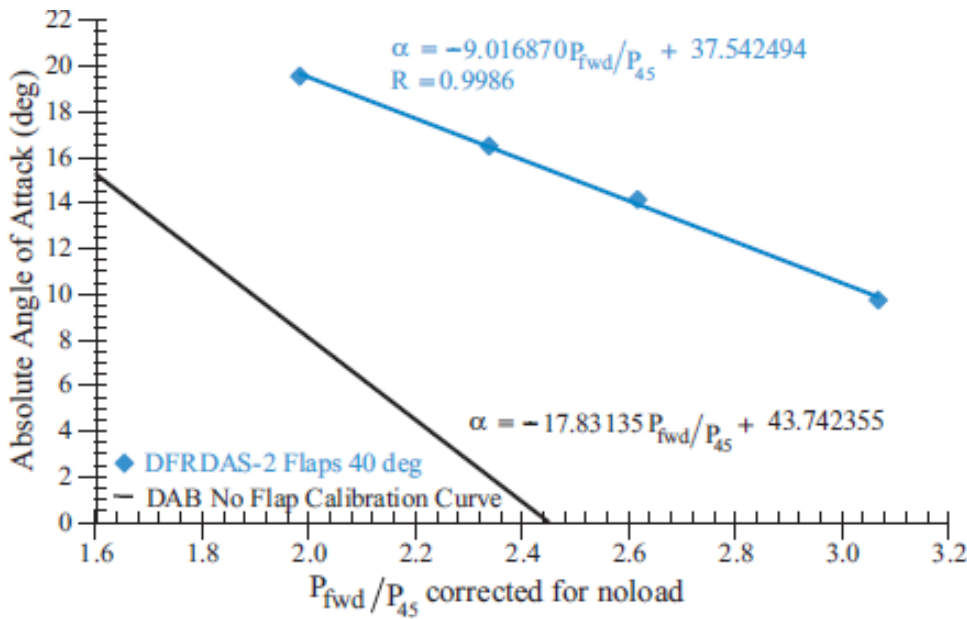


Figure 29. Absolute angle of attack vs P_{fwd}/P_{45} for DFRDAS-2 for the 27 May 2015 flight test with flaps extended to 40°. The probe is mounted at 38.9% local chord on the right wing.

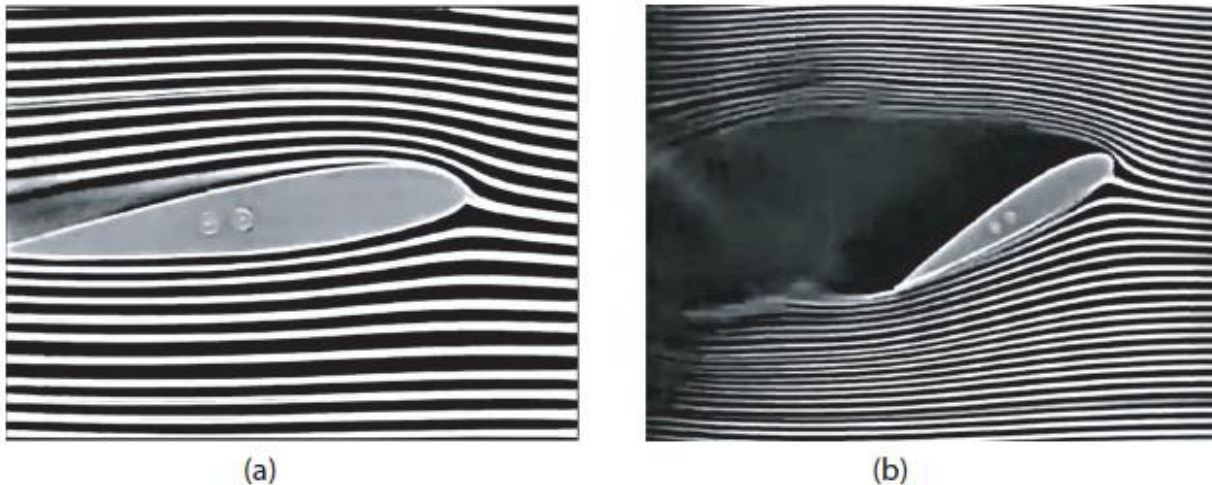


Figure 30. Two frame grabs showing the streamlines around an airfoil without flaps extended.

13. AERODYNAMICS OF WHY A LINEAR CALIBRATION CURVE?

Figure 30 shows two frame grabs (see Appendix C for additional information) from a 1938 NACA film [NACA38] that illustrate the underlying principle that results in a linear calibration curve for under wing mounted differential angle of attack probes. The airfoil in the frame grabs is a symmetrical airfoil.

The pressure on the surface of the airfoil referenced to the free stream (atmospheric) pressure is positive in the vicinity of the stagnation point but generally negative on the upper surface and may be negative or positive on the lower surface (see Figure 31). Generally, other than near the stagnation point, if the pressure relative to the atmosphere pressure is positive on the lower surface it is positive at low angles of attack near the trailing edge or when flaps are deployed.

Returning to Figure 31, notice that the pressure is typically below atmospheric pressure except near the leading and trailing edges. Hence, the pressure is increasing away from the airfoil surface. Because P_{fwd} has a significant dynamic pressure component for typical angles of attack, P_{fwd} is larger than P_{45} . Hence, provided that the angle of attack probe is mounted behind the forward stagnation positive pressure region and ahead of the trailing edge positive pressure region the P_{fwd}/P_{45} pressure ratio smoothly varies as the angle of attack changes. The data from the current flight tests suggests that the variation is linear.

Figure 32 shows several frame grabs for the video [NACA38] for the same airfoil with a flap deployed. Again, the streamlines on the lower surface are smooth and remain smooth with increasing angle of attack. Hence, the pressure field on the bottom of the airfoil is also smooth. Thus, the angle of attack probe behaves in a similar manner as without a flap deployed, as Figure 29 above confirms.

14. THE RESULTS OF THE 18/19 AUGUST 2015 FLIGHT TESTS

Additional flight tests were conducted at Stevensville, Maryland (W29) on 18 and 19 August 2015. The purpose of the flight tests was to investigate the ability of the DFRDAS to provide adequate response during the approach to, during and the recovery phases of stall.

The DFRDAS-2 was used for these flight tests. The orientation of the right wing probe (DFRDAS-2), located at 38.9% of the local chord, was not changed from the 22 April 2015 flight test. The software in the DFRDAS-2 used to determine P_{fwd}/P_{45} from the raw pressure sensor output was not changed. The software in the DFRDAS-2 used to calculate the angle of attack from P_{fwd}/P_{45} was updated with the linear calibration curve from the 26 May 2015 flight test represented by the blue equation in Figure 30.

As in all the flight tests, raw values of P_{fwd} and P_{45} were output to the data files. These values were used to independently calculate the ratio P_{fwd}/P_{45} , and compare to those calculated within the DFRDAS.

A five point horseshoe heading level flight performance test was conducted at a pressure altitude of 6000 ft on 18 August 2015. Data points were taken at speeds corresponding to $V_{L/D_{max}}$, V_{CC} , close to stall and at maximum available power (117 KIAS).

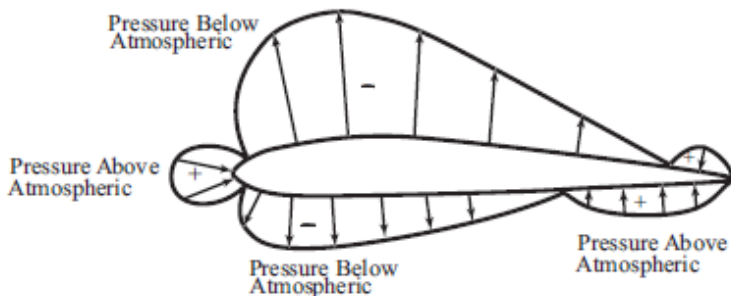


Figure 31. Sketch of the pressure distribution on the surface of a typical airfoil.

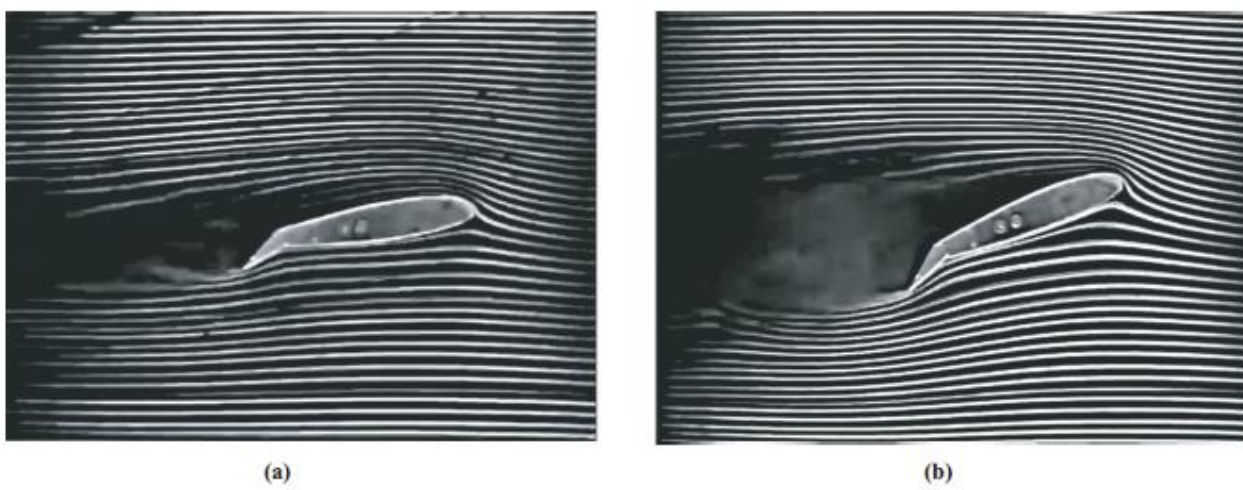


Figure 32. Frame grabs showing the streamlines around an airfoil with a flap extended.

In addition, five standard FAA stalls (1 kts/sec deceleration) were conducted in the clean configuration at 0° bank angle, left and right 20° and left and right 30 ° bank angles. Finally, two accelerated stalls (5 kts/sec deceleration) were conducted in the clean configuration.

On 19 August 2015, three standard FAA stalls were conducted with flaps extended 21.5° at 0° bank angle, right 20° and right 30° bank angles. Finally, two 5 kts/sec deceleration stalls were conducted at 0° bank angle with flaps extended 21.5° and 31°.

14.1. RIGHT WING DFRDAS-2 RESULTS

The results for the right wing DFRDAS-2 for the horseshoe heading flight test are shown in Figure 33 combined with the results from the 22-April-2015 and the 26/27 May 2015 flight tests. Individual flight test results are shown by different colored dots. The black line and the equation represents the least squares fit to all of the horseshow heading flight tests. Figure 33 clearly illustrates the repeatability of the right wing DFRDAS-2 data. Again, some of the scatter in the data is attributed to using the average of the averages of the DFRDAS-2 data stream as well as to the small continuous pilot inputs required to maintain heading, airspeed and altitude without changing the power available or trim.

14.2. STALL RESULTS

The full stall results are given in Appendix E. A selection is presented here.

Figure 34 illustrates the results for a standard FAA stall in the clean configuration. The graph is centered on the stall. The data shown are a result of a 3-point moving average. A 3-point moving average makes interpretation of the results easier. The red dots spaced along the blue line represent individual data points.

Figure 34 shows a constant angle of attack increase of approximately 0.2° per second or a deceleration of one knot per second. The stall occurs at approximately 1/2 second and recovery occurs at approximately three seconds. During the 2 1/2 second recovery approximately 30 red dot data points are displayed.

Figure 35 shows the results for a standard FAA accelerated stall, i.e., a deceleration rate of 5 kts/second or an increase in angle of attack of approximately 1.0° per second. The stall occurs at time zero with recovery (pitch down) at one second. There are approximately 16 red dots displayed during the recovery. The graph shows a characteristic angle of attack increase, of four degrees in this case, beginning at one second followed by a secondary angle of attack decrease. Recovery is completed by a smooth return to a constant angle of attack.

Figure 36 shows the results for a standard FAA stall in a right 20° bank. Stall occurs at approximately 1/4 second and the initial recovery occurs at approximately 1 1/2 seconds. There are an estimated 14 red dot data points displayed during the recovery. The maximum angle of attack recorded is approximately 19 1/2°. Recovery occurs at approximately 9 1/2° followed by the typical increase and decrease in angle of attack with a final smooth transition to level flight.

A stall was also conducted in a left 20° bank as well as left and right 30° banks with similar results. Complete results are given in Appendix E.

On 27 May 2015 a stall was conducted at zero bank angle and 40° flaps extended. At the stall the stick was held aft. The aircraft then entered a limit cycle oscillation as shown in Figure 37. After four oscillations the stick was moved forward for stall recovery. The total indicated angle of attack change during recovery was approximately 37° in approximately one second. The total number displayed red dot data points acquired, as shown in Figure 36, was 16.

These figures, along with Figure 26 clearly illustrate that the DFRDAS data acquisition rate is acceptable for all normal flight conditions as well as abusive stall cases.

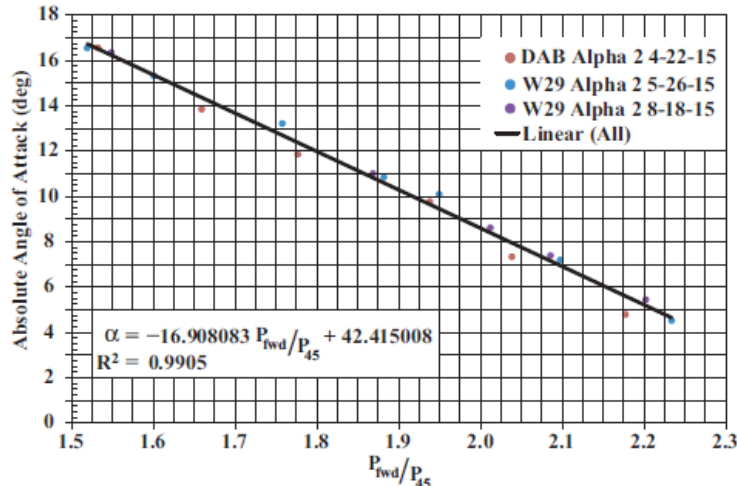


Figure 33. Combined linear fit for absolute angle of attack vs P_{fwd}/P_{45} in the clean configuration with the right hand probe at 38.9% of local chord.

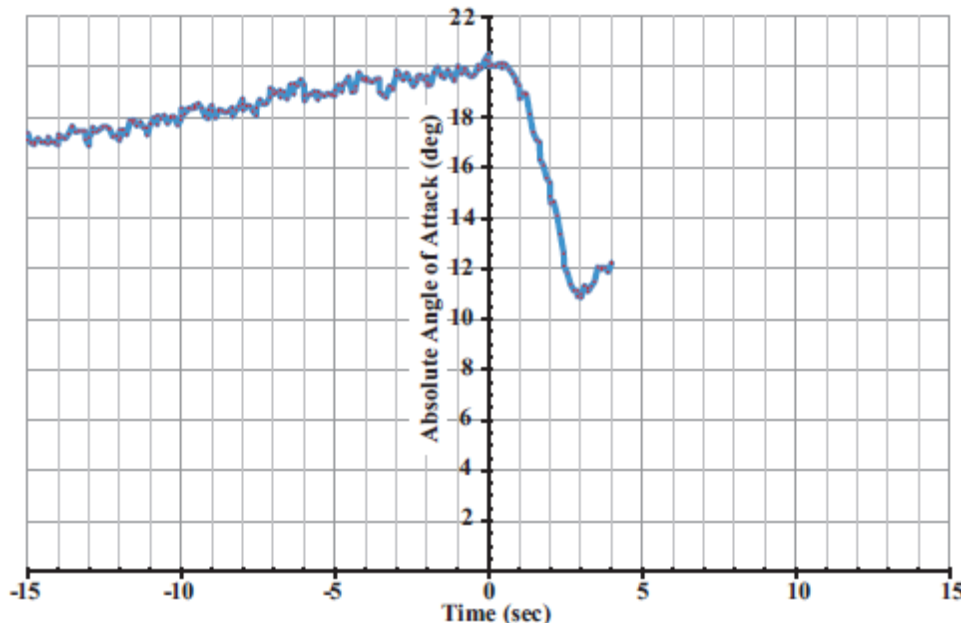


Figure 34. The DFRDAS-2 results for a standard FAA stall in the clean configuration with the probe at 38.9% of the local chord. The curve is based on a 3-point moving average of the raw data. The red dots represent individual smoothed data points.

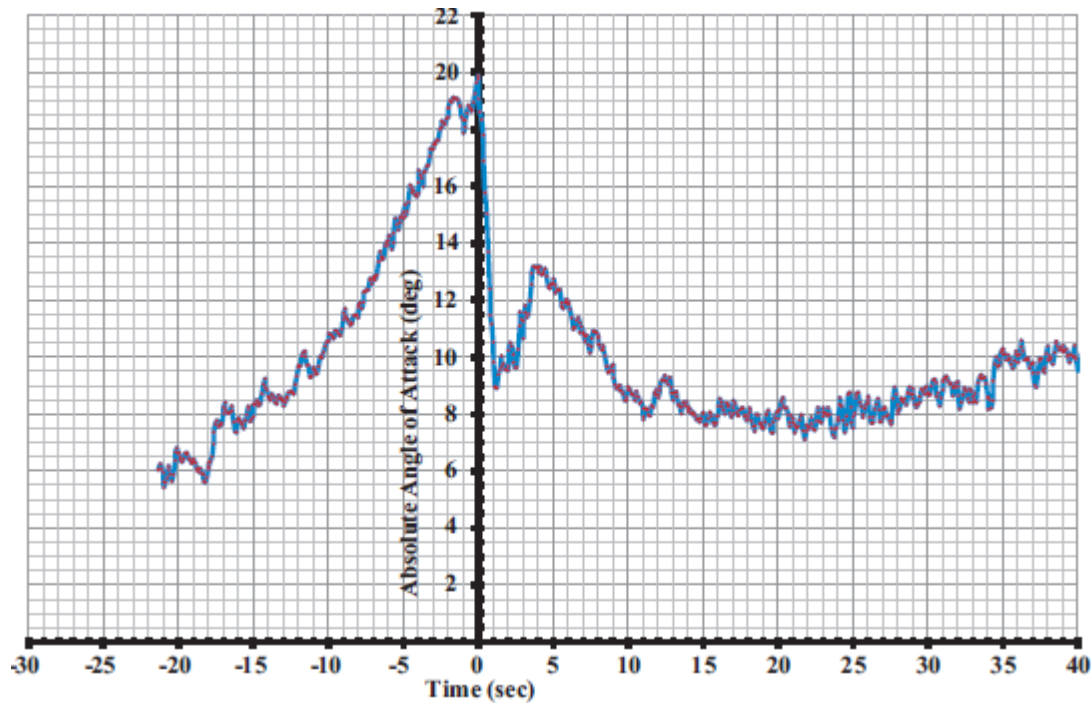


Figure 35. DFRDAS-2 results for a standard FAA stall in the clean configuration with the probe at 38.9% of the local chord. The curve is based on a 3-point moving average of the raw data. The red dots represent individual smoothed data points.

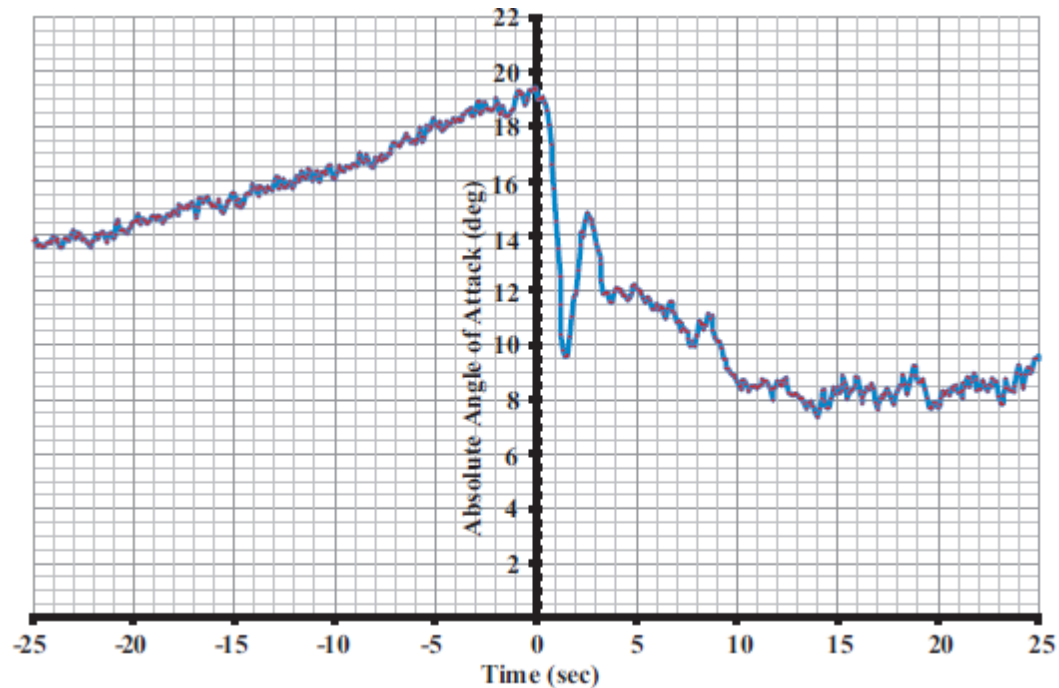


Figure 36. DFRDAS-2 results for a standard FAA stall in the clean configuration in a right 20° bank with the probe at 38.9% of the local chord. The curve is based on a 3-point moving average of the raw data. The red dots represent individual smoothed data points.

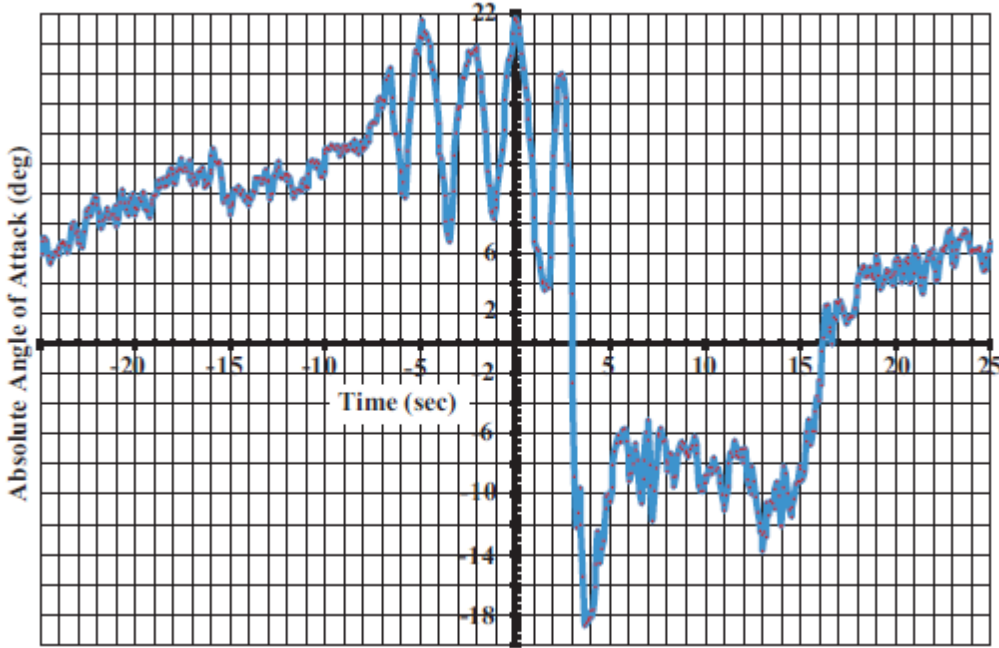


Figure 37. DFRDAS-2 results for a standard FAA stall with zero bank and 40° flap extended with the probe at 38.9% of the local chord. The curve is based on a 3-point moving average of the raw data. The red dots represent individual smoother data points.

15. WHAT WORKS AND WHAT DOES NOT WORK

Four angle of attack vs various pressure relationships were investigated. These were:

- Angle of attack vs P_{fwd}/P_{45} ;
- Angle of attack vs $(P_{fwd}-P_{45})/P_{45}$;
- Angle of attack vs $(P_{fwd}-P_{45})/q$ where q is the freestream dynamic pressure;
- Angle of attack vs $(P_{fwd}-P_{45})$, i.e. the unnormalized differential pressure.

The results from the 26/27 May 2015 flight tests for the right wing probe mounted at 38.9% of the local chord are used to illustrate which of these techniques yields an accurate angle of attack throughout the aircraft angle of attack range.

Figure 38 illustrates the results obtained for each of the independent parameters listed above. The angle of attack probe was located on the right wing at 38.9% of the local wing chord. Both the absolute angle of attack derived from the 4-leg GPS true airspeed and the geometric angle of attack referenced to the aircraft longitudinal reference line are shown. Both angles of attack show consistent behavior. The green lines in Figure 38 represent extensions of independent variable for the calibration curve above and below the flight test data.

The highest angle of attack displayed represents an indicated airspeed of 58 KIAS while the lowest angle of attack displayed represents an indicated airspeed of 117 KIAS. The aircraft POH gives 70 KIAS for the speed for L/D_{max} . The aircraft calculated angle of attack for L/D_{max} is approximately 12.4° represented by the fourth blue dot from the right in Figure 38 at an absolute angle of attack

of approximately 11.9° . The speed for Carson Cruise is estimated at 94 KIAS represented by the second blue dot from the right in the Figure 38. The estimated absolute angle of attack for Carson Cruise is 7° , again represented by the second blue dot from the left in Figure 38 at $7+^\circ$.

Figure 38a with P_{fwd}/P_{45} as the independent variable shows that linear “calibration” curves for angle of attack vs P_{fwd}/P_{45} throughout the aircraft angle of attack range. The absolute angle of attack, represented by the blue line, is consistently higher than the geometric angle of attack, as it should be, given that the angle of zero lift is negative with respect to the aircraft longitudinal reference line. Figure 38a is the best choice for a stable calibration curve. An appropriate calibration curve can be obtained by flying constant heading, altitude and power at two points. However, three or four points at approximately 1.1 to $1.2V_{stall}$, $V_{L/Dmax}$, V_{CC} and typical altitude cruise are recommended for additional accuracy.

Figure 38b with $(P_{fwd} - P_{45})/P_{45}$ as the independent variable also shows a linear calibration curve throughout the aircraft angle of attack range, as expected. After all, $(P_{fwd} - P_{45})/P_{45} = P_{fwd}/P_{45} - 1$. Notice that the slope of the $(P_{fwd} - P_{45})/P_{45}$ and the P_{fwd}/P_{45} calibration curves are essentially the same. The values of $(P_{fwd} - P_{45})/P_{45}$ were calculated from the individual values of P_{fwd} and P_{45} . There may be some advantage (or disadvantage) to directly measuring $(P_{fwd} - P_{45})$ and separately measuring P_{45} . In the latter case the issue of the reference pressure for P_{45} needs addressing. This effort was not within the scope of the current investigation.

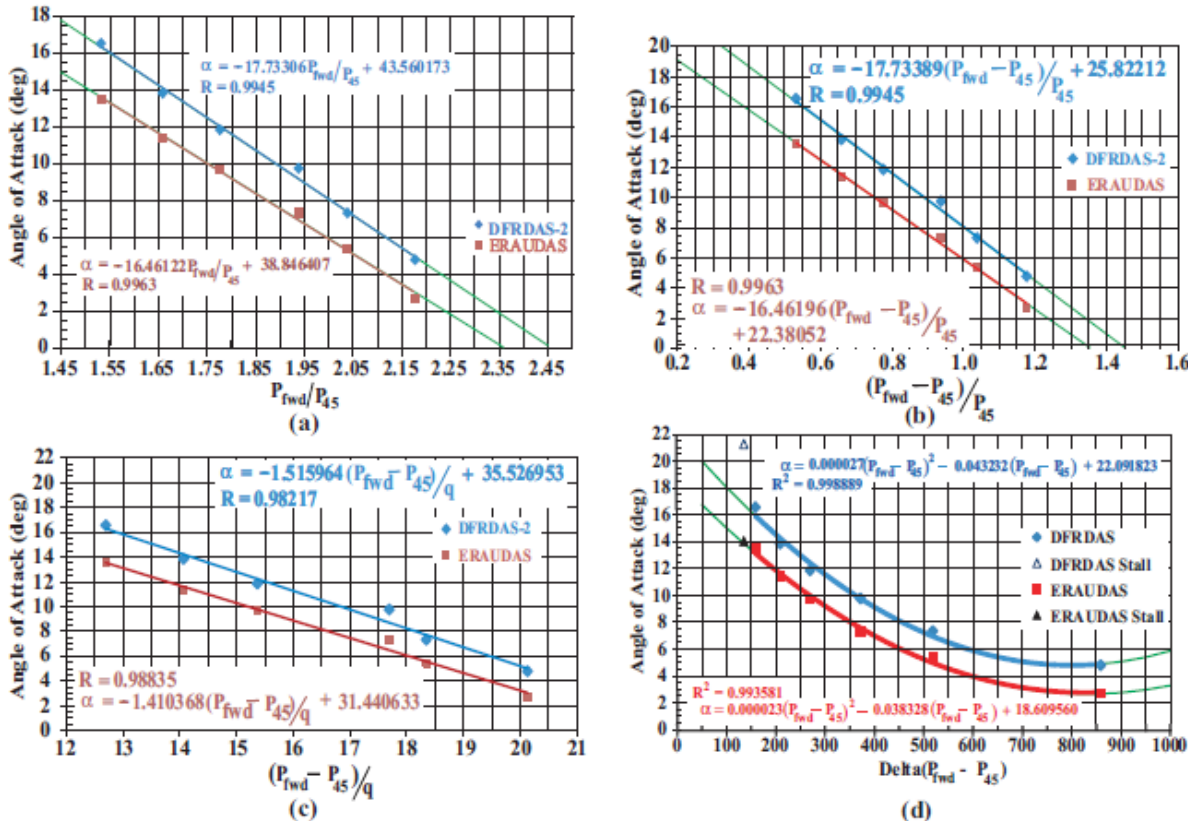


Figure 38. What works and what does not work: Angle of attack vs (a) P_{fwd}/P_{45} , (b) $(P_{fwd} - P_{45})/P_{45}$, (c) $(P_{fwd} - P_{45})/q$, (d) $\Delta(P_{fwd} - P_{45})$.

Figure 38c with $(P_{fwd} - P_{45})/q$ as the independent variable shows a linear calibration curve. Recall that $(P_{fwd} - P_{45})$ is the differential pressure and q is the freestream dynamic pressure. Specifically, q is not the dynamic pressure derived from the pitot-static system. This is a subtle, but important, point. Most aircraft pitot-static systems require correction at low speed/high angle of attack near stall because of errors in either the pitot tube and/or the static pressure readings. If these corrections are not incorporated into the angle of attack system, it is unlikely that a linear calibration with $(P_{fwd} - P_{45})/q$ results. Similar results may be expected for other differential pressure systems.

Figure 38d with simply the unnormalized differential pressure $(P_{fwd} - P_{45})$ as the independent variable does not show a linear calibration for angle of attack vs $(P_{fwd} - P_{45})$. The best fit is a second degree polynomial as shown by the red and blue lines in Figure 38d. The green lines represent extensions of the polynomial fits to both lower and higher angles of attack. In the low angle of attack (high speed) regime the polynomial fit “turns up” which results in an ambiguous angle of attack. If simple unnormalized differential pressure is used as the independent variable, a multi-point chord wise approximation using a near stall speed, V_{PRmin} , V_{LDmax} , V_{CC} , normal cruise speed and high speed cruise as suggested by Rogers [ROG13] yields acceptable results.

16. CONCLUSIONS

- a. A differential pressure based COTS angle of attack data acquisition system was designed, successfully reduced to practice, wind tunnel tested and flight tested.
- b. The accuracy of the differential pressure angle of attack system was determined to be $1/4^\circ$ to $1/2^\circ$.
- c. A data rate of 17 samples/sec or better was achieved during all the flight tests including during all phases of FAA standard and accelerated stalls, approach to stall, full stall and stall recovery.
- d. Use of the local ambient pressure as the reference for the differential pressure sensors was confirmed in practice.
- e. The repeatability of the data from the COTS data acquisition system was proven in flight test.
- f. A calibration curve based on the ratio P_{fwd}/P_{45} is linear throughout the aircraft angle of attack range if the probe is mounted in an inspection port on the bottom of the wing the center of which is located between an estimated 25% to an estimated 60% of the local wing chord. Similar results may be expected for other differential pressure systems.
- g. The linear calibration curve results because; on the lower surface of the wing, the flow remains attached and varies smoothly in the pressure field between the wing lower surface and the far field static (atmospheric) pressure below the wing throughout the entire aircraft angle of attack range including stall with and without a deflected flap.
- h. A physics based determination of angle of attack was successful, provided that a reasonably accurate aircraft lift curve is determined. Calculation of the lift curve slope was within $0.01/\text{deg}$ of the value determined by flight test using an alpha/beta probe.
- i. With the angle of attack probe mounted at the leading edge of the local chord, a power law calibration curve cast as angle of attack vs P_{fwd}/P_{45} provides a better fit to the data than a parabolic or linear fit. For a limited range of high angles of attack near stall a linear fit to the data provides adequate accuracy. However, accuracy at low angles of attack, such as required by cruise, is poor. Hence, systems, similar to that tested, mounted near the leading edge and using a linear calibration are basically only stall warning devices.

- j. Using unnormalized differential pressure ($P_{fwd} - P_{45}$) does not provide adequate accuracy throughout the aircraft angle of attack range. This technique is dynamic pressure dependent. Similar results may be expected for other differential pressure systems.

For a limited range of high angles of attack near stall a linear fit to the data provides adequate accuracy. However, accuracy at low angles of attack, such as required by cruise, is poor. Hence, systems similar to that tested, using a linear calibration are basically only stall warning devices.

- k. Normalizing the differential pressure with aircraft dynamic pressure is impractical in the aftermarket because of the necessity to include the aircraft high angle of attack (low speed) pitot-static correction to achieve the required accuracy.

17. SUGGESTED FUTURE WORK

- a. More carefully determine the acceptable local chord range for probe location. Conduct flight tests to confirm proper operation from 25% chord to 60% chord.
- b. Determine the sensitivity of the probe to flap deflection, e.g., flaps 10°, 20° and 30°.
- c. Conduct a literature search to see if studies of the lower surface far field exist.
- d. Explore the behavior of the pressure field between the lower surface of the wing and the far field using PIV, CFD and/or flight test studies.
- e. Study the effect of “ringing/jitter” in angle of attack display including the ergonomic effect on pilot acceptance and interpretation as well as techniques for reducing and/or eliminating the effect.
- f. The variation with distance from the wing of the pressure field between the lower surface of the wing and the far field is little known (see c. above), hence the distance between the P_{fwd} and P_{45} ports on the angle of attack probe may significantly influence the performance of the probe. Use CFD, wind tunnel tests and/or flight tests to explore this effect on probe performance.
- g. Conduct tests of alternate display configurations for presenting angle of attack information to the pilot.
- h. Relax the original requirement for installing the probe in an EXISTING inspection plate.
- i. Convey to the developers that only P_{FWD}/P_{45} , or $(P_{FWD} - P_{45})/P_{45}$ correctly (linear) normalizes the dynamic pressure effect.
- j. Convey to the developers that using only $P_{FWD} - P_{45}$ does NOT yield an accurate angle of attack indication. It is ONLY a stall warning device.
- k. Convey to the developers that, in their installation instructions, the probe should be mounted on the wing opposite to the standard stall warning device to provide stall warning in both a left and right hand turn.
- l. Develop an Advisory Circular on differential pressure transducer based angle of attack data acquisition systems.

18. REFERENCES

- ARR45 Abbott, I.H., von Doenhoff, A.E. and Stivers, L.S. Jr., “Summary of Airfoil Data”, NACA TR-824, 1945 also available as Abbott, I.H. and von Doenhoff, A.E., “Theory of Wing Sections Including a Summary of Airfoil Data”, Dover Publications, INC., New York, 1949, 1959.

- And89 Anderson, John D. Jr., *Introduction to Flight*, McGraw-Hill Publishing Company, New York, 1989.
- ARE09** Arend, D. J. and Saunders, J. D., "An Experimental Evaluation of the Performance of Two Combination Pitot Pressure Probes," NASA Technical Paper TP-2009-215632M, October 2009.
- BENa Online bending mount calculator <http://bendingmomentdiagram.com/>
- BOS85 BMP085 Digital Pressure Sensor Data Sheet, Bosch Sensortec Inc. USA, 2400 Geng Road - Ste. 200, Palo Alto, CA, 94303.
- CAR82 Carson, B. H., "Fuel Efficiency of Small Aircraft," *Journal of Aircraft*, Vol. 19, 1982, pp. 473–479.
- CFR "Limit Maneuvering Load Factors", sourced from <http://www.gpo.gov/fdsys/granule/CFR-2011-title14-vol1/CFR-2011-title14-vol1-sec23-337>.
- CFDa Solid Works Fluid Flow Analysis, available at www.solidworks.com
- COR53 Corning, G., "Supersonic and Subsonic Airplane Design", 2nd Edition, Third Printing, 1953.
- FEAa Solid Works Finite Element Analysis, available at www.solidworks.com
- FOX95 Fox, D., "Is Your Speed True?", *Kitplanes*, Feb. 1995, pp. 49–50.
- GAR34 Garrick, I.E., "Determination of the Theoretical Pressure Distribution for Twenty Airfoils," NACA TR-465, 1934.
- GRA58 Gracey, W, "Summary of Methods of Measuring Angle of Attack on Aircraft," NACA TN-4351, August 1958.
- LEW97 Lewis, G., "A Flight Test Technique Using GPS for Position Error Correction Testing," *Cockpit*, Jan.– March 1997, pp. 20–24
- MIL8 MILSTD-882C, "Military Standard System Safety Program Requirements," January 1993.
- MS45 MS4525DO Data Sheet, Measurement Specialties Inc., 1000 Lucas Way, Hampton, VA 23666, www.meas-spec.com.
- NACA38 NACA, "Aerodynamics: Airfoil Cambers, Flaps, Slots-Slats and Drag "Smoke Lifts", National Advisory Committee for Aeronautics, circa 1938, Langley Research Laboratory sourced from YouTube <https://www.youtube.com/watch?v=qeMQvDoDWk>.
- P&H49 Perkins, C.D. and Hage, R. E., "Airplane Performance Stability and Control", John Wiley & Sons, New York, 1949.
- POH Cessna Model 182Q Pilot's Operating Handbook, Cessna Aircraft Corporation, 1 Cessna Blvd, Wichita, KA 67215.
- ROG02 Rogers, D. F., "An Engineering Flight Test Course Emphasizing Flight Mechanics Concepts", *Journal of Aircraft*, Vol. 39, No.1, Jan–Feb. 2002, pp. 79–83.
- ROG13 Rogers, David F., "Investigation of a General-Aviation Differential Pressure Angle-of-Attack Probe," *Journal of Aircraft*, Vol. 50, No. 5, Sept–Oct. 2013, pp. 1668-1671.
- SAD11 Letter from the FAA Small Airplane Directorate, Kansas City, KS, to DepotStar Inc., dated 15 December 2011.
- WOO63 Wood, K.D., "Aerospace Vehicle Design, Vol. 1, Aircraft Design", Johnson Publishing Company, Boulder, CO, 1963.

APPENDIX A. DETAILS FOR THE ARDUINO BASED COTS SYSTEM

The COTS data acquisition system consists of the Arduino UNO, two Measurement Specialties MS4525 0–1 psi differential pressure sensors, a Bosch BMP085 altitude/pressure sensor and various resistors and capacitors, as detailed in the block diagram below. The pressure sensors, Bosch BMP085 (or BMP180) and the small parts are mounted on a Proto shield which attaches to the UNO. The pinouts are also given in the block diagram below.

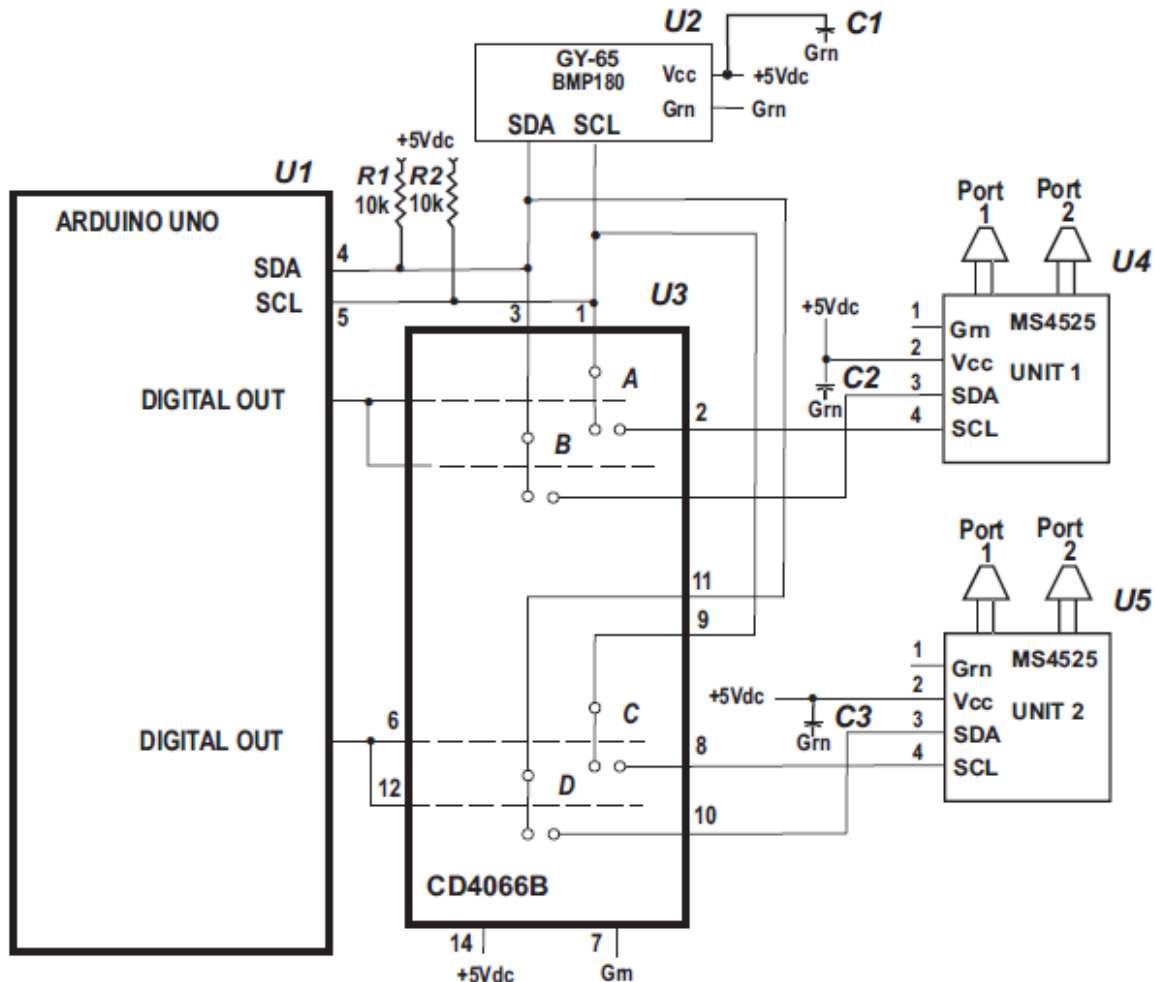


Figure A-1. Block diagram for Arduino DFRDAS data acquisition system.

A list of parts, sources and costs is given below in Table A-1.

Table A-1. Parts List and Costs—DFRDAS Data Acquisition System.

Item	Mfr	Mfr No.	Qty	Source	Cost
1 Arduino UNO R3 DIP Edition	Arduino	A000066	1	Newark Elec.	\$22.92
2 Proto Shield for Arduino UNO		STR 104B2P	1	Adafruit	\$5.00
3 Bosch GY-65 (BMP085 or BMP180)	Bosch	GY-65/BMP085	1	Component City	\$8.75
4 MS4525DO	Measurement Specialties	4525DO - DS 5AI001DP	2	Servoflo Corp	\$42.00
5 CD4066BE	Texas Instruments	CD4066BE	1	Newark Elec.	\$0.48
6 Capacitor Alum Elec 0.1 microF 35V 20%	Multicomp	MCMHR63V104MAX7	2	Newark Elec.	\$0.45
7 Cable USB 3FT	Multicomp	SPC20065	1	Newark Elec.	\$2.31
8 Resistor, Carbon Film 4.7k Ohm 0.25 W 5%	Multicomp	MCF 0.25W 4K7	2	Newark Elec.	\$0.60
9 Tubing Fitting Adapter	Avery Tools Cole-Parmer	SA-F1 EW-06365-42	2	Straight Female 1/8" Male Pipe to 1/8" Barb	\$9.42
10					\$0.92

The Arduino sketch (program) begins with declaration of the global variables followed by setting up the pins allowing communication with the hardware. The main loop first gets the atmospheric pressure from the Bosch BMP085 or BMP180. Because only MS4525 sensors with a common I2C address were available, it was necessary to multiplex accessing the two MS4525 pressure sensors for P_{fwd} and P_{45} . The P_{fwd} and P_{45} pressure values are acquired as raw counts in the range of 0 to 16383. These values are corrected by subtracting the ‘noload’ values corresponding to zero differential pressure. The ratio P_{fwd}/P_{45} is then calculated using the ‘noload’ corrected P_{fwd} and P_{45} values. The angle of attack, α , is then determined from the calibration equation. Finally, the result is either printed or displayed as required.

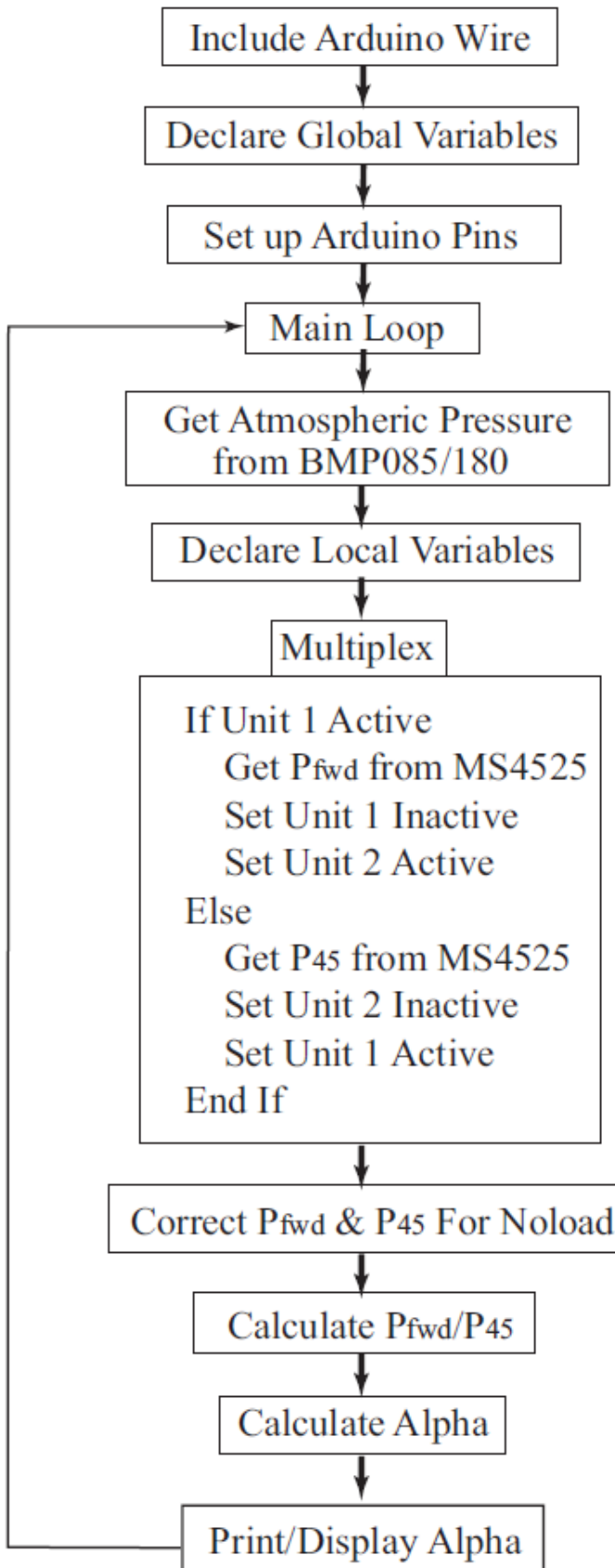


Figure A-2. Block diagram for Arduino DFRDAS data acquisition system sketch (program).

The Arduino code listing below is for the DFRDAS angle of attack data acquisition system used in the flight tests. The linear calibration ‘curve’ is based on the composite flight test curve give in Figure 41. During those flight tests the probe was mounted at 38.9% of the local wing chord. The calibration ‘curve’ should be adjusted for any other wing location (see lines 95 & 96). The noload values should be adjusted for individual sensors (see lines 98 & 99). The probe location should be between an estimated 25% and 60% of the local wing chord outboard of the wing flap.

ArduinoListing

```
1 // Name: Bar_and_Diff_pressure_V1_4_2.ino
2 // Version: 1_4_2
3 // Date: 29 July 2015
4 // Author: Francisco Rodriguez
5 // Calibration: Alpha2 Linear From DAB 5-26/2015
6
7 // Arduino 1.0+ Only
8
9 /* Based largely on code by Jim Lindblom
10
11 // Bar_and_Diff_pressure_V1_4_2
12
13 Get pressure, altitude, and temperature from the BMP085.
14 Serial.print it out at 9600 baud to serial monitor.
15 */
16
17 #include <Wire.h>
18
19 #define BMP085_ADDRESS 0x77 // I2C address of BMP085
20
21 const unsigned char OSS = 0; // Oversampling Setting
22
23 // Calibration values
24 int ac1;
25 int ac2;
26 int ac3;
27 unsigned int ac4;
28 unsigned int ac5;
29 unsigned int ac6;
30 int b1;
31 int b2;
32 int mb;
33 int mc;
34 int md;
35 float pressurepsi;
36 float altitudefeet;
37 float temperaturec;
38 int ver = 142;
39
40
41 // Definitions for Delta Pressure sensor
42
43 int press_address = 40; //1001000 written as decimal number
44 int reading = 0;
45 int mask = 63; //(0 0 1 1 1 1 1 1 )
```

```

46 int maskstatus = 192; // (1 0 0 0 0 0 0 )
47 int Status;
48 float deltapressure;
49 float deltapressure1;
50 float deltapressure2;
51
52 // Definitions for Alpha Calculations
53
54 float pfwdnoload, p45noload;
55 float pfwd, p45;
56 float pfwd_p45, Alpha; // pfwd_p45 is Pfwd/P45
57 float pfwdcorr, p45corr, Dtarepfwd,Dtarep45,deltanoloadpfwd;
58 float deltanoloadp45, psi_count;
59 float A, B;
60
61 // Definitions for LED Control
62
63 int led13 = 13;
64 int num1 = 0;
65 int led = 1;
66
67 int unit = 1; // 1 = unit1 selected, 2 = unit2 selected
68
69 // b5 is calculated in bmp085GetTemperature(...)
70 // the b5 variable is also used in bmp085GetPressure(...)
71 // so ...Temperature(...) must be called before ...Pressure(...)
72
73 long b5;
74
75 // Definition of output control
76
77 const int unit1 = 8;
78 const int unit2 = 9;
79
80
81 void setup(){ // Setup loop
82     Serial.begin(9600);
83     Wire.begin();
84
85     pinMode(unit1, OUTPUT); // set pin 8 control for sensor 1
86     pinMode(unit2, OUTPUT); // set pin 9 control for sensor 2
87     digitalWrite(unit1, LOW); // set both units off line
88     digitalWrite(unit2, LOW);
89
90     //-----Calibration FOR ALPHA 2 -----
91
92     //-- ALPHA 2 Right Wing Flight Test Calibration Curve
93     //-- Linear from DAB 5-26/27-2015 Alpha = A*(Pfwd/P45) + B
94
95     A = -16.908083; // These values must be adjusted for individual
96     B = 42.415008; // probes and probe locations
97
98     pfwdnoload = 8162.9; //counts Adjust these values for
99     p45noload = 8186.6; //counts the individual sensors
100
101    //-----NOTE THE BMP085 IS NOT ACTUALLY NEEDED-----
102    //-----THE SENSOR CAN BE REMOVED FROM THE DFRDAS-----

```

```

103 //-----ALONG WITH THE ASSOCIATED CODE-----
104
105     bmp085Calibration();
106     pinMode(led13, OUTPUT);
107 } // end setup loop
108
109 void loop() // Main loop
110 {
111     float temperature = bmp085GetTemperature(bmp085ReadUT()); //MUST be called first
112     float pressure = bmp085GetPressure(bmp085ReadUP());
113     float atm = pressure / 101325; // "Standard Atmosphere Sea Level Pressure"
114     float altitude = calcAltitude(pressure); // Uncompensated calculation - in Meters
115
116     // Various alternative possibilities for output from the BMP085
117
118     // Serial.print("Barometric Pressure = ");
119     pressurepsi = pressure * 0.000145037738; // convert from Pa to psi
120     altitudefeet = altitude * 3.280839895; // convert altitude from meters to feet
121     // Serial.print(pressurepsi, 6);
122     // Serial.println("psi");
123
124     // Serial.print("Barometric Pressure = ");
125     // pressurepsi = pressure * 0.000295; // convert from Pa to inHg
126     // Serial.print(pressurepsi,6);
127     // Serial.println(" inHg");
128
129     // Serial.print("Altitude = ");
130     // altitude = altitude * 3.2808; // convert from Pa to inHg
131     // Serial.print(altitude,2);
132     // Serial.println(" feet");
133     // -----
134     // Serial.print(pressurepsi);
135
136     Serial.print(altitudefeet,2);
137     Serial.print(",");
138
139     if ( num1 > 5 ) // Discard initil 5 inputs for stability
140     {
141         led =-led;
142         num1 =0;
143
144         // Multiplex the two MS4525 pressure sensors
145
146         if (led < 0)
147         {
148             digitalWrite(led13,HIGH);
149         }
150         else
151         {
152             digitalWrite(led13,LOW);
153         }
154
155     }
156
157     num1 =num1+1;
158
159 //-----

```

```

160 // Get Differential Pressure from unit 1
161
162 digitalWrite(unit1,HIGH );
163 unit=1;
164 float pfwd = MS4525Getpressure(unit); // Get Differential Pressure from unit 1
165 digitalWrite( unit1, LOW);
166
167 //pfwd =7814.83; // TEST =====
168
169 Serial.print( pfwd); // Print raw counts
170 Serial.print(",");
171
172 pfwdcorr = pfwd - pfwdnoload; // Account for no load
173
174 // Serial.print( pfwdcorr, 6); // Debuggign
175 // Serial.print(" , ");
176
177
178 //-----
179 // Get Differential Pressure from unit 2
180 digitalWrite(unit2,HIGH );
181
182 unit=2;
183 float p45 = MS4525Getpressure(unit); // Get Differential Pressure from unit 2
184 digitalWrite( unit2, LOW);
185
186 //p45 =7926.78; // TEST=====
187
188 Serial.print( p45); // Print raw counts
189 Serial.print(",");
190
191 p45corr = p45 - p45noload; // Account for noload
192
193 // Serial.print( p45corr,6); // Debugging
194 // Serial.print(" , ");
195
196 digitalWrite(unit2,LOW);
197
198 Serial.flush(); // Clear serial port
199 // get values again.
200
201 // pfwdcorr=1; // TEST=====
202 // p45corr=-2; // TEST=====
203
204
205 pfwd_p45 = pfwdcorr/p45corr;
206
207 // Serial.print(pfwd_p45,10);
208 // Serial.print(" -----, ");
209
210 //-----TEST-----
211 // pfwd_p45 = 2.1;
212 //-----END TEST-----
213
214 Serial.print(pfwd_p45,5);
215 Serial.print(" , ");
216

```

```

217 //---- Calculate Alpha From P fwd/P45 -----
218
219 Alpha = A*(pfwd_p45) + B;
220
221 Serial.print(Alpha);
222 Serial.print(" , ");
223
224 Serial.print(pfwdnoload);
225
226 Serial.print(" , ");
227 Serial.print(p45noload);
228
229 Serial.print(" , V=");
230 Serial.println(ver);
231
232 // delay(1000); // Debugging
233 // Serial.print("\n");
234
235
236 } // End of main loop
237
238 // Stores all of the bmp085's calibration values into global variables
239 // Calibration values are required to calculate temp and pressure
240 // This function should be called at the beginning of the program
241
242 void bmp085Calibration()
243 {
244     ac1 = bmp085ReadInt(0xAA);
245     ac2 = bmp085ReadInt(0xAC);
246     ac3 = bmp085ReadInt(0xAE);
247     ac4 = bmp085ReadInt(0xB0);
248     ac5 = bmp085ReadInt(0xB2);
249     ac6 = bmp085ReadInt(0xB4);
250     b1 = bmp085ReadInt(0xB6);
251     b2 = bmp085ReadInt(0xB8);
252     mb = bmp085ReadInt(0xBA);
253     mc = bmp085ReadInt(0xBC);
254     md = bmp085ReadInt(0xBE);
255 }
256
257 // Calculate temperature in deg C
258
259 float bmp085GetTemperature(unsigned int ut){
260     long x1, x2;
261
262     x1 = (((long)ut - (long)ac6)*(long)ac5) >> 15;
263     x2 = ((long)mc << 11)/(x1 + md);
264     b5 = x1 + x2;
265
266     float temp = ((b5 + 8)>>4);
267     temp = temp /10;
268
269     return temp;
270 }
271
272 // Calculate pressure retrieved.
273 // Calibration values must be known.

```

```

274 // b5 is also required so bmp085GetTemperature(...) must be called first.
275 // Value returned is pressure in units of Pa.
276
277 long bmp085GetPressure(unsigned long up){
278     long x1, x2, x3, b3, b6, p;
279     unsigned long b4, b7;
280
281     b6 = b5 - 4000;
282
283     // Calculate B3
284     x1 = (b2 * (b6 * b6)>>12)>>11;
285     x2 = (ac2 * b6)>>11;
286     x3 = x1 + x2;
287     b3 = (((((long)ac1)*4 + x3)<<OSS) + 2)>>2;
288
289     // Calculate B4
290     x1 = (ac3 * b6)>>13;
291     x2 = (b1 * ((b6 * b6)>>12))>>16;
292     x3 = ((x1 + x2) + 2)>>2;
293     b4 = (ac4 * (unsigned long)(x3 + 32768))>>15;
294
295     b7 = ((unsigned long)(up - b3) * (50000>>OSS));
296     if (b7 < 0x80000000)
297         p = (b7<<1)/b4;
298     else
299         p = (b7/b4)<<1;
300
301     x1 = (p>>8) * (p>>8);
302     x1 = (x1 * 3038)>>16;
303     x2 = (-7357 * p)>>16;
304     p += (x1 + x2 + 3791)>>4;
305
306     long temp = p;
307     return temp;
308 }
309
310 // Read 1 byte from the BMP085 at 'address'
311
312 char bmp085Read(unsigned char address)
313 {
314     unsigned char data;
315
316     Wire.beginTransmission(BMP085_ADDRESS);
317     Wire.write(address);
318     Wire.endTransmission();
319
320     Wire.requestFrom(BMP085_ADDRESS, 1);
321     while(!Wire.available())
322     ;
323
324     return Wire.read();
325 }
326
327 // Read 2 bytes from the BMP085
328 // First byte will be from 'address'
329 // Second byte will be from 'address'+1
330

```

```

331 int bmp085ReadInt(unsigned char address)
332 {
333     unsigned char msb, lsb;
334
335     Wire.beginTransmission(BMP085_ADDRESS);
336     Wire.write(address);
337     Wire.endTransmission();
338
339     Wire.requestFrom(BMP085_ADDRESS, 2);
340     while(Wire.available()<2)
341     ;
342     msb = Wire.read();
343     lsb = Wire.read();
344
345     return (int) msb<<8 | lsb;
346 }
347
348 // Read the uncompensated temperature value
349
350 unsigned int bmp085ReadUT(){
351     unsigned int ut;
352
353     // Write 0x2E into Register 0xF4
354     // This requests a temperature reading
355     Wire.beginTransmission(BMP085_ADDRESS);
356     Wire.write(0xF4);
357     Wire.write(0x2E);
358     Wire.endTransmission();
359
360     // Wait at least 4.5ms
361     delay(5); // Wait 5 ms
362
363     // Read two bytes from registers 0xF6 and 0xF7
364     ut = bmp085ReadInt(0xF6);
365
366     return ut;
367 }
368
369 // Read the uncompensated pressure value
370
371 unsigned long bmp085ReadUP(){
372
373     unsigned char msb, lsb, xlsb;
374     unsigned long up = 0;
375
376     // Write 0x34+(OSS<<6) into register 0xF4
377     // Request a pressure reading w/ oversampling setting
378     Wire.beginTransmission(BMP085_ADDRESS);
379     Wire.write(0xF4);
380     Wire.write(0x34 + (OSS<<6));
381     Wire.endTransmission();
382
383     // Wait for conversion, delay time dependent on OSS
384     delay(2 + (3<<OSS));
385
386     // Read register 0xF6 (MSB), 0xF7 (LSB), and 0xF8 (XLSB)
387     msb = bmp085Read(0xF6);

```

```

388     lsb = bmp085Read(0xF7);
389     xlsb = bmp085Read(0xF8);
390
391     up = (((unsigned long) msb << 16) | ((unsigned long) lsb << 8) | (unsigned long) xlsb) >> (8-OSS);
392     //Serial.print(up);
393     //Serial.print(" , ");
394     return up;
395 }
396
397 void writeRegister(int deviceAddress, byte address, byte val) {
398     Wire.beginTransmission(deviceAddress); // start transmission to device
399     Wire.write(address); // send register address
400     Wire.write(val); // send value to write
401     Wire.endTransmission(); // end transmission
402 }
403
404 int readRegister(int deviceAddress, byte address){
405
406     int v;
407     Wire.beginTransmission(deviceAddress);
408     Wire.write(address); // register to read
409     Wire.endTransmission();
410
411     Wire.requestFrom(deviceAddress, 1); // read a byte
412
413     while(!Wire.available()) {
414         // waiting
415     }
416
417     v = Wire.read();
418     return v;
419 }
420
421 float calcAltitude(float pressure){
422
423     float A = pressure/101325;
424     float B = 1/5.25588;
425     float C = pow(A,B);
426     C = 1 - C;
427     C = C /0.0000225577;
428
429     return C;
430 }
431
432 // Get Delta Pressure from MS4525 -----
433
434 //Reads Differential Pressure from I2C Ms4525 sensor
435 //
436 float MS4525Getpressure(int unit){
437     deltapressure =0;
438
439     //Send a request
440     //Start talking to the device at the specified address
441     Wire.beginTransmission(press_address);
442     //Send a bit asking for register zero, the data register
443     Wire.write(0);
444     //Complete Transmission

```

```
445     Wire.endTransmission();
446
447     //Request 2 Byte from the specified address
448     Wire.requestFrom(press_address, 2);
449     //wait for response for 2 bytes
450
451     if(2 <=Wire.available())
452     {
453         reading = Wire.read(); // byte 1
454         //Status = reading & maskstatus; // check status
455         //Status = Status >>6;
456         //Serial.println(Status);
457
458         //if ( Status <= 0)
459         //{
460             reading = reading & mask;
461
462             reading = reading << 8; //
463
464             reading |= Wire.read(); // read byte 2
465             //Serial.print(reading);
466             //Serial.print(",");
467             deltapressure =reading;
468             //deltapressure = deltapressure/16383 - .5;
469
470             // Serial.println(pressure,4);
471             // }
472     }
473     //delay(50);
474     return(deltapressure);
475 }
```

APPENDIX B. MECHANICAL DRAWINGS, GENERAL ASSEMBLY, GROUND AND FLIGHT TESTING

The following pages contain mechanical drawings for the right wing tip air data boom. This installation is intended for Cessna 182 - N721A. The drawings represent three boom sections, three mounting blocks, three boom straps, and three L brackets, shown in Figure B-1. The L brackets are attached to the right wing tip rib using rivets per AC43.13-2B.

The blocks attach to the L brackets through the aircraft skin. The top of each block has a nut plate installed over each of the four block holes. Blocks are fastened to the nut plates with AN3 bolts. Straps are fastened to blocks with 10-32 in x 2 3/4 in bolts and associated hardware. The two most aft boom tubes are constrained with one 10-32 in x 2 3/4 in bolt and associated hardware, seen in Figures B-2 and B-3. The two swivel head boom segment and the middle boom tube are constrained with one 10-32 in x 2 1/4 in bolt and associated hardware shown in Figures B-6 and B-7.

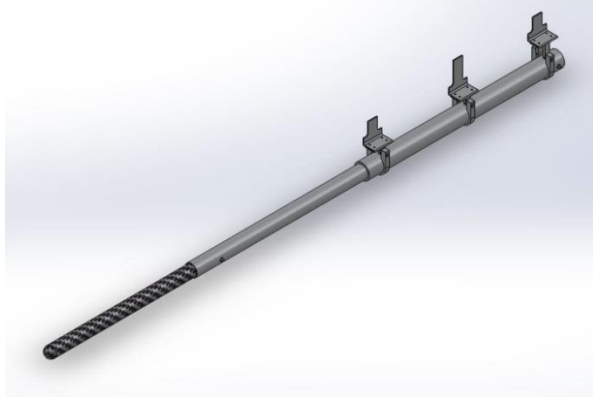


Figure B-1. Isometric view.



Figure B-2. Side view.

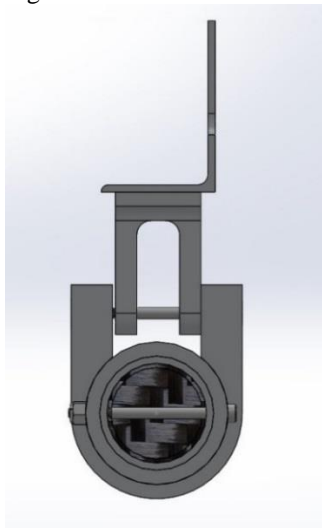


Figure B-3. Front view.

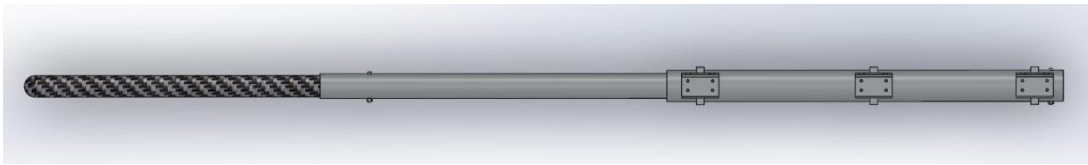


Figure B-4. Top view.

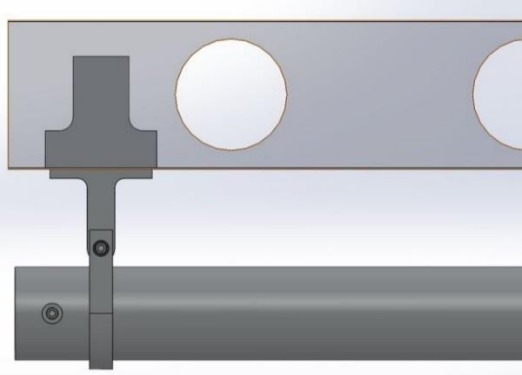


Figure B-5. Right wing tip with boom (side view). Figure B-6. Right wing tip (side view).

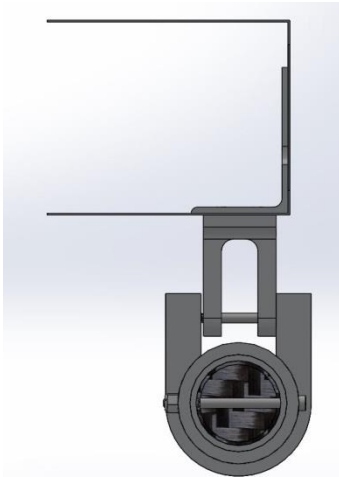


Figure B-7. Right wing tip with boom (view looking forward).



Figure B-8. Angle of attack data boom.

STRUCTURAL ANALYSIS OVERVIEW

Flight test booms are exposed to various loads during in-flight operations. The purpose of this test is to physically test the boom structural behavior on the ground. The boom is designed to withstand a 4.4g in-flight load. Details of the design and analysis are not included in this report.

The boom, shown in Figure B-8, is modeled with a swivel head at the tip, which weighs approximately 1 lb, and four sections with different distributed loads. The first section starting at the tip is made of carbon fiber, the second section consists of aluminum and carbon fiber and the remaining sections are made of aluminum. Note that sections are superimposed, which has been considered in the analysis. The boom is attached to the wing with three hinges. Inside the wing, brackets, stiffeners, and shims are used to strengthen the outboard wing rib and skin. In Figure B-9, the distributed loads for each section are shown as well as the point load due to the tip probe. The point and distributed loads represent a 4.4g in-flight load. The assumptions for the finite element analysis (FEA) are shown at the top right of Figure B-9.

Ground tests used point loads representative of the resultant forces in order to reproduce the shear and bending moment diagram shown in Figures B-11 and B-12. All point loads were rounded up to the closest available weight. The theoretical and actual loads are described in Figure B-10. Note that the actual loads are the ones in parentheses (all loads were conservative).

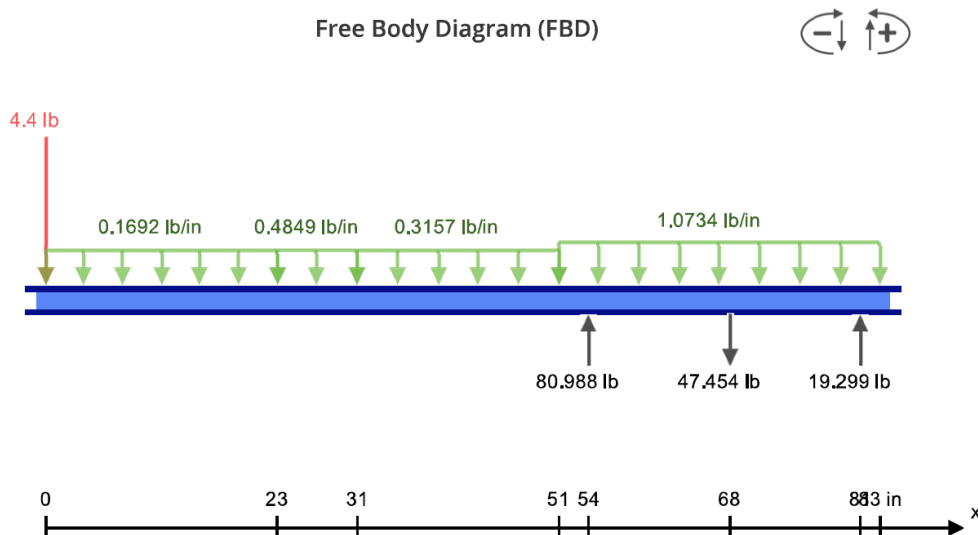


Figure B-9. Data boom free body diagram.

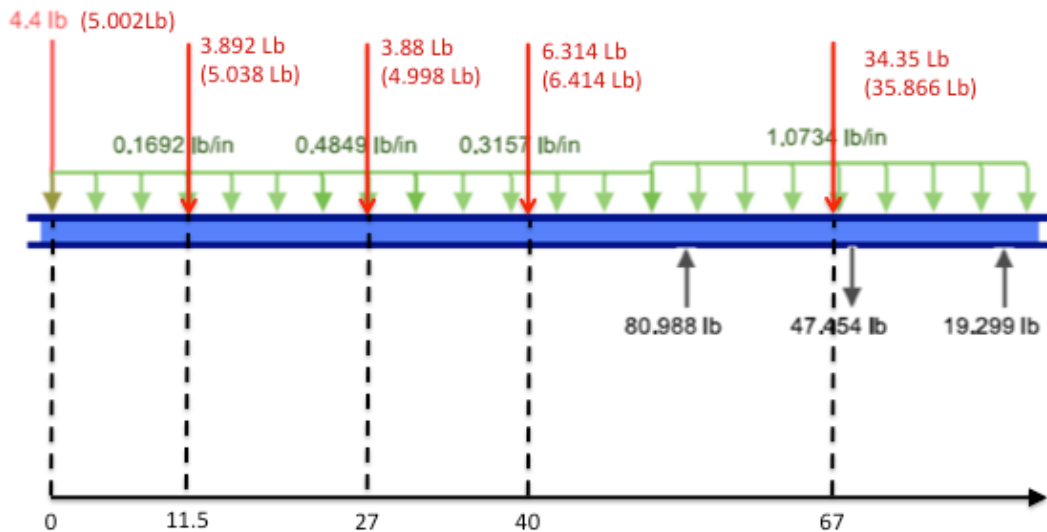


Figure B-10. Point loads magnitude and position.

A shear force and bending moment diagram were created. The highest shear force is located at point 5 in Figure B-11 with a magnitude of 59.283 lb. As expected, the highest shear force is located at the forward attachment point. Also, the maximum bending moment occurs at point 4 in Figure B-12, which is consistent with the location of the maximum shear force. The magnitude of the maximum bending moment is -594.64 lb-in.

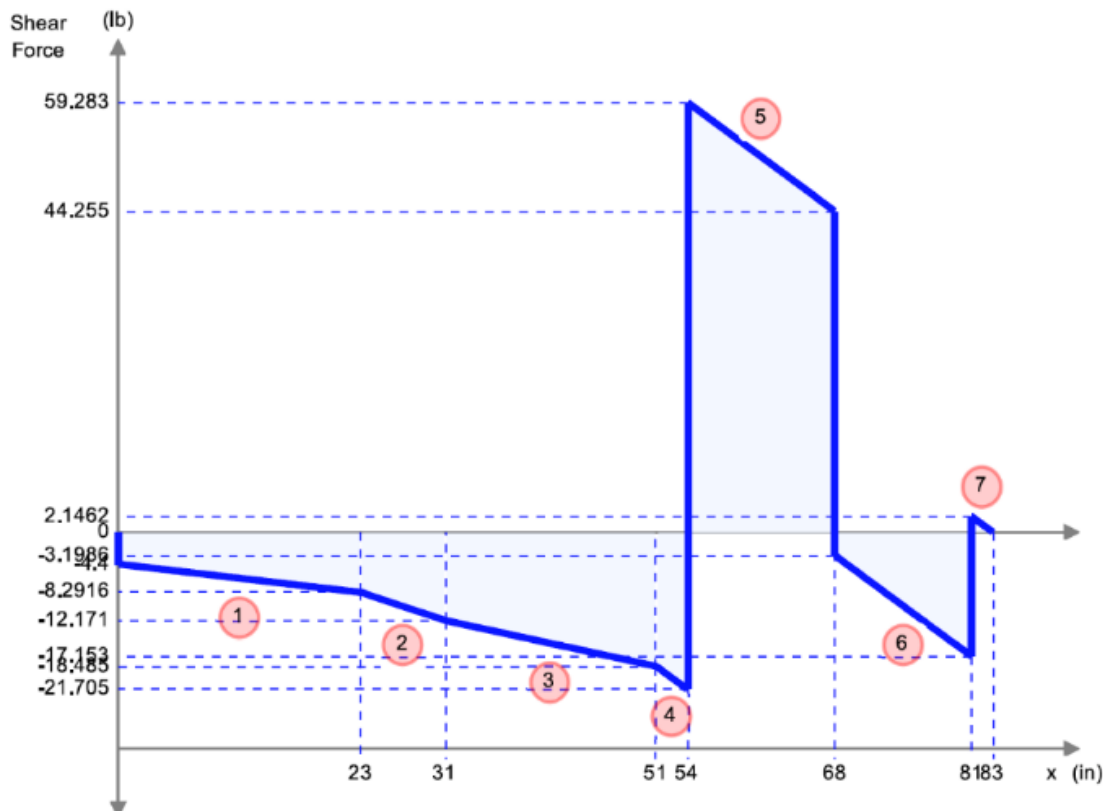


Figure B-11. Shear force diagram.

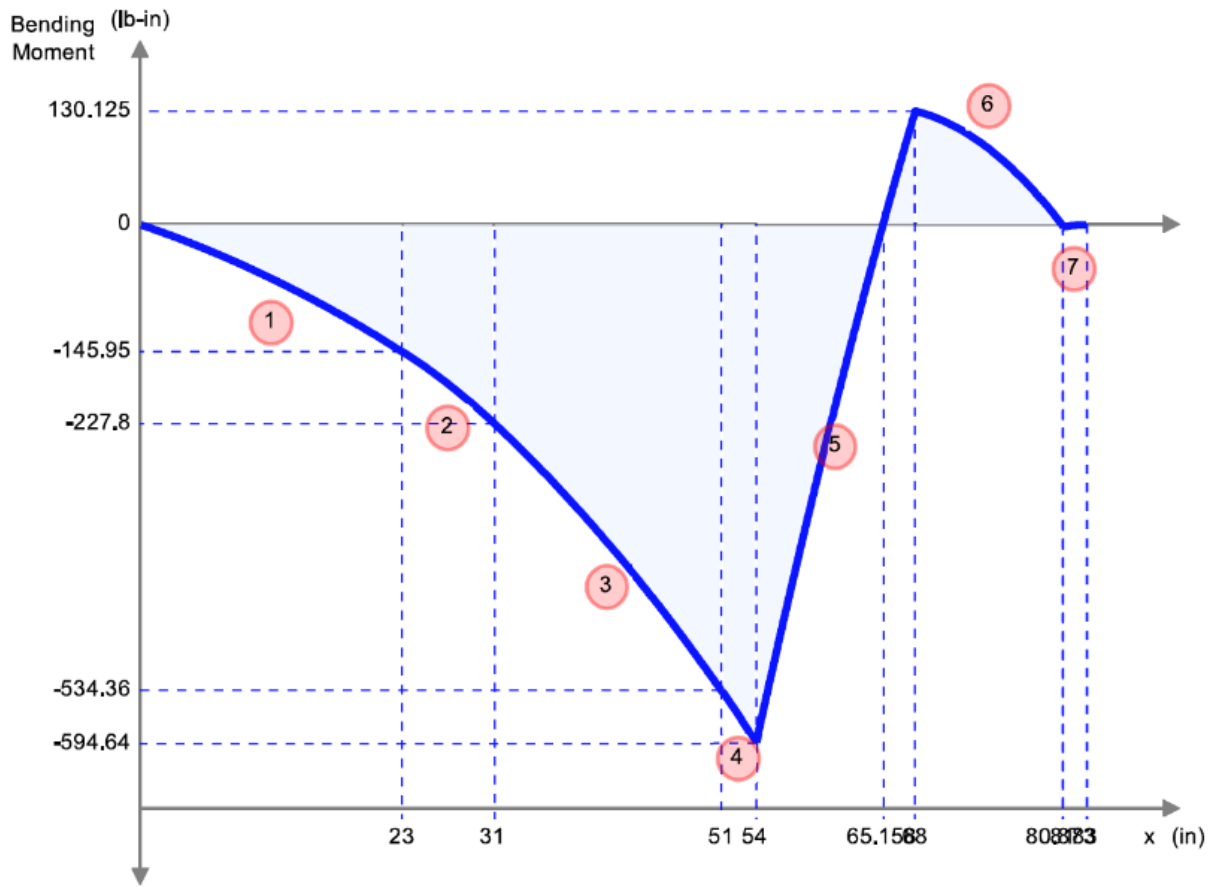


Figure B-12. Bending moment diagram.

Based on available weights, the expected deflection of the beam was 0.219 in at the tip as shown in Figure B-13. The actual maximum shear and bending moment located at the forward attachment of the boom versus wing deflection at all three connections were negligible.

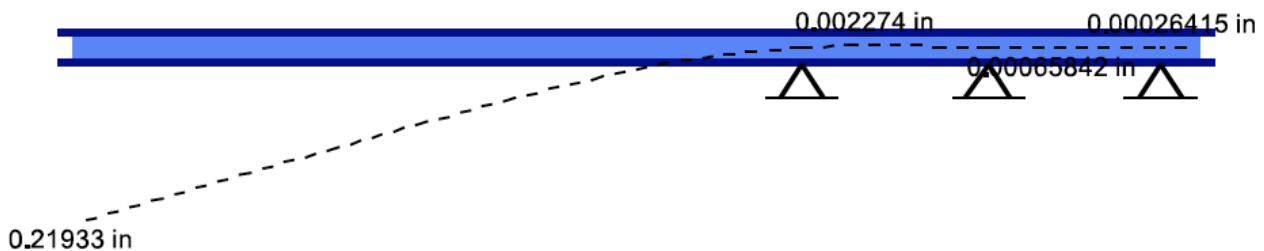


Figure B-13. Predicted deflection.



Figure B-14. Test setup with boom unloaded.

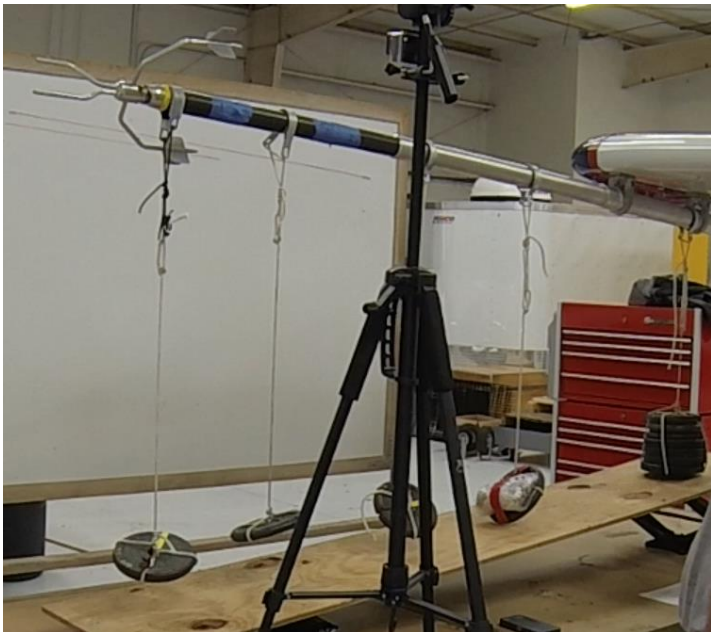


Figure B-15. Test setup – boom loaded.

TEST SETUP

With the boom mounted on the right wing point loads were placed as shown in Figure B-14. Two scissor car jacks were used to support the base holding the weights. Two rulers were vertically aligned with respect to the boom, and attached to a white board in the background. One ruler was used for tip deflection and the other ruler for root deflection. Two cameras were positioned using a level in order to align the edge of the boom with the rulers. Extra measurements were made at the leading and trailing edges. In addition, the deflection angle was measured with an inclinometer at different stations, denoted with blue tape in Figure B-15.

POINT LOADS HARDWARE

The clamps shown in Figure B-17 were covered with rubber in order to avoid scratching the boom. Each of the point loads were weighed and identified with color tape (Yellow = 5 lb, Red = 6.414 lb, No Color = 35 lb). Weights were arranged according to Figure B-18 in order to ensure each weight was attached at the right location.



Figure B-16. Rulers, clamps and inclinometer stations setup.



Figure B-17. Clamps.



Figure B-18. Weights with the correspondent clamp.

PROCEDURE

At setup completion, the leading and trailing edge were measured as well as the inclination at each marked station. Next, loads were slowly applied by lowering the base jacks progressively from root to tip using the car jacks. During the process, deformation was monitored while checking for abnormal noises. Knock it off test limits were a tip deflection of 1 in. All ground test personnel

had knock it off authority. Once all weights cleared the base, the loading was maintained for one minute. Measurements of deflection and displacement were taken again. The boom was then unloaded, detached and inspected.

Table B-1. Deflection and displacement.

	Inclination [deg]							Leading Edge	Trailing Edge
Unloaded	0.1	0.1	0.1	0.1	/	0.2	0.2	41 3/4	40
Loaded	0.1	0.2	0.4	0.5	/	0.8	0.8	41 1/2	39 3/4
Location (root to tip) [in]	8.38	22.3	37.38	49.8	66	76.8	83.00		
Unloaded deflection	0.015	0.039	0.065	0.087	/	0.181	0.203		
Loaded deflection	0.015	0.063	0.169	0.277	/	0.654	0.741	1/4	1/4
Rotation	0.000	0.024	0.103	0.190	/	0.473	0.538		
					Experimental		0.288		
					Expected		0.219		
					%ERROR		31.50		

RESULTS

Table B-1 shows the results of the measurements before and after the one minute constant load. The total deflection at the tip, using the superposition method, was 0.741 in, which approximates the measurement from the ruler located at the tip as shown in Figure B-16. However, while the boom was loaded, it experienced a rotation, which set the tip 0.203 in lower. In addition, the wing experienced a displacement of 0.25 in, which resulted in 0.288 in of actual deflection at tip.

From the finite element analysis (FEA) the expected deflection was 0.219 in at the tip, which represents a 31.5% calculation error. The limit for the test was set to 1 in deflection, leaving the resulting value within the acceptable range. The difference between the actual load (available hardware) and the true load varied from 1.5% to 29.4%. This results in a more conservative test since in-flight loads are not expected to be greater than 4.4g.

As the boom was unloaded, the tip returned to its initial position. Finally, in the post-test inspection all brackets, fasteners and rivets were checked, as well as the boom itself. There were no signs of cracks, fatigue or deformation in any of the inspected elements.



Figure B-19. Boom – tip deflection.

DATA ACQUISITION AND INSTRUMENTATION

The aircraft's data acquisition system (DAS) collects data from the Inertial Measurement Unit (IMU), Global Position System (GPS) unit, total and static pressure transducers, and Angle of Attack and Angle of Sideslip control position transducers. The IMU installed in the flight test aircraft is the Honeywell HG1700. The IMU is able to record the aircraft's velocity relative to the ground, all pitch, roll, and yaw rates and angles, and also any accelerations acting on the aircraft. For position reporting, the IMU communicates with the ProPak-V3 GPS unit, manufactured by NovAtel.

The aircraft is equipped with a Precision Differential Pressure Transducer and Precision Static Pressure Transducer (PPT's) used to measure total pressure and static pressure, respectively. These PPTs, manufactured by Honeywell, transform changes in pressure measured at the air data boom into a digital signal that is recorded by the data acquisition system (DAS). Additionally, the air data boom has an angle of attack vane and angle of sideslip vane that is attached to separate potentiometers. These potentiometers, also known as Control Position Transducers (CPT's), send angle of sideslip and angle of attack measurements to the DAS via changes in signal voltage. Similar to the PPT's, the CPTs require calibration before they can be implemented.

Once these systems were installed on the aircraft, an initial ground calibration was completed. The boom pitot and static ports were connected to a ground Pitot-Static tester and the system was tested for airspeeds between 38 and 159 knots, and pressure altitudes between -100 and 9985 feet. Furthermore, the angle of sideslip and angle of attack vanes were both tested between -90 and 90 degrees. The resulting conversion equations are given here for airspeed, pressure altitude, angle of attack, and angle of sideslip, respectively. It is important to note that boom's pitot-static system was tested and verified to be leak free, and any inherent instrument error is negligible to the subsequent analysis.

$$\begin{aligned} V_i &= 206.28 \times q_{cl}^{0.5203} \\ H_i &= -2158.7 \times P_s + 31552 \\ \alpha_i &= -0.00281 \times v_\alpha + 0.53235 \\ \beta_i &= -0.00295 \times v_\beta + 0.53892 \end{aligned}$$

The outside air temperature (OAT) and fuel quantities were manually entered into the DAS control panel on the FTE's laptop throughout flight. The fuel remaining quantities entered by the FTE were obtained from a J.P. Instruments Fuel Scan 450 fuel monitoring system. The Fuel Scan 450, which reports fuel flow, fuel used, and fuel remaining, is part of the extra instrumentation that was installed previously on the aircraft. This system has been tested and calibrated through a functional check flight prior to its use for subsequent flight testing. Lastly, the OAT was read directly off the temperature gauge on the aircraft's Aspen Evolution 1000 primary flight display.

The IMU, GPS, PPT, and CPT signals are interpreted by a National Instruments Compact reconfigurable input/output (RIO) communications module. The Compact RIO simultaneously logs this data in a raw format and outputs the data to a Flight Test Engineer's laptop. The laptop serves as both a master control module for the DAS system, as well as a data processing and logging device. The laptop saves the processed data into a comma separated value file that is then reduced and interpreted post-flight.

Table B-2 and Figure B-20 represent the sensor locations and type of data (analog / digital) used in this research.

Table B-2. Cessna 182Q instrumentation.

1	Angle of Sideslip Probe
2	Angle of Sideslip Sensor I/F Module P/N DSTR-ANGLE OF SIDESLIP-1975
3	Pitot Tube
4	Display I/F Module P/N DSTR-Angle of Sideslip-9525DDUAL
5	Port – Eagle Display/Starboard – Hawk Display
6	SMART Pressurized I/F Module P/N DSTR-Angle of Sideslip-XXXX
7	Angle of Sideslip System audio output
8	Angle of Sideslip Sensor I/F Module P/N DSTR-ANGLE OF SIDESLIP-1975
9	Angle of Sideslip Probe
10	Angle of Sideslip Vane
11	Angle of Sideslip Vane
12	Honeywell Precision Differential Pressure Transducer
13	Honeywell Precision Static Pressure Transducer
14	Static Pressure Source

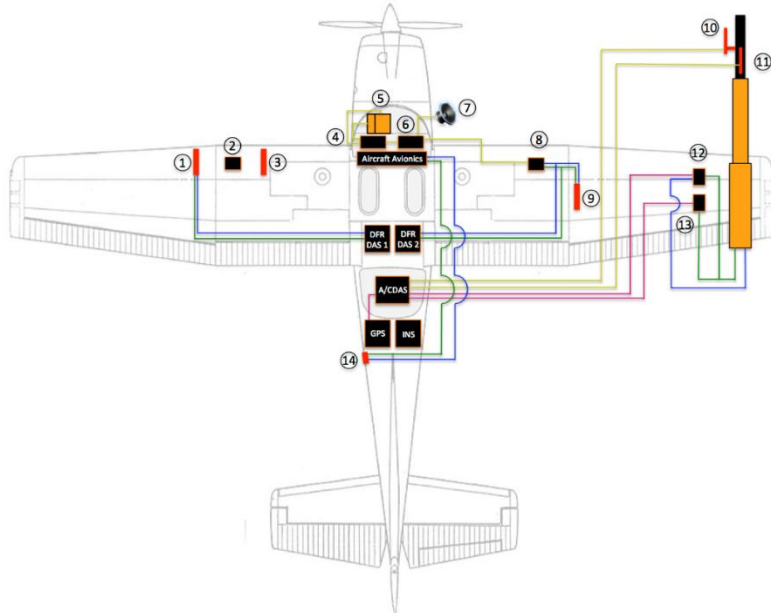


Figure B-20. Air data boom pneumatic and digital wiring.

GROUND CALIBRATION

The following static pressure calibration illustrates the ground calibration procedure. Additional calibrations (not shown) were accomplished for dynamic pressure, angle of attack, and angle of sideslip.

PPT (static pressure)

- Altitudes were commanded from the calibration unit at the ERAU maintenance center
- Altitude was increased in 1000 ft increments from 0 to 10,000 ft and back to 0
- Pressure outputs were recorded from the PPT measuring static pressure
- Commanded altitude values were read from the calibration unit and corrected according to the calibration sheet.

Table B-3. Commanded altitude vs. measured pressure.

Commanded Alt. [ft]	Static Pressure [psi]
-100	14.752
1045	14.152
1980	13.684
2990	13.188
4035	12.684
6049	11.79
6965	11.359
7960	10.944
8962.5	10.522
9985	10.113
8952.5	10.516
8000	10.914
6885	11.386
6010	11.774
5002.5	12.23
4005	12.695
3010	13.173
2010	13.666
1015	14.176
-100	14.757

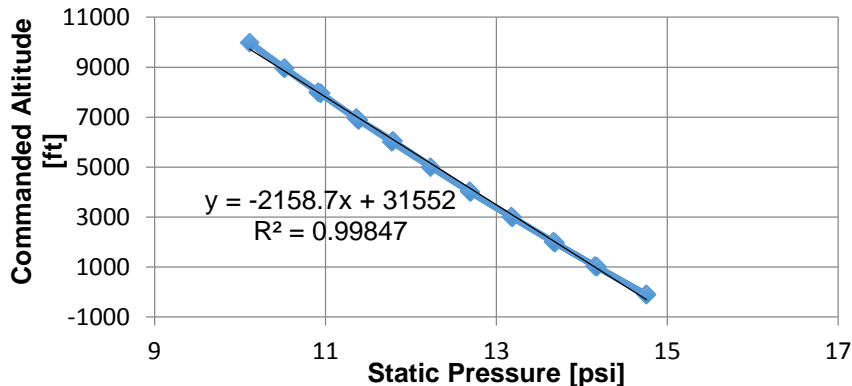


Figure B-21. Commanded altitude vs static pressure.

INFLIGHT CALIBRATION THEORY

Air Data System (ADS) Calibration

In flight test, air data sensors are commonly placed at the end of a boom to collect air data not affected by the aircraft. Although air data booms alleviate errors associated with this flow field disturbance, it is impossible to place the sensors in completely undisturbed air, because the boom would need to be longer than feasible to retain rigidity in flight.

In this flight test technique (FTT), pressure position error correction (ΔP_{PC}), airspeed static pressure position error correction (ΔV_{PC}), and static altitude pressure error correction (ΔH_{PC}) are calculated. Plots are created to show how these correction factors change with airspeed. These plots and correction factors are used in subsequent flights to obtain corrected airspeeds and altitudes.

Airspeed Correction

In order to determine the airspeed correction factor, several quantities must be computed. The first is the airspeed static pressure position error correction (ΔV_{PC}), which is the difference between calibrated and indicated airspeeds. The relationship can be mathematically represented as follows

$$V_i = V_C - \Delta V_{PC} \quad (B-1)$$

where V_C is calibrated airspeed, V_i is indicated airspeed and ΔV_{PC} is the correction factor.

Because the data for the ADS calibration was recorded over approximately two hours, the change in aircraft weight due to fuel consumption must be considered. This was done by standardizing the test results with a given reference weight. The following equation computes weight corrected velocity

$$V_{i,w} = \sqrt{\frac{W_{ref}}{W_{test}}} \quad (B-2)$$

where $V_{i,w}$ is weight corrected indicated airspeed, W_{ref} is maximum gross aircraft weight and W_{test}

is gross aircraft weight less fuel used.

At Mach numbers below 0.3 compressibility effects can be ignored. Under these conditions, true airspeed and equivalent airspeed (V_E) are assumed equal. The relationship between equivalent and true airspeed is

$$V_E = \sqrt{\sigma} \cdot V_T \quad (\text{B-3})$$

where V_T is true airspeed and σ is density ratio

Position Correction

The second correction factor is the static pressure position error coefficient. This correction nondimensionalizes the data in order to compare and graph the results of the ADS Calibration. The measured dynamic pressure is

$$q_{ci} = P_{SSL} \left(\left(\frac{\rho_{SSL} \cdot V_{i,w}^2}{(P_{SSL} \cdot 7) + 1} \right)^{\gamma/\gamma-1} - 1 \right) \quad (\text{B-4})$$

where q_{ci} is the measured dynamic pressure.

The static pressure position coefficient is calculated by taking the difference between the two dynamic pressures

$$\Delta P_{PC} = q_c - q_{ci} \quad (\text{B-5})$$

Altitude Correction

The last correction factor is the altitude static position error (ΔH_{PC}) which accounts for the altimeter static pressure error. This factor is computed using the hydrostatic equation:

$$\Delta H_{PC} = \frac{\Delta P_{PC}}{\rho g} \quad (\text{B-6})$$

Upwash Calibration

Upwash calibration is used to determine errors in the indicated angle of attack that result from upwash in the flow field. Upwash decreases ahead of the wing leading edge and, theoretically, if placed far enough forward, upwash is negligible. Theory suggests that this distance is at least 1.5 fuselage diameters ahead of the wing. Completely removing any upwash sensed by the boom would require an unfeasibly long boom. The upwash correction removes this error and obtains the true angle of attack, measured with respect to the fuselage reference line (FRL) in-flight.

Because of the way the data acquisition system (DAS) sensors are installed, other measurement errors need to be accounted for. After reducing data, a correction factor is then determined to calculate the true angle of attack, which is then compared to other angle of attack instruments to

determine its accuracy.

A direct way of calculating upwash is to compare the indicated angle of attack to the true angle of attack, given by

$$\Delta\alpha = |\alpha_T - \alpha_i| \quad (\text{B-7})$$

where α_{true} is

$$\alpha_{true} = \theta - \gamma \quad (\text{B-8})$$

where θ is pitch attitude and γ is flight path angle. The flight path angle can be determined from

$$\gamma = \sin^{-1} \left(\frac{\frac{dh}{dt}}{V_T} \right) \quad (\text{B-9})$$

During straight and level un-accelerated flight, γ is zero. This justifies the assumption that angle of attack is equal to pitch angle in straight and level un-accelerated flight. The upwash angle is calculated from

$$\Delta\alpha = \sin^{-1}(n_{xaccel} - n_{xpress}) \quad (\text{B-10})$$

where n_{xaccel} and n_{xpress} are defined respectively as

$$n_{xaccel} = n_{xb} \cos \alpha_i - n_{zb} \sin \alpha_i \quad (\text{B-11})$$

$$n_{xpress} = \frac{\dot{h}}{V_T} + \frac{V_T}{g} \quad (\text{B-12})$$

where n_{xb} is instrumented body-axis longitudinal load factor, n_{zb} is instrumented body-axis vertical load factor, \dot{h} is geometric climb rate from pressure altitude corrected for test day temperature, V_T is true airspeed, \dot{V}_T is rate of change of true airspeed, g is gravitational acceleration constant, α_i is indicated angle of attack and n_{xpress} is used to correct for small vertical velocities or accelerations that are present during steady state trim shots.

IN-FLIGHT CALIBRATION RESULTS

ADS Calibration

Table B-4. Velocity corrections as listed in the pilot's operating handbook (POH).

Airspeed	POH Values										
KIAS	50	60	70	80	90	100	110	120	130	140	150
KCAS	60	64	71	80	89	99	108	117	127	136	145
Aircraft Calculated KCAS	55.4	63.7	72.2	80.7	89.2	97.8	106.5	115.2	124.0	132.9	141.8
% Error	7.7%	0.4%	1.6%	0.8%	0.2%	1.2%	1.4%	1.5%	2.4%	2.3%	2.2%
											150.7

Table B-5. Correction values determined during ADS calibration.

Viw_DAS	PEC_DAS	dVpc_DAS	dHpc_DAS
KIAS	Unitless	Knots	Feet
119.48	0.06	3.48	41.66
93.17	0.10	4.51	42.50
79.39	0.11	4.22	33.77
71.20	0.10	3.46	24.68
65.48	0.11	3.40	22.34
61.09	0.13	3.95	24.38
59.05	0.10	2.82	16.64

Table B-4 contains the POH velocity static pressure position corrections along with the reported indicated airspeed corrections. The aircraft calibrated airspeed was calculated using the airspeeds in the reduction algorithm. For a graphical representation of these correction factors, refer to Figure B-22.

Table B-5 contains correction factors calculated using an ADS calibration reduction algorithm. These values were then used throughout the rest of the algorithm including upwash calibration and stall testing plots. Individual equations and graphical representations are included in Figures B-23, B-24 and B-25.

Figure B-22 represents the accuracy of the calculated correction factors. Various horizontal and vertical lines are used to show that both pitot and ERAU DAS indicated airspeeds (when corrected) provide the same calibrated airspeeds. These values fell within +/- 0.5 knots of each other. Figure B-23 shows the results of the ADS calibration on the trimmed DAS data.

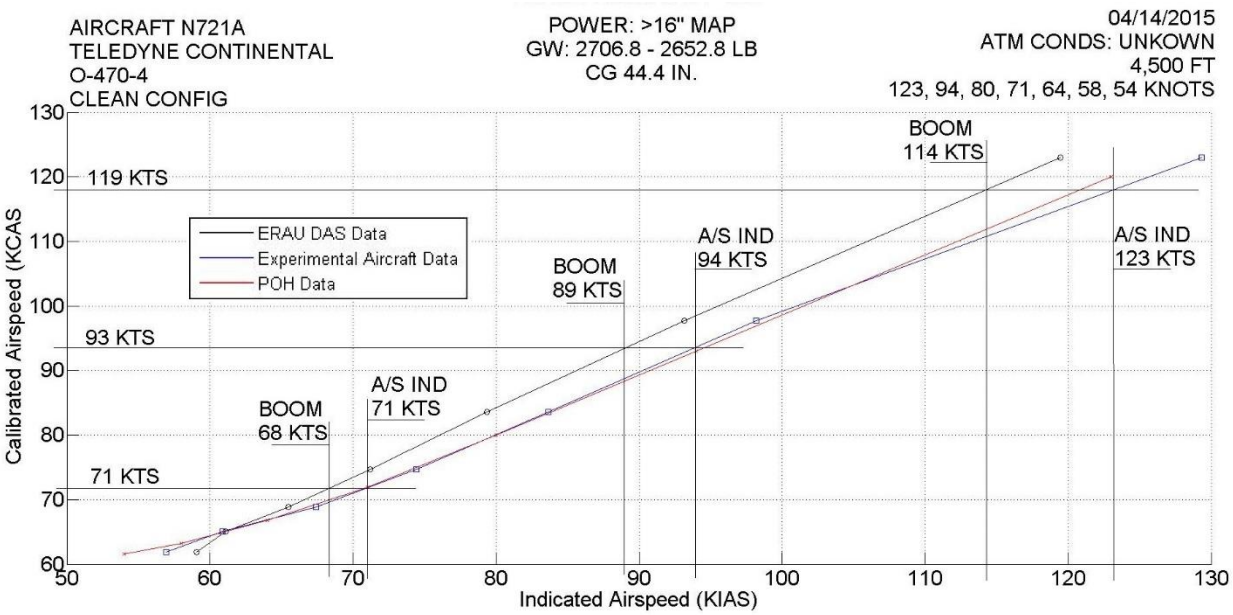


Figure B-22. Values for the POH and ERAU DAS airspeeds in graphical format.

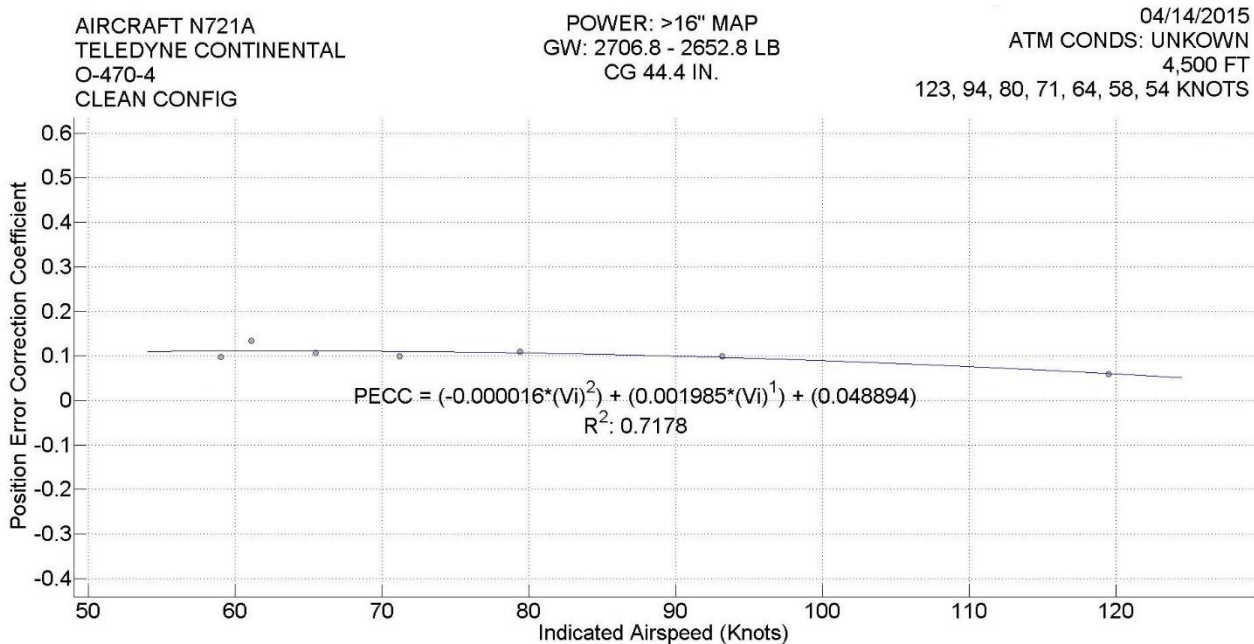


Figure B-23. Static pressure position error (Δ PPC) vs indicated airspeed.

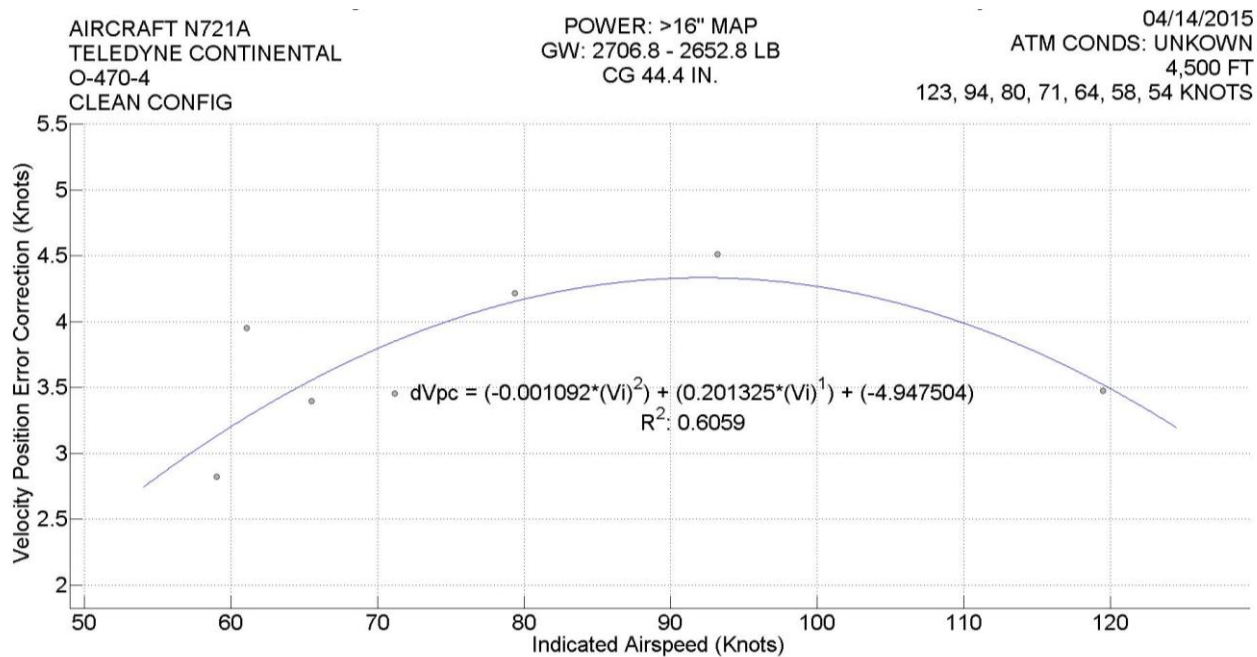


Figure B-24. Velocity static pressure position error (ΔVPC) vs indicated airspeed.

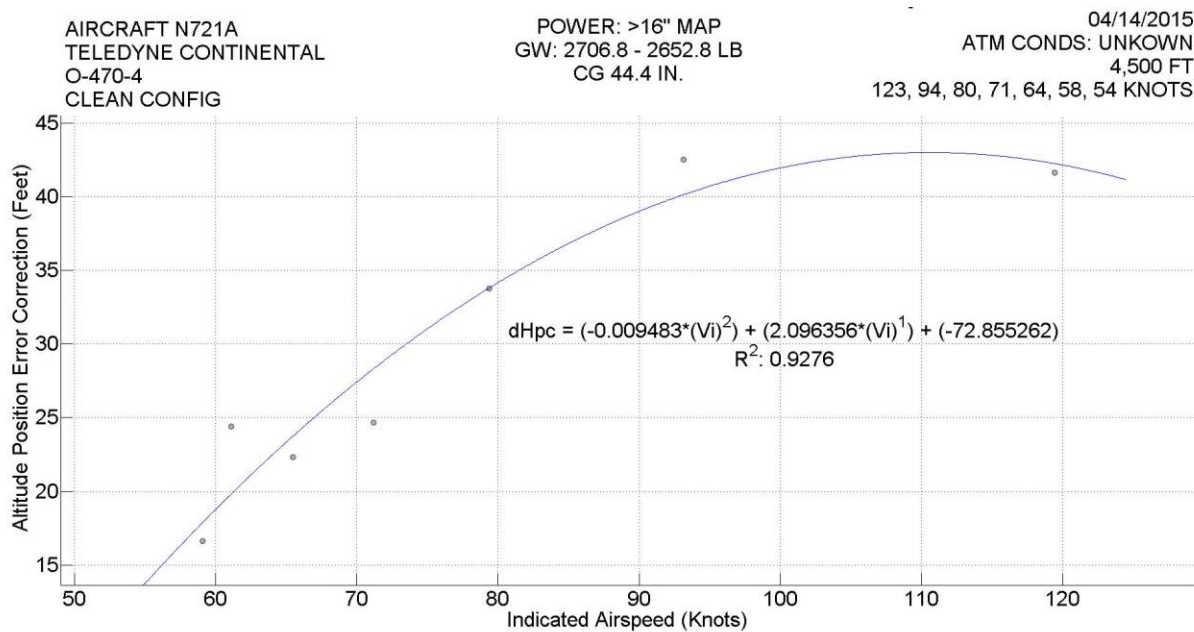


Figure B-25. Altitude static position error vs indicated airspeed.

As the indicated airspeed increases, the error correction remains relatively constant. This shows that the static port is well placed because the static pressure doesn't change as the flow field changes. The data point at 61 KIAS is a slight outlier to the trend, caused by failing to maintain test tolerances, a changing air mass composition, or turbulence.

The graph in Figure B-24 shows how the velocity position error correction changes with indicated airspeed. The best fit line between ΔV_{PC} and indicated airspeed is parabolic. Once again, the 61 KIAS value is an outlier.

Figure B-25 shows a parabolic relationship between altitude position error correction and airspeed. At low speeds there is a small correction, however, as indicated airspeed increases, a larger correction must be applied.

Upwash Calibration

The following figures were obtained for the upwash calibration. Figure B-25 is a sample figure for $\Delta\alpha$ vs. time, α vs. time, airspeed vs. time, and altitude vs. time for the first leg of the flight test. Figure B-26 shows the $\Delta\alpha$ vs. time for all legs of the flight test and Figure B-28 shows α_T vs. α_i for all legs of flight test. Two correction factors were included, 0.4° for α_i and 7.08° for α_T . The correction factor for α_i was due to the air data boom being mounted exactly 0.4° below the fuselage reference line (FRL). This correction factor was added to α_i . The correction factor for α_T was due to the inertial navigation system (INS) mounted at a -7.08° incline. With these correction factors, α_T and α_i are with respect to the FRL.

Two methods are used to calculate upwash. The first method's results can be seen in Figure B-25 and the second method can be seen in Figure B-26. The first method uses Equations B-10 through B-12. Figure B-26 shows the trends of the airspeed, altitude, angle of attack, and upwash vs. time for the trimmed record data. The y-axis for airspeed and altitude are set at the flight test tolerance bands for the trim shots performed. This figure uses the first method of calculating upwash. The second method was used in Figure B-27. This takes into account the flight path angle using Equations B-7 through B-9.

As shown in Figure B-26 altitude and airspeed were flown within tolerances. The angle of attack and upwash measured during trim shots stay relatively constant.

Figure B-28 shows the upwash correction vs. measured angle of attack for all 28 trim shots. This upwash was calculated using Equations B-10 through B-12. This is the first method of calculating upwash. The measured angle of attack increases as the upwash correction increases. The data is scattered along the line, reflected in the R^2 value.

AIRSPEED: 123 KIAS
MANEUVER COUNTER: 39
HEADING: NORTH

RECORD 1

04/14/2015
AIRCRAFT: N721A

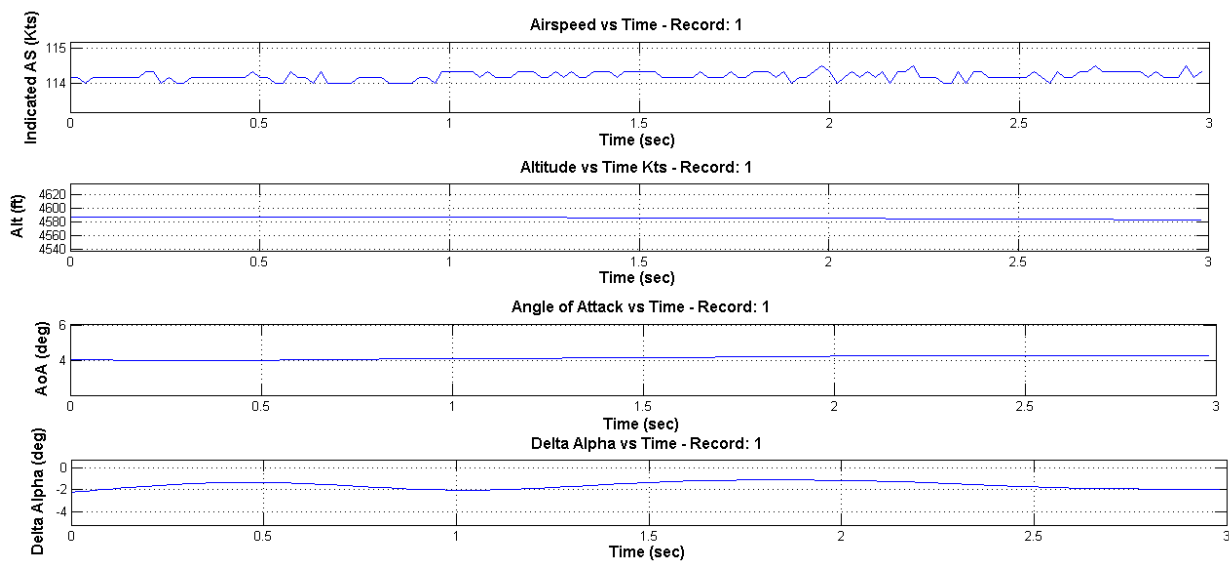


Figure B-26. $\Delta\alpha$ vs. time, α vs time, airspeed vs time, and altitude vs time for record 1.

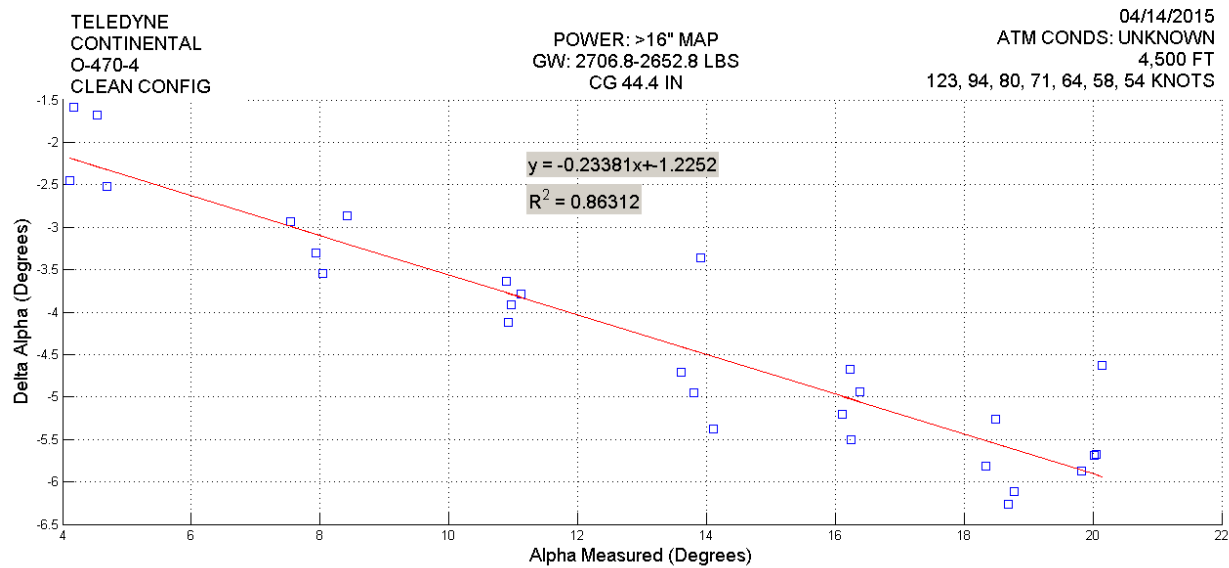


Figure B-27. $\Delta\alpha$ vs α_i for all legs. Alpha measured w.r.t. the fuselage reference line.

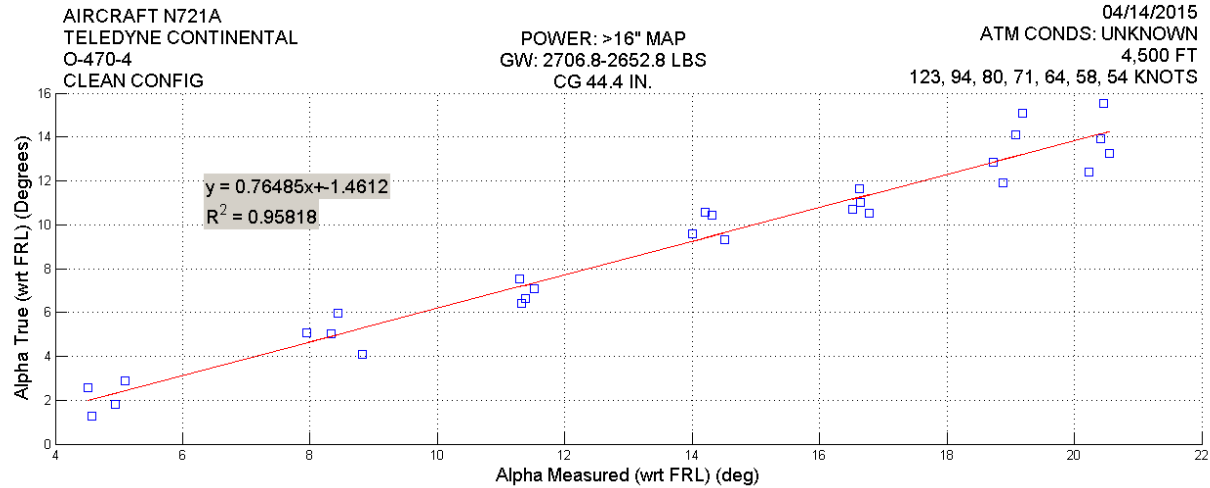


Figure B-28. α_{true} vs α_i for all legs.

Figure B-28 shows that as α_i increases, α_T increases as well. Thus, it can also be said that as α_i increases, upwash also increases.

The upwash results can be validated by comparing both Figures B-27 and B-28. As shown in Equation B-7, a direct way to find the upwash is by calculating the difference between α_T and α_i . The second method to calculate upwash was used to generate Figure B-28. In Figure B-28 at an α_i of 10° α_T is 6° . Thus, the upwash for method one is approximately 4° . As shown in Figure B-27 at an α_i of 10° the upwash can be seen to be approximately 3.5° . This validates the results presented in Figures B-27 and B-28 and shows a difference of 13.3%.

STALL TESTING

Data for the analysis of lift behavior at stall was collected during two stall maneuvers performed on 22 April 2015. Figure B-29 shows the aerodynamic model for the first stall. The maximum coefficient of lift was found to be 1.42 and occurred at an angle of attack of 16.5 degrees. Figure B-29 shows the lift coefficient versus angle attack for the second stall. The maximum coefficient of lift was shown as 1.38 at an angle of attack of 16 degrees.

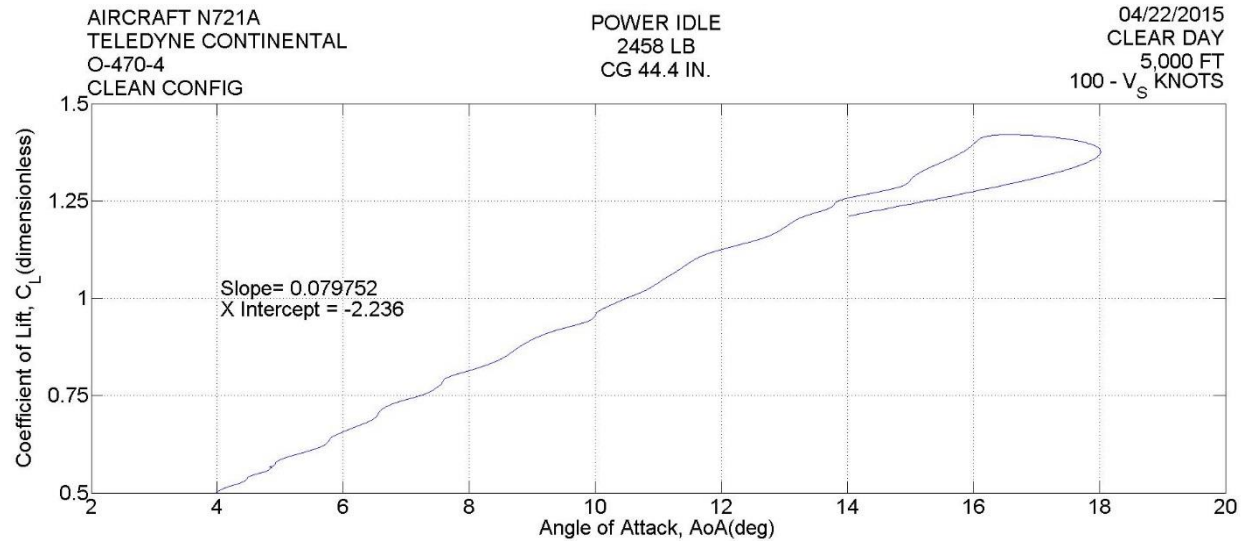


Figure B-29. Stall 1 lift coefficient vs angle of attack.



Figure B-30. Stall 2 lift coefficient vs angle of attack.

Figure B-31 overlays Figures B-29 and B-30 to compare Stall 1 and Stall 2. The data shows a consistent lift curve slope between both stalls. The difference of the maximum coefficient of lift between both two stalls is 3.15%. For the stall angle of attack, the difference is 3.08%.

Figures B-32 and B-33 show the calibrated airspeeds of the Cessna 182Q during the stalls. The average bleed rate observed for Stall 1 is 0.80 knots per second and for Stall 2 is 0.68 knots per second, a 15.97% difference. The differences in bleed rate will cause variations in the lift coefficient and change observed aerodynamic behavior. These effects can cause the maximum coefficient of lift and the stall angle of attack to increase with increased bleed rate. This could explain why Stall 1 has a larger max coefficient of lift and stall angle of attack than Stall 2.

The weight difference between the two stalls is 5.4 lb, a difference of 0.19%, resulting in a negligible change in maximum lift coefficient.

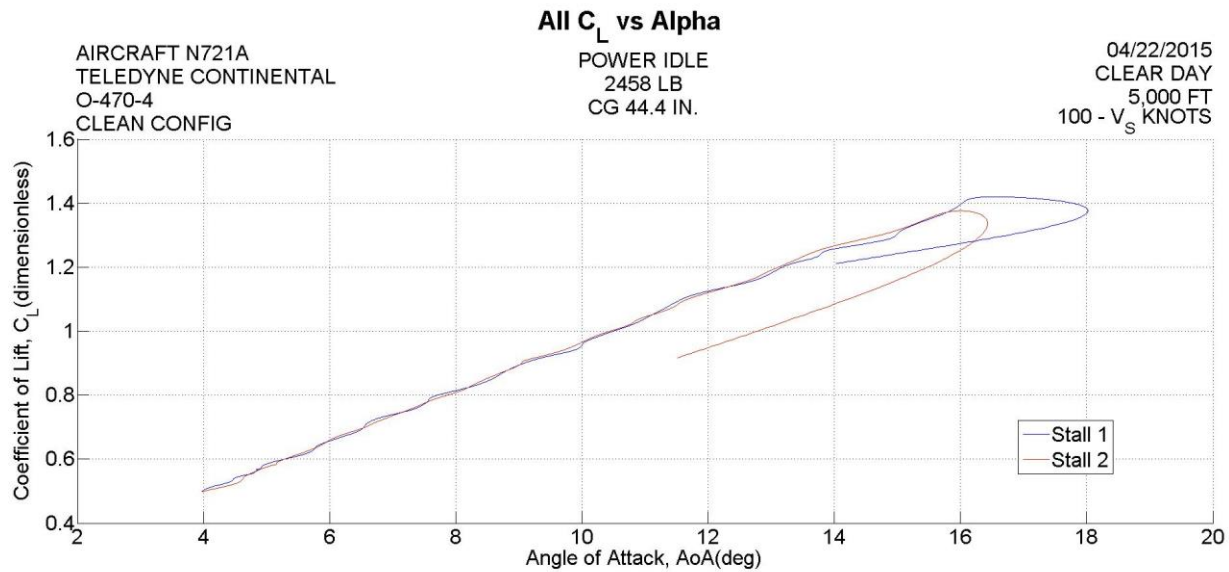


Figure B-31. Comparison between Stalls 1 and 2.

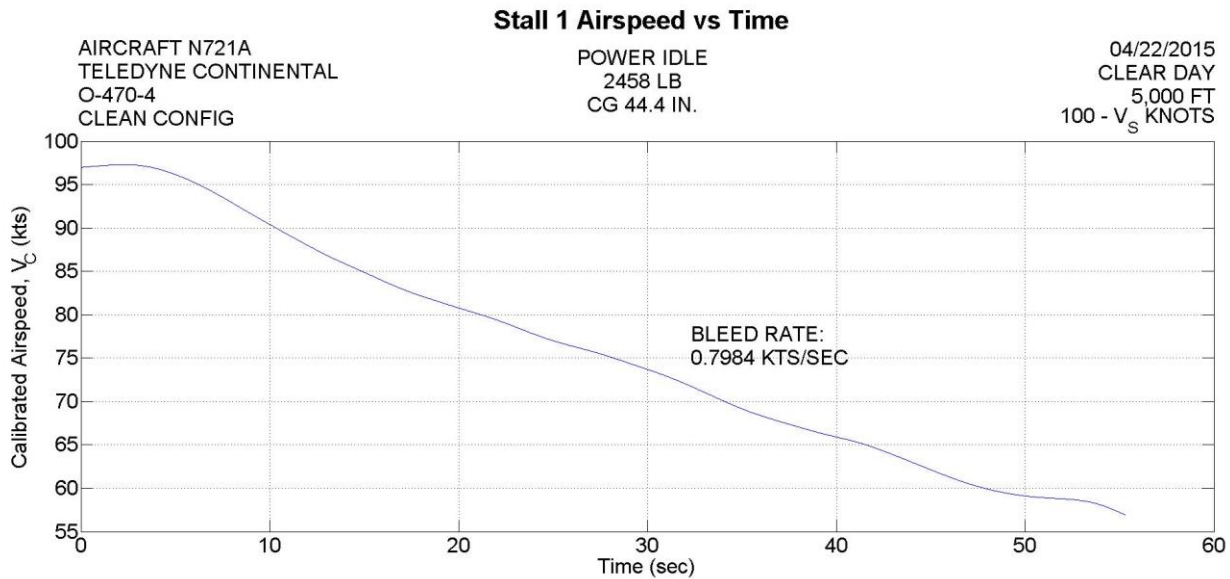


Figure B-32. Calibrated airspeed during Stall 1

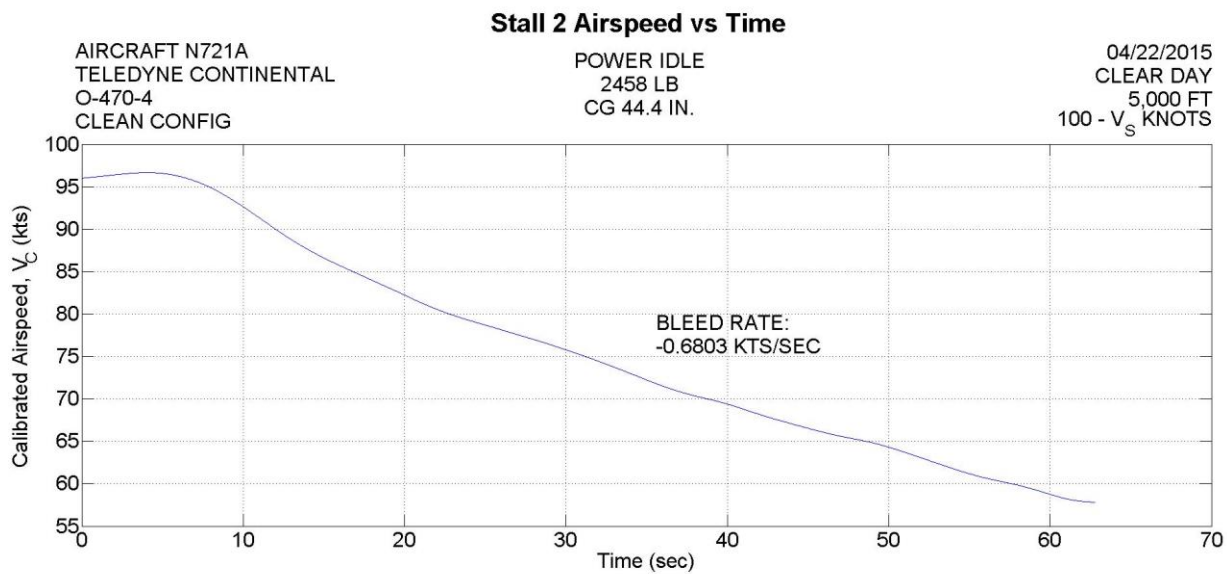


Figure B-32. Calibrated airspeed during Stall 2.

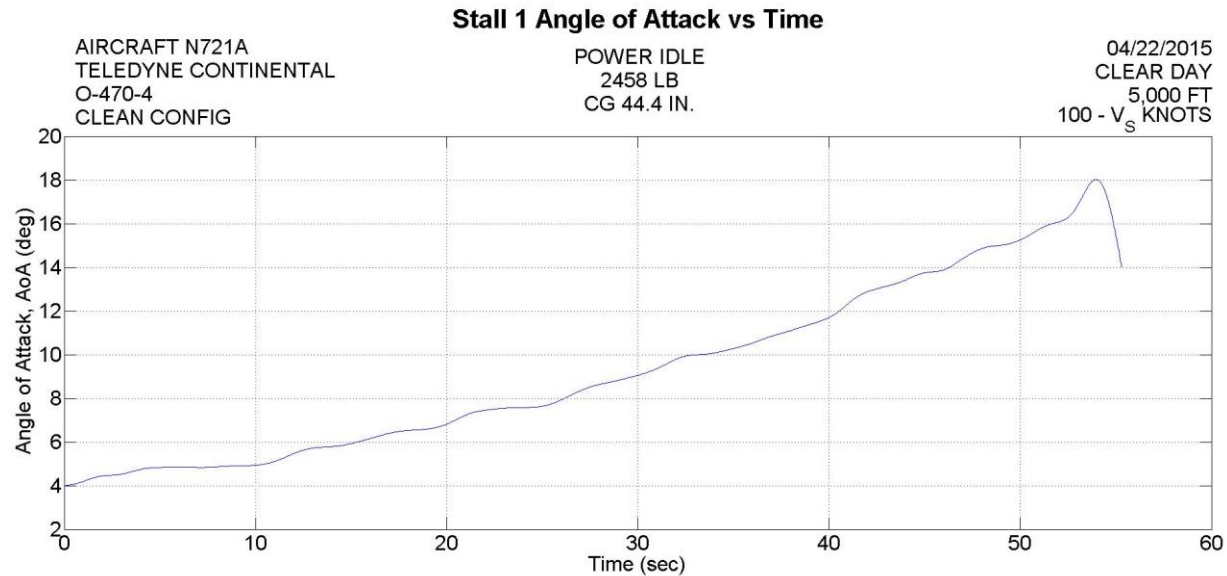


Figure B-33. Calibrated angle of attack during Stall 1.

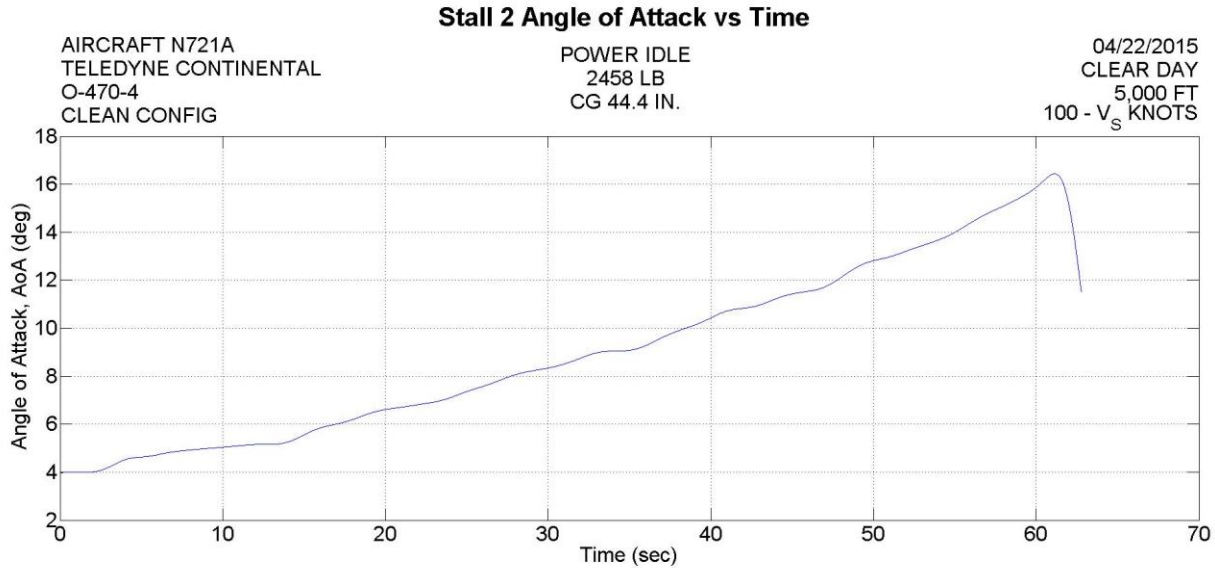


Figure B-34. Calibrated angle of attack during Stall 2.

The theoretical value for the lift curve slope of the Cessna 182Q was estimated at 0.08 per degree. Comparing this theoretical value to each individual stall, Stall 1 showed a difference of 0.057% and 0.41% difference for Stall 2. The average of the data was 0.0800 per degree, which has zero difference. Significant figures failed to capture the exact difference. The NACA 2412 airfoil in this aircraft has a maximum coefficient of lift of 1.5 to 1.7 at a geometric angle of attack of about 16 degrees depending on aerodynamic center location and atmospheric conditions. With the assumption that 90% of the airfoil max lift coefficient can estimate the theoretical max lift coefficient the aircraft, the Cessna 182Q should have a theoretical value of 1.44 for the max lift coefficient. The average max coefficient of lift value was 1.40, a 2.86% difference from the theoretical value. The average geometric stall angle of attack was 16.25 degrees, differing by 1.55% from the airfoil's theoretical value.

The calibration methods showed a parabolic relationship for dV_{pc} and dH_{pc} while the PEC remained fairly constant. The dV_{pc} correction factor peaks at 94 KIAS at an approximate value of 4.5 knots. Compared to the POH data, the velocity pressure position corrections at each indicated airspeed show a largest error of 7.7%. The dH_{pc} correction factor peaks at approximately 110 KIAS with an approximate value of 43 feet. Furthermore, the results of the upwash calibration determined that as the angle of attack increases, the upwash correction also increased. A validation of these results was done by using two different methods to reach the same conclusion, showing a 13.3% difference in $\Delta\alpha$ at an α of 10 degrees. The last flight test technique showed that the maximum lift coefficient and stall angle of attack had errors of 5.71% and 12.1% respectively.

APPENDIX C. AERODYNAMICS OF WHY A LINEAR CALIBRATION WORKS

Six frame grabs from a 1938 NACA film [NACA38] are shown in Figure C-1 (two of these frame grabs, (a) and (f), are also shown in Figure 30). These images illustrate the underlying principle that results in a linear calibration curve for under wing mounted differential angle of attack probes. The airfoil in the frame grabs is a symmetrical airfoil.

The pressure on the surface of the airfoil referenced to the free stream (atmospheric) pressure is positive in the vicinity of the stagnation point but generally negative on the upper surface and may be negative or positive on the lower surface (see Figure C-2 or 31). Generally, other than near the stagnation point, if the pressure relative to the atmosphere pressure is positive on the lower surface it is positive at low angles of attack near the trailing edge or when flaps are deployed.

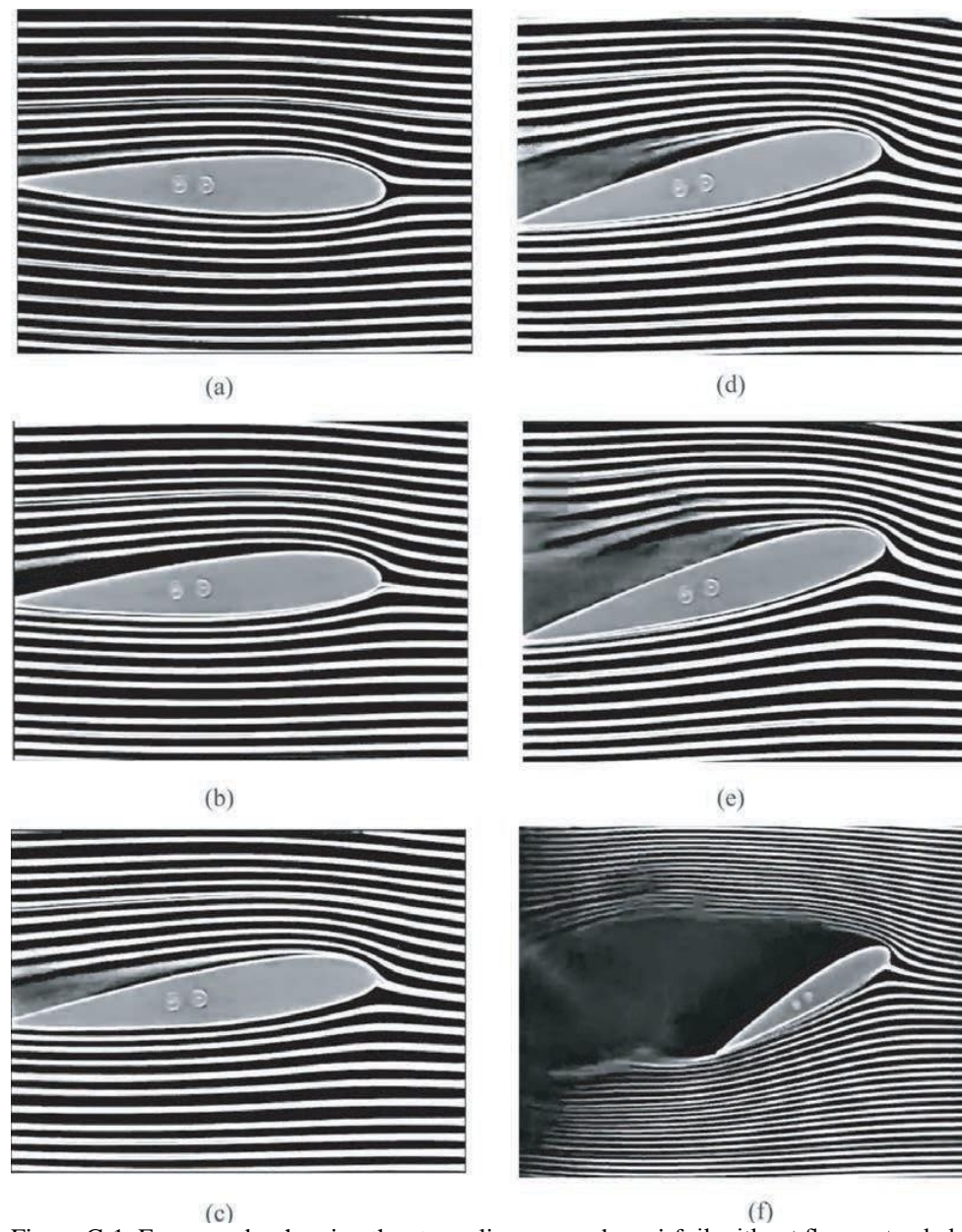


Figure C-1. Frame grabs showing the streamlines around an airfoil without flaps extended.

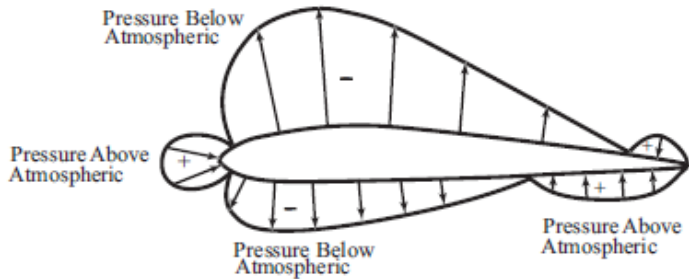


Figure C-2. Sketch of the pressure distribution on the surface of a typical airfoil.

Returning to Figure C-1, notice that the pressure is typically below atmospheric pressure except near the leading and trailing edges. Hence, the pressure is increasing away from the airfoil surface. Because P_{fwd} has a significant dynamic pressure component for typical angles of attack, P_{fwd} is larger than P_{45} . Hence, provided that the angle of attack probe is mounted behind the forward stagnation positive pressure region and ahead of the trailing edge positive pressure region the P_{fwd}/P_{45} pressure ratio smoothly varies as the angle of attack changes. The data from the current flight tests suggests that the variation is linear.

Looking carefully at Figures C-1a to f notice, that Figure C-1a is at zero angle of attack and that the angle of attack increases in each of the successive figures (b–f). Also notice that the 11th and 12th streamlines from the bottom of Figure C-1a pass above and below the airfoil respectively.

There is a streamline between the 11th and 12th streamlines (not shown) that impacts exactly on the nose of the airfoil. That streamline is called the stagnation streamline and the point where it impacts the airfoil is called the stagnation point. At the stagnation point all the energy of motion in the airflow is converted to pressure—the stagnation pressure. The stagnation pressure is larger (positive) with respect to the static (atmospheric) pressure in the free stream.

Now notice that the 11th streamline from the bottom in Figure C-1a passes just below the airfoil as does the 11th streamline in Figure C-1b. However, in Figure C-1c the 11th streamline passes just above the airfoil as do the 11th streamline in Figures C-1d and C-1e. What this means is that as the angle of attack increases the stagnation point and the stagnation streamline move below the nose of the airfoil. This is also true in Figure C-1f, but more streamlines are shown so it is no longer between the 11th and 12th streamlines but the 22nd line from the bottom appears to be the stagnation streamline itself.

The pressure on the surface of the airfoil referenced to the free stream (atmospheric) pressure is positive in the vicinity of the stagnation point but generally negative on the upper surface and may be negative or positive on the lower surface (see Figure C-2). Generally, other than near the stagnation point, if the pressure relative to the atmosphere pressure is positive on the lower surface it is positive at low angles of attack near the trailing edge or when flaps are deployed.

Returning now to Figure C-1, notice that the flow over the upper surface of the airfoil becomes more and more separated as the angle of attack increases, until it is fully separated (stalled) in Figure C-1f. However, looking at the bottom surface of the airfoil, notice that the flow along the surface is smooth and unseparated at any angle of attack shown. Thus, a bottom mounted angle of

attack probe is operating in a smoothly varying pressure field. The pressure far away from the airfoil surface must return to freestream (atmospheric) pressure.

Figure C-3 shows several frame grabs from the video [NACA38] for the same airfoil with a flap deployed. Again, the streamlines on the lower surface are smooth and remain smooth with increasing angle of attack. Hence, the pressure field on the bottom of the airfoil is also smooth. Thus, the angle of attack probe behaves in a similar manner as without a flap deployed.

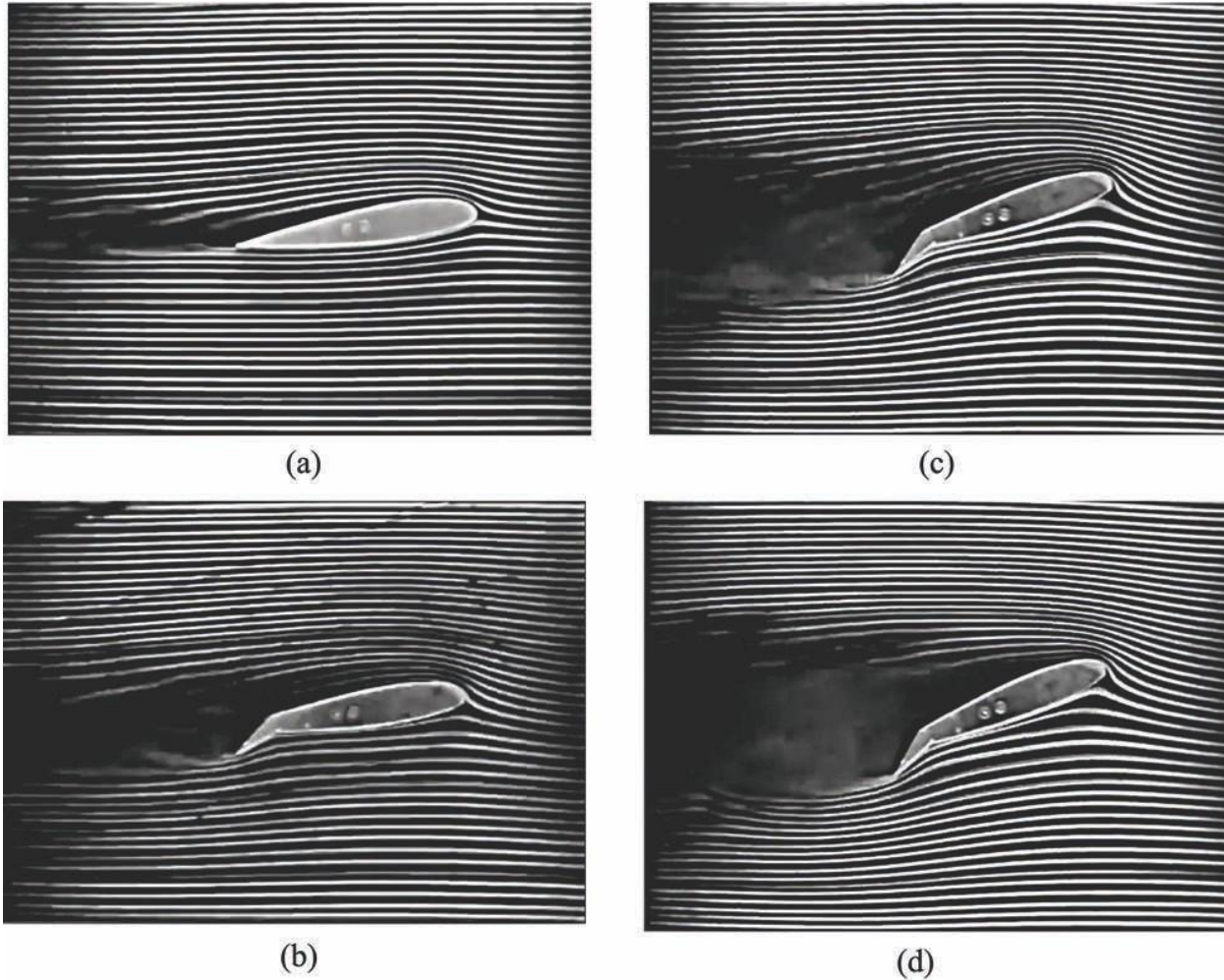


Figure C-3. Frame grabs showing the streamlines around an airfoil with flaps extended.

APPENDIX D. THE EFFECT OF THE AVERAGE OF AN AVERAGE

The difference in angle of attack for a given value of P_{fwd}/P_{45} is likely a result of the method used to determine both the angle of attack and P_{fwd}/P_{45} . Specifically, the noload value used in the 22 April 2015 flight test was determined by averaging 100 data points and was not changed, nor should it have been, for the two flight tests on 26/27 May and 18/19 August 2015. The 100 values for P_{fwd}/P_{45} for each leg of the 4-leg GPS horseshoe heading box pattern were averaged and then the four averaged values averaged again. The four true airspeeds determined from each of the triads of the 4-leg GPS horseshoe heading data were averaged to obtain the true airspeed for each data point. In short, the values represented by the data points are an average of an average. Finally, the calibration curve was determined by a ‘statistical’ fit to the averaged data.

To illustrate the effect of averaging the averages, consider Fig. D-1 which shows the data from the DFRDAS-2 for a single leg of the 4-leg GPS run at an indicated speed for $V_{L/D_{max}}$ at a pressure altitude of 6000 ft. The red data symbols and the red axis show the variation in P_{fwd}/P_{45} , and the solid red line shows the average of the 100 data points at 1.868. The standard deviation is 0.028, while the maximum deviation is 0.075 at a time of approximately 7.53 minutes. Recall that the angle of attack is derived from P_{fwd}/P_{45} .

The blue data symbols show the variation in angle of attack, while the solid blue line shows the average of the 100 data points as 10.43° . The standard deviation is 0.49° . However, the maximum deviation for this data set is 1.33° , again at a time of approximately 7.53 minutes as expected.

In addition to the effect of the average of an average there is ‘ringing’ of the transducer in the pressure sensor which accounts for 1/4 % of full scale, i.e., 1/4 % of 1.0 psi or 0.0025 psi.

Finally, the constant small stick inputs by the pilot in maintaining constant heading, altitude and airspeed without changing power available or trim contribute.

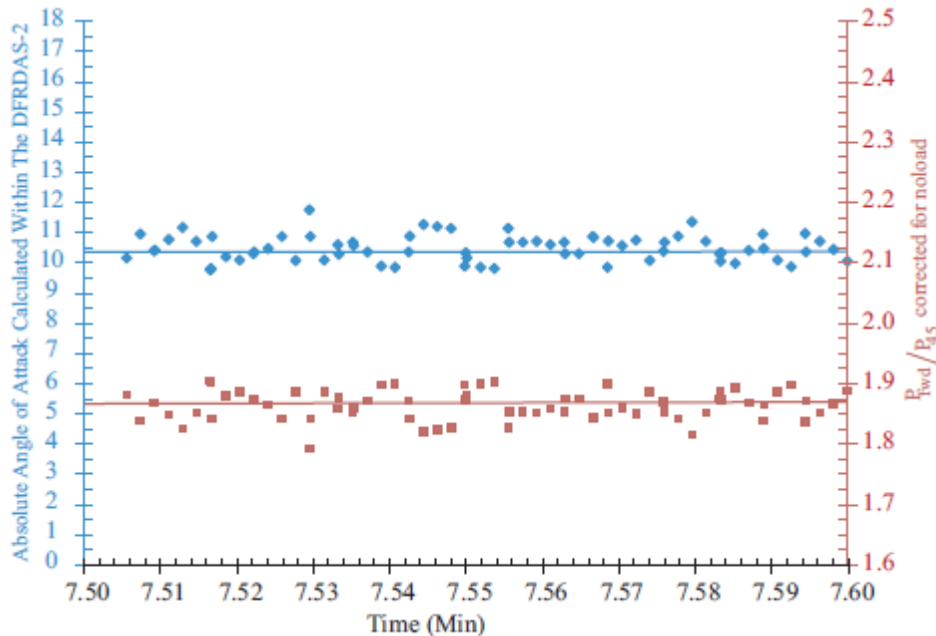


Figure D-1. Values for angle of attack and P_{fwd}/P_{45} from DFRDAS-2 for one leg of the 4-leg GPS data point for $V_{L/D_{max}}$ for the 26 May 2015 flight test.

APPENDIX E. THE RESPONSE OF THE DFRDAS TO VARIOUS STALL CONFIGURATIONS

Below is a series of graphs of the response of the DFRDAS to various stall configurations. The available configurations are detailed in Table E-1. The flap angle was measured between the upper wing surface of the right wing just ahead of the flap and at the flap trailing edge approximately five inches outboard of the fuselage. A digital inclinometer was used.

Unless otherwise stated all stalls were performed as standard FAA stall, i.e., using a deceleration of one KIAS per second. Accelerated stalls were performed using a deceleration of five KIAS per second. All banks are to the right.

Table E-1. Stall Series.

Figure No.	Flaps (deg)	Bank Angle	Accelerated
E-1	0	0	No
E-2	0	20	No
E-3	0	30	No
E-4	0	0	Yes
E-5	0	0	Yes
E-6	21.5	0	No
E-7	21.5	20	No
E-8	21.5	30	No
E-9	21.5	0	Yes
E-10	30	0	No
E-11	30	20	No
E-12	30	30	No
E-13	30	0	Yes
E-14	40	0	LCO*

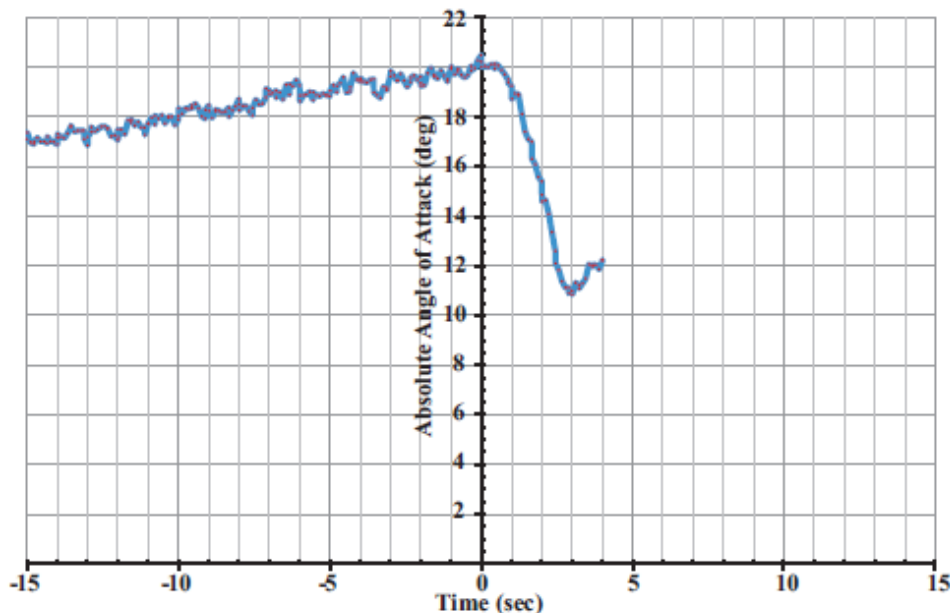


Figure E-1. FAA standard stall with Flaps 0° and Bank 0° DFRDAS-2 probe on the right wing at 38.9% of the local ©2015 David F. Rogers. All rights reserved.

chord.

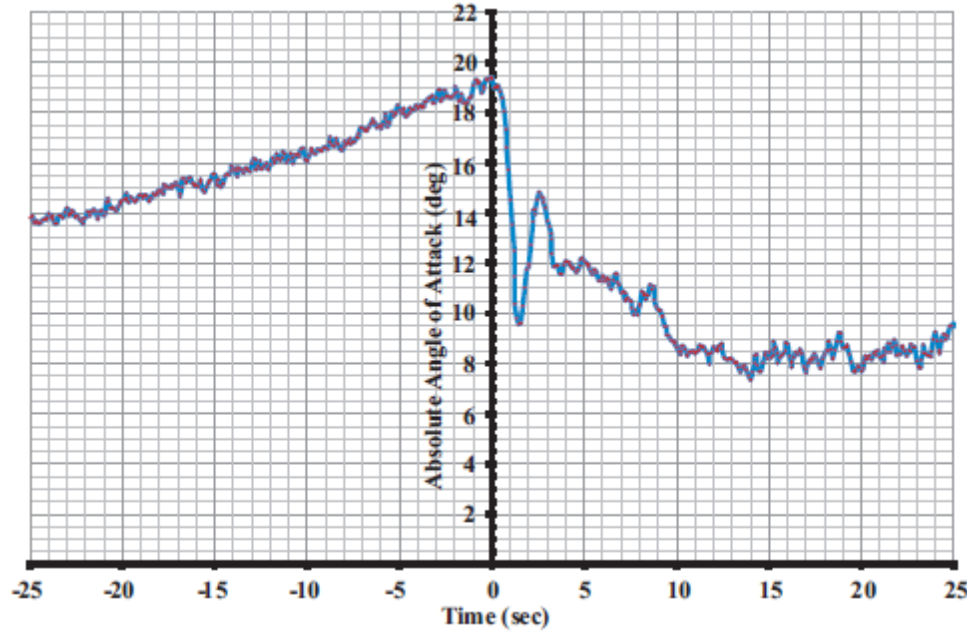


Figure E-2. FAA standard stall with Flaps 0° and Bank 20° DFRDAS-2probe on the right wing at 38.9% of the local chord.

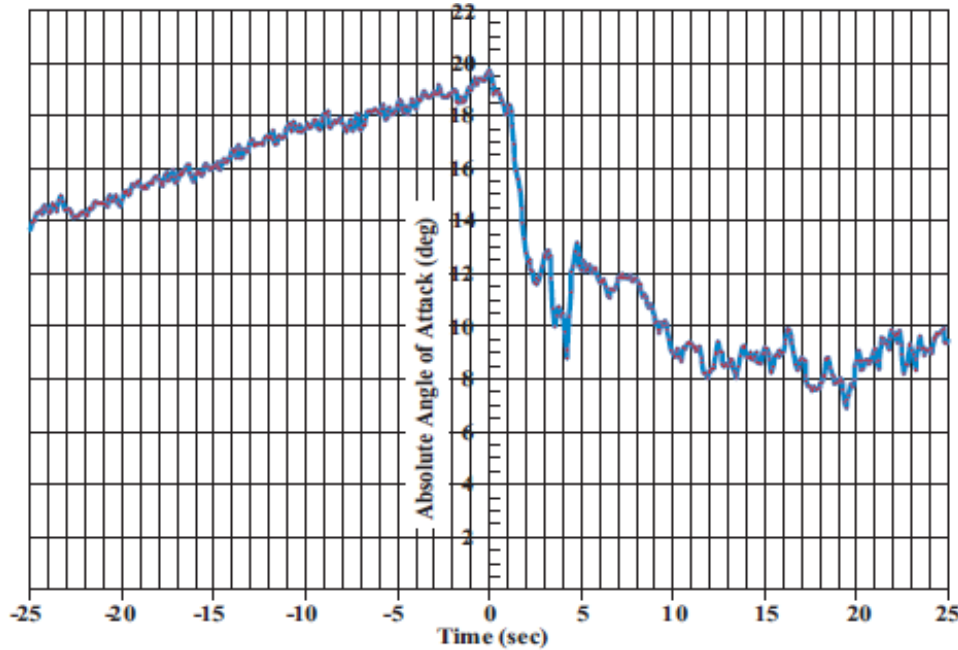


Figure E-3. FAA standard stall with Flaps 0° and Bank 30° DFRDAS-2probe on the right wing at 38.9% of the local chord.

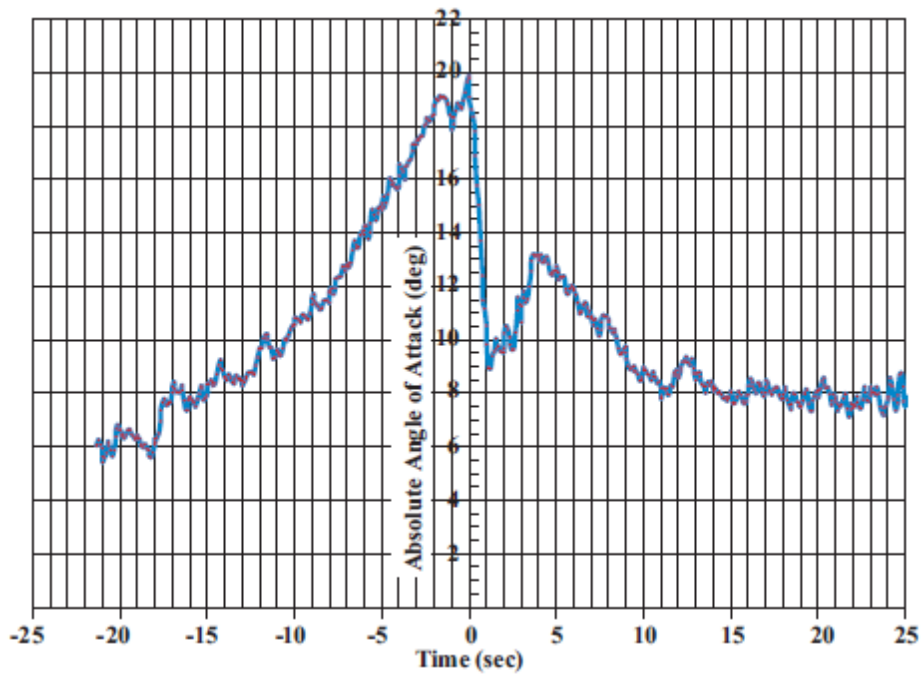


Figure E-4. FAA accelerated stall with Flaps 0° and Bank 0° DFRDAS-2probe on the right wing at 38.9% of the local chord.

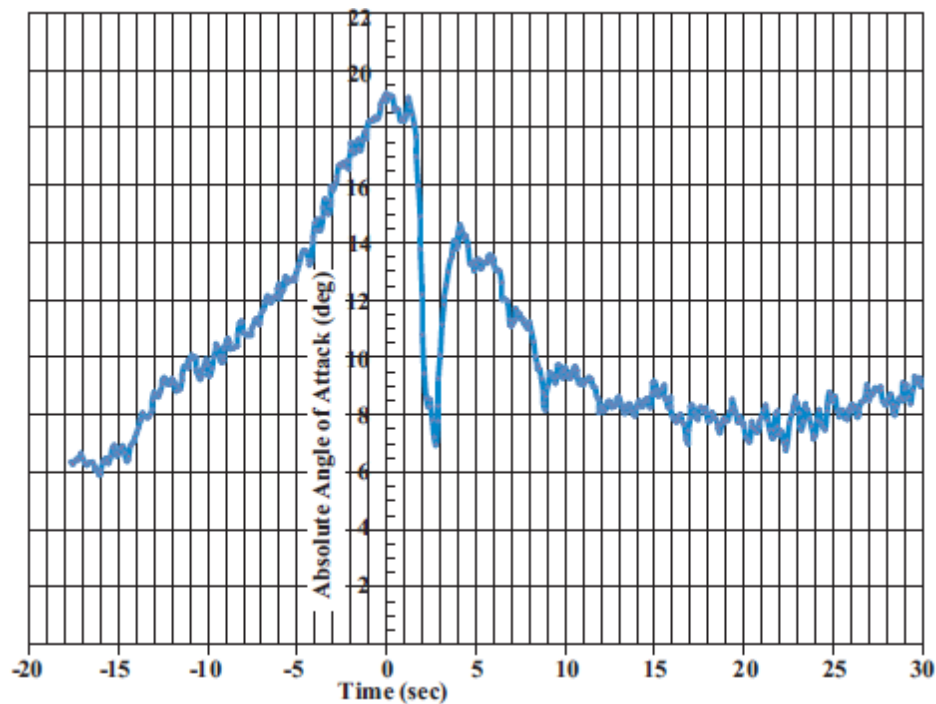


Figure E-5. FAA accelerated stall with Flaps 0° and Bank 0° DFRDAS-2probe on the right wing at 38.9% of the local chord.

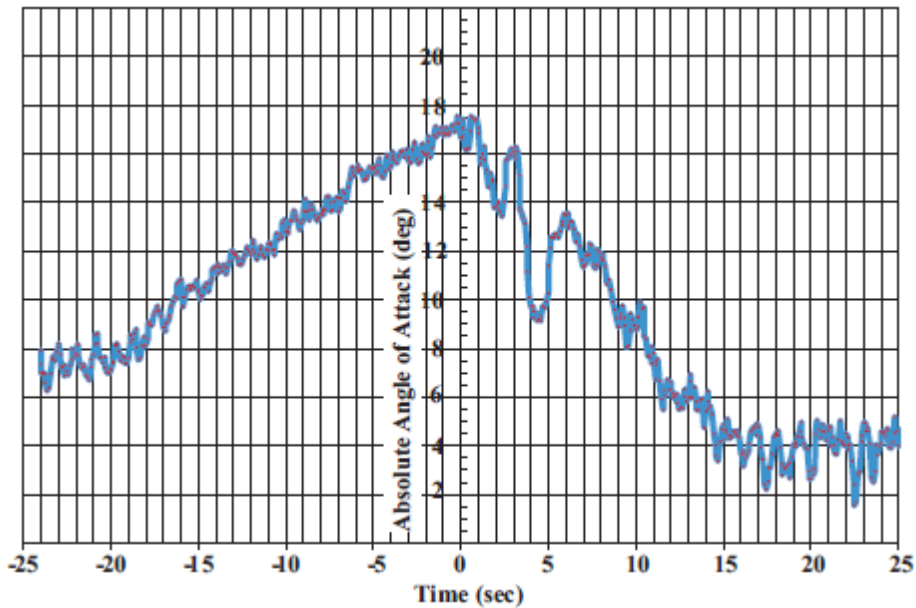


Figure E-6. FAA accelerated stall with Flaps 21.5° and Bank 0° DFRDAS-2 probe on the right wing at 38.9% of the local chord.

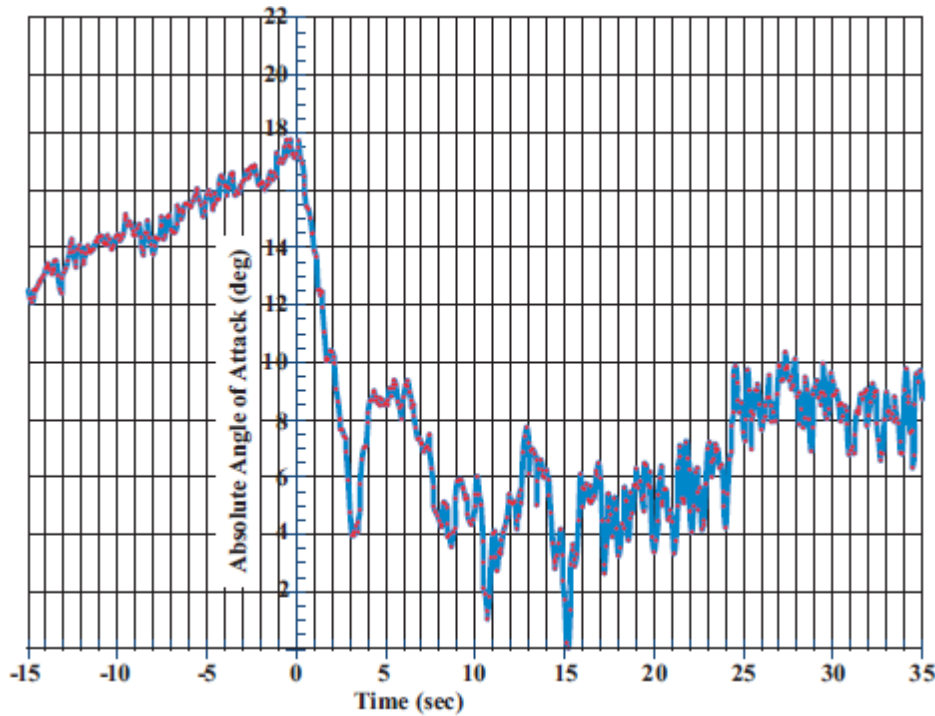


Figure E-7. FAA standard stall with Flaps 21.5° and Bank 20° DFRDAS-2 probe on the right wing at 38.9% of the local chord.

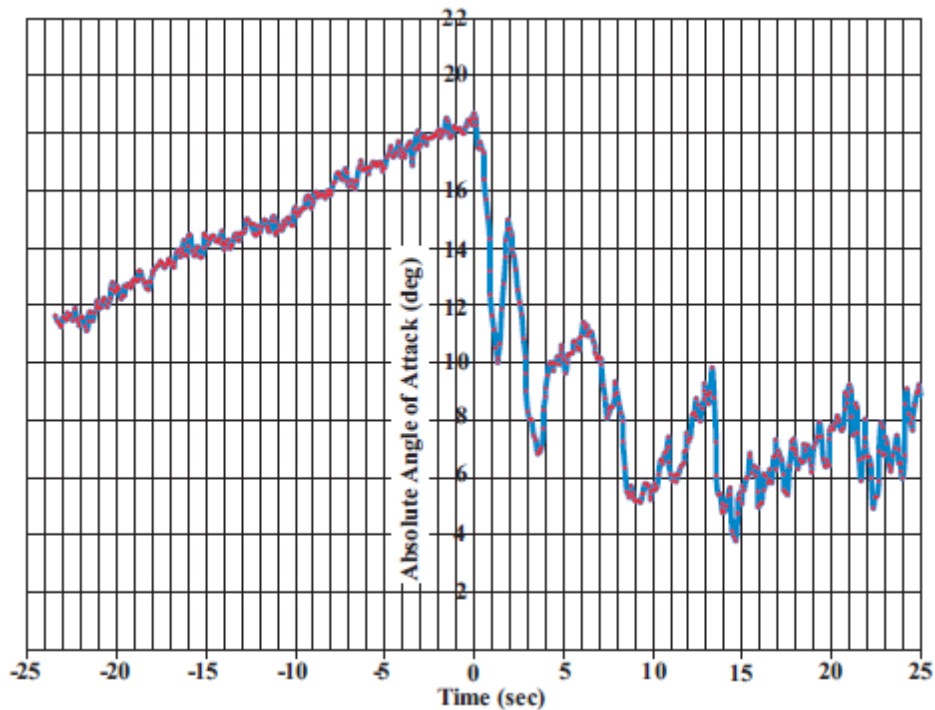


Figure E-8. FAA standard stall with Flaps 21.5° and Bank 30° DFRDAS-2 probe on the right wing at 38.9% of the local chord.

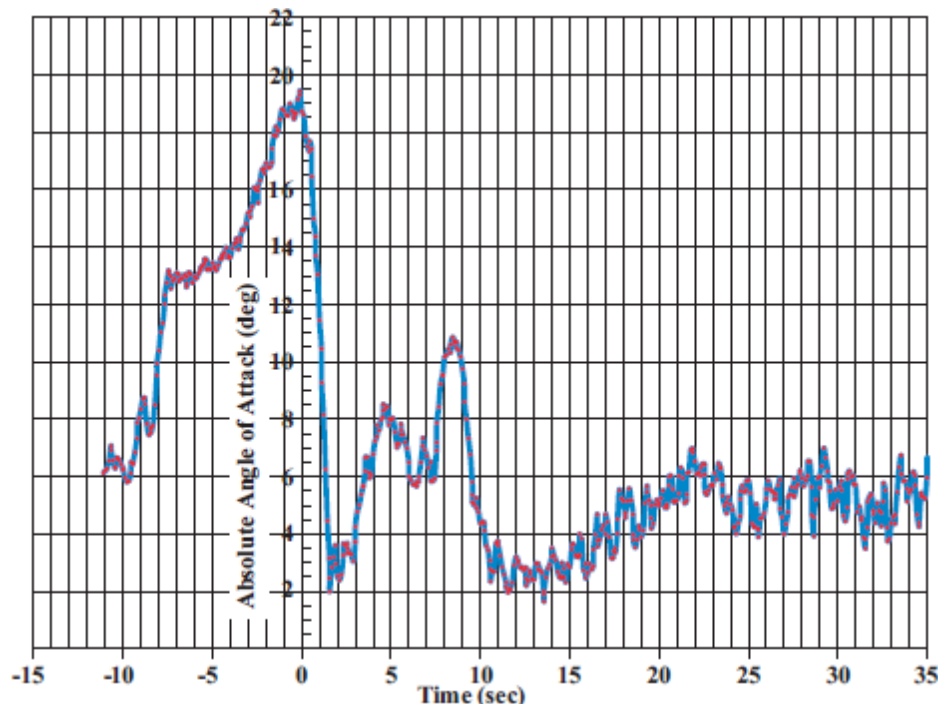


Figure E-8. FAA accelerated stall with Flaps 21.5° and Bank 0° DFRDAS-2 probe on the right wing at 38.9% of the local chord.

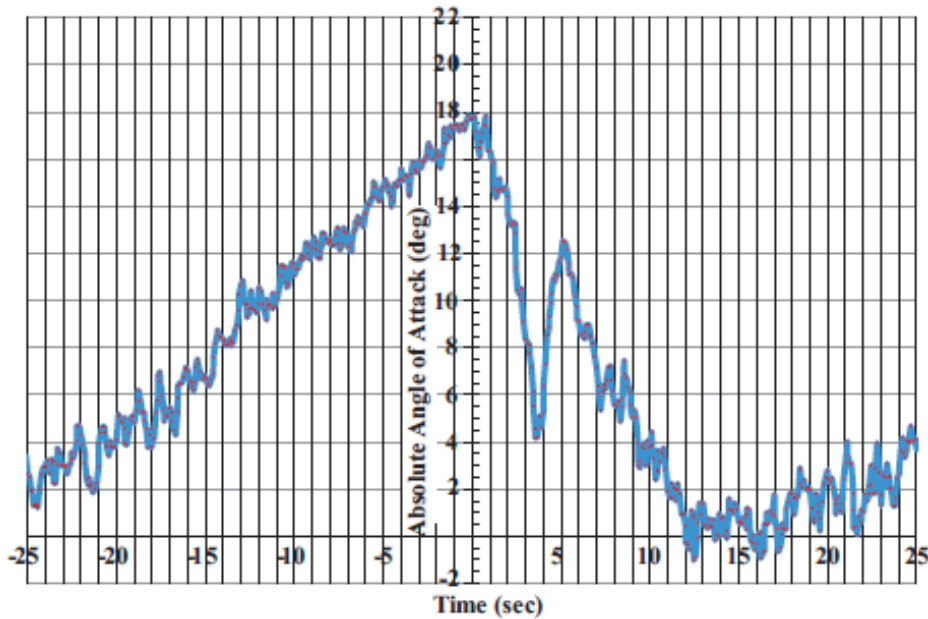


Figure E-9. FAA standard stall with Flaps 30° and Bank 0° DFRDAS-2 probe on the right wing at 38.9% of the local chord.

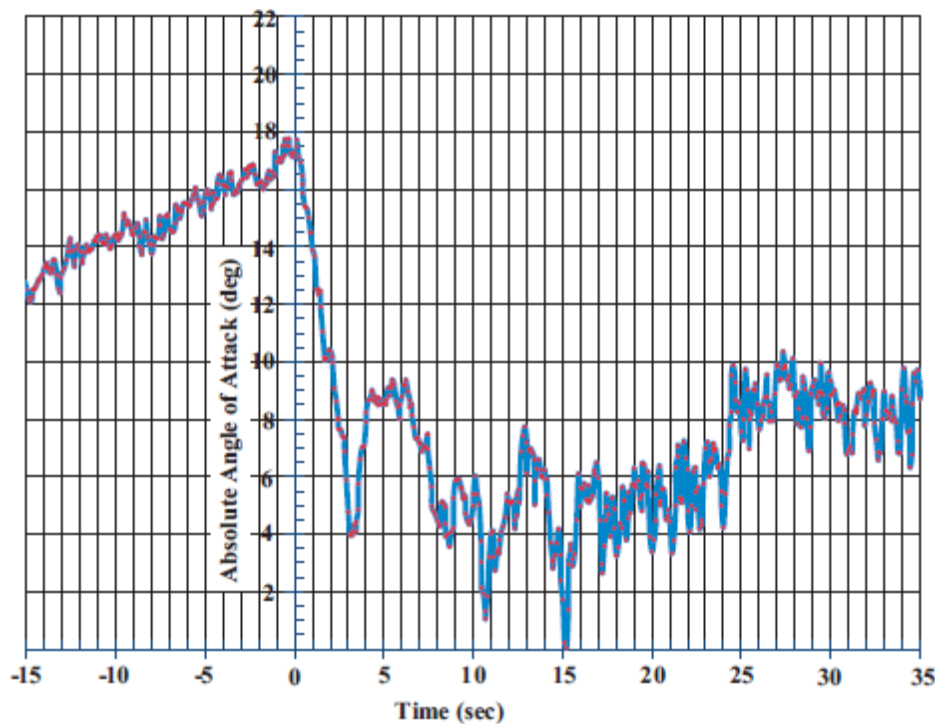


Figure E-10. FAA standard stall with Flaps 30° and Bank 20° DFRDAS-2 probe on the right wing at 38.9% of the local chord.

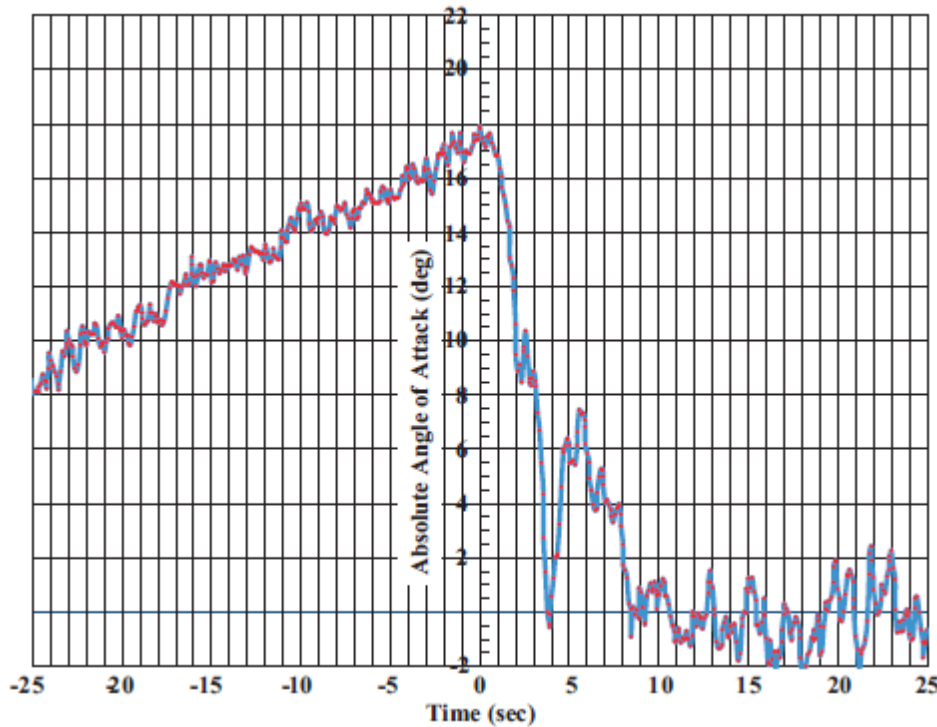


Figure E-11. FAA standard stall with Flaps 30° and Bank 30° DFRDAS-2 probe on the right wing at 38.9% of the local chord.

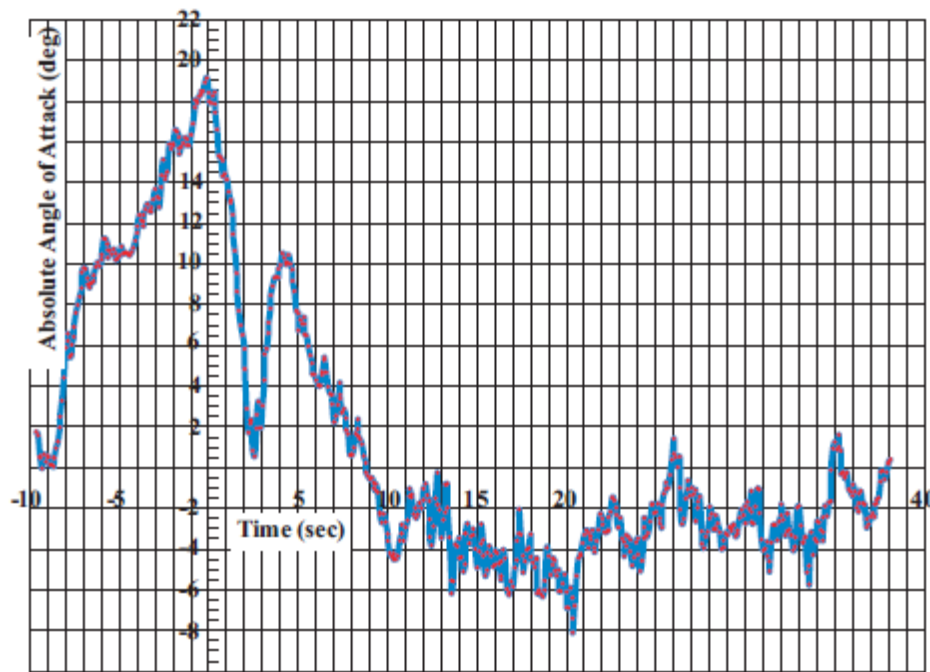


Figure E-12. FAA accelerated stall with Flaps 30° and Bank 0° DFRDAS-2 probe on the right wing at 38.9% of the local chord.

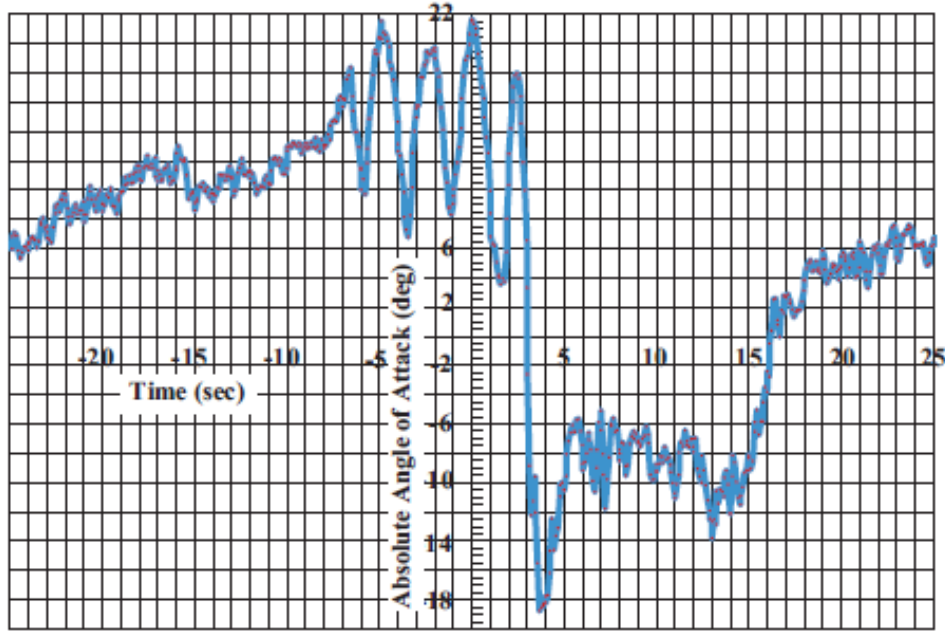


Figure E-13. FAA standard stall with Flaps 30° and Bank 30° DFRDAS-2 probe on the right wing at 38.9% of the local chord. This is a four cycle limit cycle oscillation.

APPENDIX F. HAZARDS, TEST CARDS AND FLIGHT LOG

EFRC SAFETY FINDING		
SAFETY FINDING TITLE FUNCTIONAL CHECK FLIGHT		
PROJECT FAA-AOA-GRANT	AIRCRAFT (N NUMBER) Cessna 182Q (N721A)	DATE April 2015
CONCLUSION AND RECOMMENDATIONS		
<ol style="list-style-type: none"> 1. A Hazards Review was completed on 01 April 2015 for the Federal Aviation Administration (FAA) Angle Of Attack (AOA) grant flights. These flights include functional check flights in Daytona Beach, Florida (KDAB). All Hazard Reports, hazard mitigations, and safety related issues were identified, discussed, assessed, and assigned an appropriate Hazard Risk and Probability after all hazard mitigations were applied. 2. A total of 4 Hazards were identified for this mission. <ul style="list-style-type: none"> • HR-AOA-02 In flight collision with other aircraft I-E • HR-AOA-03 Injury or Emergency egress blockage due to loose equipment I-E • HR-AOA-04 Electrical fire and smoke I-E • HR-AOA-05 Air data boom structural failure I-E All four hazards were assigned a I-E 3. In addition to the FAR's the following flight limitations were identified for the flight(s). <ul style="list-style-type: none"> • All flights must be conducted in VMC (no flight through visible moisture). • No over-water flight below 1,000 FT AGL. • No flight operations / RTB if lightning is observed within 25 nm radius. 4. The following Mission Rules were identified for the flight(s). <p>For All Flight Operations:</p> <ul style="list-style-type: none"> • Minimum flight crew is two qualified pilots. • One pilot will maintain visual look-out for traffic at all times. • Attempt to remain in communication with airspace controlling agency at all times. • Attempt to remain in positive radar contact at all times. 		
<p>A structural functional check flight was completed on 31 March 2015 for the FAA Angle of Attach research mission. The following conclusions and recommendations are made:</p> <ol style="list-style-type: none"> 1. No handling or structural anomalies up to +2.5/-0.5g's and 157 KIAS. 2. When the air data boom is installed V_{NE} is 143 KIAS. All others speeds are as outlined in the POH. 3. Mitigations and controls for all hazards are adequate for safe flight. 4. Air data boom flights are approved. 		
NAME / SIGNATURE <i>Scott Martin</i>	DATE 4/1/15	

Figure F-1. EFRC safety finding.

EFRC FLIGHT PERMIT (FP)

FLIGHT PERMIT TITLE MISSION FLIGHTS

PROJECT FAA-AOA-GRANT	AIRCRAFT (N NUMBER) Cessna 182Q (N721A)	DATE April 2015
--------------------------	--	--------------------

FLIGHT ACTIVITY (*Specify type of flight operation.*)

- Flight Research Cessna 182Q (N721A) Flight Training / Proficiency
 Flight Support Other (Specify): _____

FLIGHT LIMITATIONS (*List aircraft and flight limitations due to experimental hardware, software, weather conditions, pilot qualification, allowable aircrew, etc.*)

Flight Limitations in addition to the FAR's:

1. All flights must be conducted in VMC (no flight through visible moisture).
2. No over-water flight below 1,000 ft AGL.
3. No flight operations / RTB if lightning is observed within 25 nmi radius.
4. All flight operations will be conducted within the normal operating limits of the aircraft with the following limitations: the maximum load factor is restricted to +2.0g and 0.0g and the maximum allowable airspeed is restricted to 143 KIAS (V_{NO}).

Mission Rules For All Flight Operations

1. Minimum flight crew is one qualified pilot.
2. Attempt to remain in communication with airspace controlling agency at all times.
3. Attempt to remain in positive radar contact at all times.

CONTACT INFORMATION (*List personnel responsible for engineering and operations.*)

Engineering: Agustín Giovagnoli / EFRC, (386) 506-2340

Aircraft Maintenance: Daniel Stinelli / EFRC, (239) 287-1622

Flight Operations: Pat Anderson / EFRC, (386) 323-8876

Instrumentation / Systems: Daniel Stinelli / EFRC, (239) 287-1622

Science / Principal Investigator: Borja Martos / EFRC, (386) 323-8870

SIGNATURE / DATE (Head of Flight Operations)



4/1/2015-

Figure F-2. EFRC flight permit.

AIRCREW TEST CARDS

AOA Calibration Flight

Scheduled Date : March 2015

Aircraft Type/ Tail# : C182Q, N721A

Mission Risk Level: LOW

Safety/Test Considerations

TEST OBJECTIVES

1. AOA avionics calibration flight.

SECURITY REQUIREMENTS

1. Mission/data classification
 - Briefing / Cards – N/A
 - Other classifications: N/A

GO / NO-GO

1. VMC required
2. Winds calm and little or no turbulence.

These flight test cards are a compilation of safety and operating procedure information extracted from various sources and developed by test personnel. Submit recommended changes to Test Conductor Borja Martos, EFRC (386) 323-8092

These test cards were prepared and certified by the following:

Prepared by:
Test Engineer


Agustin Giovagnoli

Prepared by:
Project Aircrew


Borja Martos

Reviewed by:
Technical Director


Pat Anderson

Certified by:
Certifying Review


Scott Martin

Test Hazard Analysis Worksheets (THAWs)

1. In-flight collision with other aircraft
2. Injury or Emergency egress blockage due to loose equipment.
3. Electrical fire and/or smoke.
4. Airdata boom and structural failure

SAFETY APPENDIX RESTRICTIONS: - NONE

ATRISB STIPULATIONS: None beyond THAW requirements

MANUVERING RESTRICTIONS - +2/0 G's / 143 KIAS

WEATHER REQUIREMENTS - Day VMC

PHOTO/SAFETY CHASE REQUIREMENTS - NONE

DIVERT - NONE

WAIVERS - NONE

ORM ATR/ISB = LOW

Figure F-3. Test cards and safety considerations cover.

Note – Only the test card cover sheet is included

HAZARD MATRIX AND SAFETY PROCESS

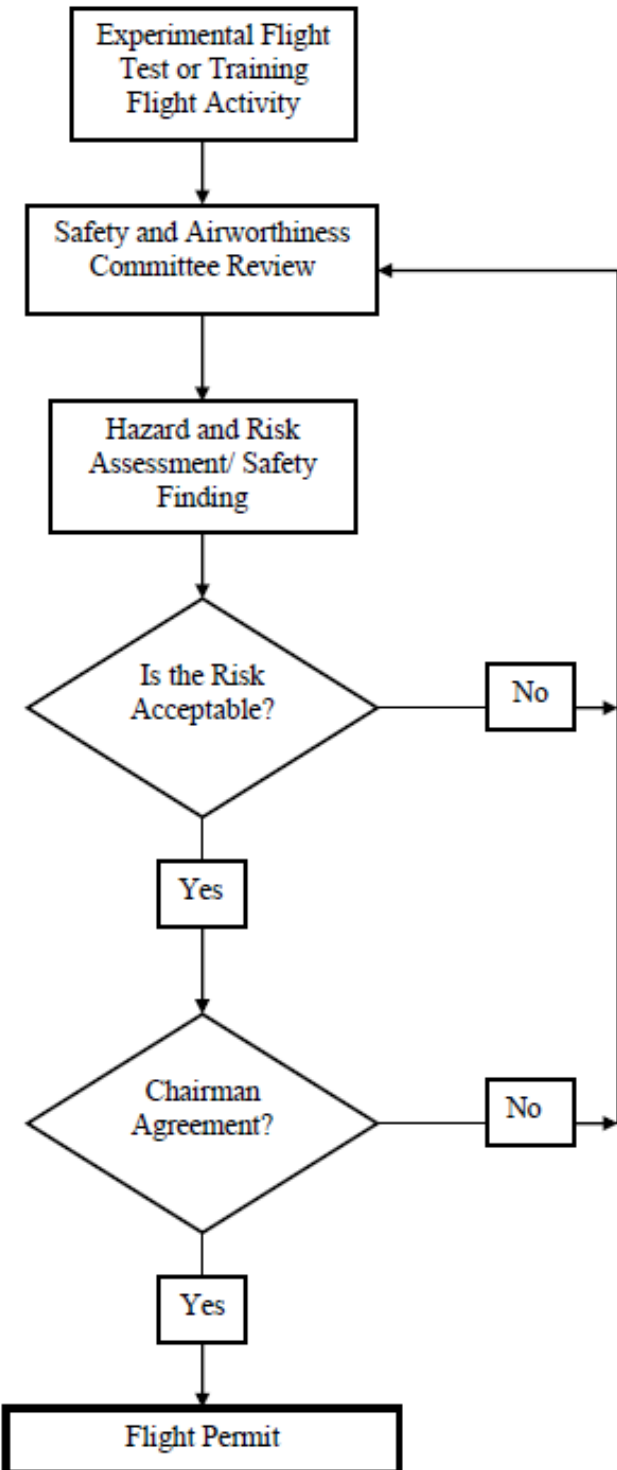


Figure F-4. Airworthiness and safety process.

Table F-1. Definitions of severity categories (Reference MILSTD-882D).

Description	Category	Environmental, Safety, and Health Result Criteria
Catastrophic	I	Could result in death, permanent total disability, or irreversible severe environmental damage that violates law or regulation.
Critical	II	Could result in permanent partial disability, injuries or occupational illness that may result in hospitalization of personnel, or reversible environmental damage causing a violation of law or regulation.
Marginal	III	Could result in injury or occupational illness resulting in one or more lost work days(s), or mitigable environmental damage without violation of law or regulation where restoration activities can be accomplished.
Negligible	IV	Could result in injury or illness not resulting in a lost work day, o minimal environmental damage not violating law or regulation.

Table F-2. Mishap probability levels (Reference MILSTD-882D).

Description*	Level	Quantitative Probability	Qualitative Probability
Frequent	A	Likely to occur often in the life of an item, with a probability of occurrence greater than 10^{-1} in that life.	Continuously experienced.
Probable	B	Will occur several times in the life of an item, with a probability of occurrence less than 10^{-1} but greater than 10^{-2} in that life.	Will occur frequently.
Occasional	C	Likely to occur some time in the life of an item, with a probability of occurrence less than 10^{-2} but greater than 10^{-3} in that life.	Will occur several times.
Remote	D	Unlikely but possible to occur in the life of an item, with a probability of occurrence less than 10^{-3} but greater than 10^{-6} in that life.	Unlikely, but can reasonably be expected to occur.
Improbable	E	So unlikely, it can be assumed occurrence may not be experienced, with a probability of occurrence less than 10^{-6} in that life.	Unlikely to occur, but possible.

Table F-3. Comparative risk assessment matrix (Reference MILSTD-882C).

FREQUENCY OF OCCURRENCE	HAZARD CATEGORIES			
	I CATASTROPHIC	II CRITICAL	III MARGINAL	IV NEGLIGIBLE
A - Frequent	IA	II A	III A	IV A
B - Probable	R1 IB	II B	III B	IV B
C - Occasional	IC	II C	III C	IV C
D - Remote	R 2 ID	II D	III D	IV D R 4
E - Improbable	R 3 IE	II E	III E	IV E

Hazard Risk Criteria:

- R1 – Unacceptable
- R2 – Must mitigate
- R3 – Acceptable with Chairman review
- R4 – Acceptable without review

FLIGHT LOG

Table F-4. Flight log.

Date	Flight	Pilot	Time [hr]
15-Jan-15	FCF - FUEL SCAN	Martos	1.4
16-Jan-15	FCF - GPS 4 LEG	Martos	2.7
16-Jan-15	FCF - AUTOPILOT	Martos	1.1
20-Jan-15	KDAF-KCAE-W29(FERRY FLT)	Martos	5.3
21-Jan-15	W29 (DATA FLT)	Martos	1.0
22-Jan-15	W29 (DATA FLT)	Martos	3.1
22-Jan-15	W29-KCAE-KDAB(FERRY FLT)	Martos	6.2
24-Mar-15	HIGH SPEED TAXI	Martos	0.5
31-Mar-15	Air data Boom FCF	Martos	1.5
1-Apr-15	DAS FCF & INIT ADS	Martos	1.3
7-Apr-15	INIT UPWASH CAL	Martos	1.3
14-Apr-15	ADS Calibration	Martos	2.3
16-Apr-15	Stall Flights	Martos	1.2
16-Apr-15	Depot Star Calibration	Martos	0.7
20-Apr-15	Depot Star Calibration	Martos	1.5
22-Apr-15	DFR (DATA FLT) TWO MASTS	Martos	2.0
24-Apr-15	Stall Flights	Martos	1.3
1-May-15	GPS Step Decrease	Martos	1.4
8-May-15	Checkout DAS New Laptop	Martos	1.2
12-May-15	Checkout DAS New Laptop	Martos	1.2
12-May-15	Stall Flights - Defeat Guidance	Martos	0.7
21-May-15	Stall Flights - Defeat Guidance	Martos	1.1
26-May-15	KDAF-KCAE-W29(FERRY FLT)	Martos	5.5
26-May-15	W29 (DATA FLT)	Martos	2.0
27-May-15	W29 (DATA FLT)	Martos	1.6
15-Jun-15	W29-KDAB(FERRY FLT)	Martin	5.4
17-Aug-15	KDAF-W29(FERRY FLT)	Martos	5.8
18-Aug-15	W29 (DATA FLT)	Martos	1.5
18-Aug-15	W29 (DATA FLT)	Martos	2.3
18-Aug-15	W29 (DATA FLT)	Martos	1.7
19-Aug-15	W29 (DATA FLT)	Martos	1.8
19-Aug-15	W29-KDAB(FERRY FLT)	Martos	6.7
		TOTAL	74.3